

Polarized Di-Hadron Production
in Lepton-Nucleon Collisions
at the Next-To-Leading Order of QCD



Dissertation

zur Erlangung des
Doktorgrades der Naturwissenschaften
(Dr. rer. nat.)
der naturwissenschaftlichen Fakultät II - Physik
der Universität Regensburg

vorgelegt von
Christof Hendlmeier
aus Regensburg

Regensburg, im Mai 2008

Promotionsgesuch eingereicht am 14. Mai 2008
Promotionskolloquium am 26. Juni 2008

Die Arbeit wurde angeleitet von: Prof. Dr. Andreas Schäfer

Prüfungsausschuss:

Vorsitzender: Prof. Dr. Jascha Repp

1. Gutachter: Prof. Dr. Andreas Schäfer

2. Gutachter: Prof. Dr. Vladimir Braun

Weiterer Prüfer: Prof. Dr. John Schliemann

Contents

1	Introduction	3
2	Basic Concepts of Perturbative QCD	9
2.1	The Lagrangian of QCD	9
2.2	Dimensional Regularization and Renormalization	15
2.3	Factorization, PDFs, and FFs	21
3	The Analytic NLO Calculation	33
3.1	Basic Concepts	33
3.2	Leading Order Contributions	36
3.3	Virtual Contributions	43
3.3.1	Vertex Corrections and Self-Energies	44
3.3.2	Box Contributions	46
3.4	Real Contributions	47
3.4.1	Three-body Phase Space without Hat-Momenta	50
3.4.2	Three-body Phase Space including Hat-Momenta	55
3.4.3	Phase Space Integration	57
3.5	Counter Terms, the Cancellation of Singularities, and Final Results	62
4	Phenomenological Applications with the Analytic Approach	69
4.1	Results for COMPASS Kinematics	73
4.2	Results for HERMES Kinematics	81
5	The Monte Carlo Approach	87
5.1	Soft Regions	89
5.2	Collinear Regions	91
5.2.1	Final State Collinearities	91
5.2.2	Initial State Collinearities	94
6	Phenomenological Applications of the Monte-Carlo Method	99
6.1	Testing the Stability of the MC Code	100
6.2	Results for COMPASS Kinematics	102
6.3	Results for HERMES Kinematics	108

7	Summary and Conclusions	113
A	Feynman Rules	117
B	Phase Space Integrals	121
B.1	Single Propagators $I_1(X_i)$	121
B.2	Double Propagators $I_1(X_i X_j)$	124
C	Soft Matrix Elements and Integrals	129

1 Introduction

The understanding of what builds up our visible and non-visible universe was and still is one of the key questions of physics, starting with the Greek philosopher Demokrit, who supposed a model that matter is made up of indivisible (Greek: *a-tomos*) particles called atoms. This was ignored rather 2000 years, and it took until the 19th century when the physicist Joseph John Thomson discovered the existence of one constituent of atoms, namely the electron. In the beginning of the 20th century Ernest Rutherford revealed in his scattering experiments the finding that atoms are not massive particles, but have an inner structure. He suggested that the positive charge of an atom and most of its mass is concentrated in a nucleus at the center of an atom, with the electrons orbiting it like planets around the sun [1]. Rutherford's model was further revised by the physicist Niels Bohr in 1913, when he suggested that the electrons were confined into clearly defined orbits [2]. After the discovery of pions in cosmic rays in 1947 [3], the development of improved particle accelerators and particle detectors led to the identification of a large amount of hadrons. The notion of quarks evolved out of a classification of these hadrons developed independently in 1961 by Gell-Mann and Nishijima [4], which was called the *eightfold way*, as in this scheme the hadrons are grouped together into octets. This quark model was further revised by Ne'eman and Zweig [5] and attained great success for, e.g., the prediction of the Ω^- baryon [6], which was eventually discovered at the Brookhaven National Laboratory.

In the 1960's a new program was started at the Stanford Linear Accelerator Center (SLAC), where a high-energy electron scatters off a nucleon, interacting via the exchange of a photon with high virtuality Q^2 [7]. The results of this Deep-Inelastic Scattering (DIS) compelled an interpretation as elastic scattering of the electron off pointlike, spin-1/2 constituents of the nucleon, carrying fractional electric charge. These constituents, called "partons", were subsequently identified with the quarks.

One assumption of this very successful parton interpretation of DIS was that partons are practically free (i.e., non-interacting) on the short time scales set by the high virtuality of the exchanged photon. As a consequence, the underlying theory of the strong interactions must actually be relatively weak on short time or, equivalently, distant scales. The groundbreaking development was when Gross, Wilczek and Politzer showed in 1973 that the non-Abelian theory Quantum Chromodynamics (QCD) of quarks and gluons possessed the remarkable feature

of “asymptotic freedom”, a discovery for which they were awarded the 2004 Nobel Prize for Physics [8]. This weak interaction of partons at short distances were then predicted to lead to visible effects in the experimentally measured DIS structure function

$$F_1(x, Q^2) = \frac{1}{2} \sum_q e_q^2 [q(x, Q^2) + \bar{q}(x, Q^2)]. \quad (1.1)$$

Here, q [\bar{q}] are the probabilities for finding an unpolarized quark [antiquark] in the unpolarized nucleon with a fraction x of the nucleon’s momentum. Q^2 is the virtuality of the exchanged photon and determines the length scale $R \simeq 1/Q$ probed in DIS. e_q is the electric charge of quark q and the sum runs over all possible quark flavors being determined by the center-of-mass system (c.m.s.) energy \sqrt{S} of the high-energy experiment. The dependence of the structure function F_1 on the virtuality Q^2 is known as “scaling violations”. It essentially describes the response of the partonic structure of the proton to the resolving power of the virtual photon, set by its virtuality Q^2 . Within the theory of QCD, including the introduction of gluons as the particles mediating the strong force, precise predictions for the Q^2 dependence of F_1 can be provided. It turned out that the predicted scaling violations were observed experimentally and verified with great precision by the H1 and ZEUS experiments at DESY-HERA [9]. This led to a great triumph of the theory of strong interactions, namely QCD, and made DIS to a very useful tool for understanding the structure of nucleons.

Nowadays, QCD is embedded in the Standard Model of particle physics describing three of the four fundamental forces between the elementary particles: electromagnetism, weak, and strong interaction, with gauge bosons as the force-mediating particles.

A further milestone in the study of the nucleon was the advent of polarized electron beams in the early 1970’s. This now allowed to perform DIS measurements with polarized lepton beams and nucleon targets, offering the first time the possibility to study whether quarks and antiquarks have preferred spin directions inside a spin-polarized nucleon. It was first studied at SLAC [10] and the European Muon Collaboration (EMC) [11]. The program of polarized DIS has been and still is an enormous successful branch of particle physics. In analogy to unpolarized DIS, one defines a spin-dependent structure function g_1 by

$$g_1(x, Q^2) = \frac{1}{2} \sum_q e_q^2 [\Delta q(x, Q^2) + \Delta \bar{q}(x, Q^2)], \quad (1.2)$$

with Δq [$\Delta \bar{q}$] being the helicity distributions of quarks [antiquarks] in the nucleon. For example,

$$\Delta q(x, Q^2) = q^+(x, Q^2) - q^-(x, Q^2) \quad (1.3)$$

counts the number density of quarks with the same helicity minus the number density of quarks with opposite helicity as the nucleon. A more detailed definition of these quantities will be given in Chapter 2. In the same way, one can define a helicity distribution for gluons by

$$\Delta g(x, Q^2) = g^+(x, Q^2) - g^-(x, Q^2). \quad (1.4)$$

Now, a prime question is how the proton spin, which is well known to be $\frac{1}{2}$, is composed of the average spins and orbital angular momenta of quarks and gluons inside the proton. To be more precise, this is expressed by the spin “sum rule” [12]

$$S_z^p = \frac{1}{2} = \frac{1}{2}\Delta\Sigma(Q^2) + \Delta G(Q^2) + L_z^{q,\bar{q}}(Q^2) + L_z^g(Q^2), \quad (1.5)$$

stating that the proton’s spin- $\frac{1}{2}$ consists of the total quark polarization $\Delta\Sigma(Q^2) = \int_0^1 dx[\Delta u + \Delta\bar{u} + \Delta d + \Delta\bar{d} + \Delta s + \Delta\bar{s}](x, Q^2)$, the total gluon polarization

$$\Delta G(Q^2) = \int_0^1 \Delta g(x, Q^2) dx, \quad (1.6)$$

and of the orbital angular momenta $L_z^{q,\bar{q},g}$ of quarks and gluons.

The single most prominent result of polarized DIS is the finding that quark and antiquark spins summed over all flavors provide very little - only about $\sim 20\%$ - of the proton spin [13]. This result is in striking contrast with predictions from constituent quark models and has therefore been dubbed “proton spin crisis/surprise”. Even though the identification of nucleon with parton helicity is not a prediction of QCD, such models have enjoyed success in describing hadron magnetic moments and spectroscopy. This result now implies that sizable contributions to the nucleon spin should come from the polarization of gluons ΔG and/or from orbital angular momenta $L_z^{q,\bar{q},g}$ of partons.

To this day, very little is known about orbital angular momenta of partons. There are attempts to gain information about it from QCD sum rules [14] and in exclusive processes like deeply virtual Compton scattering (DVCS) [15]. A theoretical approach can also be made via Lattice QCD calculations [16].

Scaling violations in polarized DIS allow, in principle, to determine not only the $\Delta q + \Delta\bar{q}$ combinations for various flavors, but also $\Delta g(x, Q^2)$. However, due to the limited range in Q^2 , results from DIS alone are not very conclusive [17].

A better way to access $\Delta g(x, Q^2)$ in lepton-nucleon scattering is to select final states, which are predominantly produced through the photon-gluon fusion process. Due to the relatively small c.m.s. energy \sqrt{S} available in the current fixed-target experiments, such studies are limited to charm and single- or di-hadron production at moderate transverse momenta P_T . Recent results from charm production at the COMPASS experiment [18] at CERN give a rather poor

picture of the size of $\Delta g(x, Q^2)$ [19]. It turns out that the production of hadrons is the much more promising process. Single- and di-hadron production is studied at COMPASS and HERMES at DESY and first results have already been published [20, 21].

The main goal of this work is to provide a reliable theoretical framework to describe and analyze the photoproduction of two hadrons at high transverse momenta in lepton-nucleon collisions at the next-to-leading order (NLO) in perturbative QCD (pQCD). So far, calculations are available only for single-inclusive photoproduction of hadrons [22] at NLO and photoproduction of hadron pairs at leading order (LO) [23]. We will give cross sections and spin asymmetries for both COMPASS and HERMES kinematics and make detailed studies of the underlying subprocesses. This is also crucial for a future global QCD analysis of all spin-dependent data in terms of polarized parton densities, in particular $\Delta g(x, Q^2)$. Due to the lack of a theoretical framework at NLO, di-hadron photoproduction data have been left out in recent analyses for polarized distribution functions [24]. Further applications of our calculations can be made for a polarized lepton-proton collider such as the planned Electron-Ion Collider (EIC) [25].

It should be noted that results from polarized lepton-nucleon scattering experiments are now supplemented by a growing amount of data from polarized proton-proton collisions at BNL-RHIC [26]. The strength of RHIC is the possibility to study several different processes, which are directly sensitive to gluon polarization $\Delta g(x, Q^2)$: single-inclusive prompt photon [27], jet [28], hadron [29], and heavy flavor production at high transverse momenta P_T , or any combination of these final states in two-particle correlations. A recent global analysis, including RHIC data, set significant constraints on the gluon helicity distribution, providing evidence that $\Delta g(x, Q^2)$ is small in the accessible range of momentum fraction $0.05 \lesssim x \lesssim 0.2$ [24]. However, due to the limited range in x , statements about the first moment $\Delta G(Q^2)$ cannot be made yet.

The basic concept that underlies the theoretical framework in pQCD for high- P_T processes in lepton-nucleon and proton-proton scattering, and any global analysis thereof, is the factorization theorem [30]. In the presence of a hard scale like the virtuality Q^2 or transverse momenta P_T , quarks can be treated as quasi-free particles due to asymptotic freedom. The factorization theorem now states that these reactions may be factorized into long-distance pieces that contain the desired information on the spin structure of the nucleon in terms of the universal parton densities, defined in Eqs. (1.3) and (1.4), and parts that describe the short-distance, hard interactions of the partons. The latter can be evaluated order by order in the strong coupling $\alpha_s(Q^2)$ within pQCD. This decomposition of course is not exact and is valid only if a hard scale - like Q^2 or P_T - is present. Towards smaller scales there are corrections that are down by inverse powers of the scale, so-called power corrections.

Nonetheless, the results of a perturbative calculation very often give excellent approximations for physical observables, as it has been shown for example for single-inclusive hadron or jet production at RHIC [28, 29, 31]. In general, pQCD is an indispensable tool for a better understanding of scattering processes. It is extremely successful in describing hard-scattering experiments at, e.g., DESY-HERA and Fermilab's Tevatron. However, pQCD studies in LO in the strong coupling α_s are suitable only for a rough qualitative picture of the underlying process, calculations at NLO accuracy are required for a first quantitative analysis to control theoretical uncertainties. However, at the fixed-target experiments like COMPASS and HERMES, which operate at relatively low c.m.s. energies, the standard perturbative QCD framework might be not sufficient and power corrections may become relevant. They will challenge our understanding and the applicability of factorization and perturbative QCD and may open a window to the non-perturbative regime, which is very poorly explored and understood so far.

Before going into the details of predictions for the different experiments, we give a brief outline of the fundamental concepts of perturbative QCD in Chapter 2. After defining the Lagrangian of QCD, which underlies all following calculations, we show how to make predictions for processes with strongly interacting particles with perturbative methods. We give a general overview of the concept of renormalization and factorization and provide a prescription to handle divergencies showing up in pQCD calculations by dimensional regularization. Furthermore, a detailed definition of the non-perturbative objects like parton distribution functions and fragmentation functions is presented.

In Chapter 3 we give the details of an analytic calculation of two-hadron photoproduction at NLO accuracy of pQCD. An explicit computation of matrix elements and polarization sums is shown in the leading order approximation first. Next, we discuss virtual corrections and present the calculation of the three-body phase space relevant for real gluon emission corrections. Special emphasis is put on the integration of various combinations of Mandelstam variables. Thereafter, we show how factorization works in practice.

We present numerical results obtained within the analytic calculation in Chapter 4. Unpolarized and polarized cross sections for COMPASS and HERMES are presented, as well as an examination of the theoretical uncertainties arising in the calculation. Furthermore, we show the sensitivity of the experimentally relevant double-spin asymmetries to the polarized gluon distribution.

Chapter 5 is dedicated to an approach alternative to the one given in Chapter 3 using the so-called “two cut-off phase space slicing method” [32] based on Monte-Carlo integration techniques. Here, two cut-off parameters are introduced to separate the regions of phase space containing the soft and collinear singularities from the non-singular regions. We give a detailed prescription how this method

works in practice and show how to obtain finite hadronic cross sections in the end.

In Chapter 6 we present detailed phenomenological studies for COMPASS and HERMES based on the Monte-Carlo approach. We test its applicability and compare it to the results from the analytic calculation. Next, polarized and unpolarized cross sections are shown with kinematics and cuts close to the experimental setup of the fixed-target experiments.

Parts of this work containing the analytic approach have been published in Refs. [23, 33], or have been accepted for publication [34]. A publication of the main results of the second part including the Monte-Carlo approach is currently in preparation [35]. The main goal of this work is to give a detailed account of the analytic and Monte-Carlo NLO pQCD calculations. Whereas most technicalities are omitted in the publications, we provide here all relevant formulas and details of the calculation.

2 Basic Concepts of Perturbative QCD

This Chapter is dedicated to the general framework needed in all calculations in perturbative QCD (pQCD) at NLO accuracy. We introduce the Lagrangian of QCD and give an idea of how to derive Feynman rules. We will demonstrate the regularization of divergencies, which inevitably show up in higher order calculations. The procedure of renormalization is shown to remove ultra-violet divergencies, and the fundamental factorization theorem is given for a proper treatment of the remaining collinear divergencies stemming from collinear emissions of partons. We close this Chapter by defining parton distribution functions for protons and photons, and fragmentation functions. Finally, we give an overview of the experimental status of these quantities. They are needed for the phenomenological studies presented in Chapter 4 and 6.

This Chapter shall serve as an introduction to the methods used for any pQCD calculation. However, it is in no way complete and just gives an overview of the basic concepts. For a detailed account of pQCD, we refer to textbooks like [36].

2.1 The Lagrangian of QCD

The standard model of elementary particles and their interactions has two basic components: the spontaneously broken $SU(2) \times U(1)$ electroweak theory, and the unbroken $SU(3)$ color gauge theory, known as Quantum Chromodynamics (QCD). This theory of strong interactions describes the interplay of spin- $\frac{1}{2}$ quarks and spin-1 gluons. As in all quantum field theories, the starting point is the Lagrange density, which reads in the case of QCD

$$\mathcal{L}_{\text{QCD}} = \mathcal{L}_{\text{classical}} + \mathcal{L}_{\text{gauge-fixing}} + \mathcal{L}_{\text{ghost}} . \quad (2.1)$$

The first term is the classical Lagrangian given by

$$\mathcal{L}_{\text{classical}} = \sum_f \bar{\psi}_f (i\gamma_\mu D^\mu - m_f) \psi_f - \frac{1}{4} F_{\mu\nu}^a F^{a,\mu\nu} . \quad (2.2)$$

The sum in Eq. (2.2) runs over all active flavors f . ψ_f denotes a spin- $\frac{1}{2}$ quark field of flavor f with a mass m_f . Color indices are suppressed in Eq. (2.2) for simplicity.

The terms in $\mathcal{L}_{\text{classical}}$ describe the interaction of the quarks with massless spin-1 gluons. The field strength tensor $F_{\mu\nu}^a$ and the covariant derivative is given by

$$\begin{aligned} F_{\mu\nu}^a &= \partial_\mu A_\nu^a - \partial_\nu A_\mu^a + g_s f^{abc} A_\mu^b A_\nu^c \\ D_\mu &= \partial_\mu - ig_s A_\mu^a T^a, \end{aligned} \quad (2.3)$$

where A_μ^a is the gluonic field with a color index a running from 1 to $N_c^2 - 1 = 8$ in a $\text{SU}(N_c = 3)$ theory. In Eq. (2.3), g_s is the strong coupling constant, and the f^{abc} are the antisymmetric structure constants of $\text{SU}(N_c)$. The T^a are a set of eight independent Hermitian traceless 3×3 matrix generators in the fundamental or adjoint representation, which satisfy the commutator relation

$$[T^a, T^b] = if^{abc} T^c. \quad (2.4)$$

Both ψ_f and A_μ^a depend on the four-dimensional space-time vector x , which is suppressed for simplicity. Throughout this work we use the sum convention of Einstein, where a summation over repeated indices is assumed implicitly. In four dimensions the Dirac matrices γ^μ obey

$$\{\gamma^\mu, \gamma^\nu\} = 2g^{\mu\nu}, \quad (2.5)$$

where we have used the convention of Bjorken and Drell [37]

$$g^{\mu\nu} = \text{diag}(1, -1, -1, -1). \quad (2.6)$$

From now on we use the symbolic notation $\not{a} \equiv a_\mu \gamma^\mu$. The fundamental difference of QCD and Quantum Electrodynamics (QED) is the self-interaction of gluons arising from the non-vanishing commutator term in the field strength tensor of a non-Abelian theory in Eq. (2.3). This self-interaction of color-charged gluons is in contrast to the interaction of gauge bosons of QED, the photons, which are charge-neutral and hence couple only to the electrically charged fermions.

For a proper definition of the propagator for gluon fields the quantization of the classical field theory requires a gauge-fixing term for the gluon fields. The choice

$$\mathcal{L}_{\text{gauge-fixing}} = -\frac{1}{2\eta} (\partial^\mu A_\mu^a)^2 \quad (2.7)$$

fixes the class of covariant gauges with a gauge parameter η , ensuring the condition $\partial_\mu A^\mu = 0$. In principle every value for η is allowed, as the physical observables must be independent of the gauge used. Throughout this work we adopt the Feynman gauge ($\eta = 1$). In a non-Abelian theory such as QCD the covariant gauge fixing term must be supplemented by a ghost Lagrangian including anticommuting (fermionic), scalar ghost fields [38]

$$\mathcal{L}_{\text{ghost}} = g_s f^{abc} \bar{\xi}^a \partial^\mu (A_\mu^c \xi^b) - \bar{\xi}^a \partial^\mu \partial_\mu \xi^a. \quad (2.8)$$

These unphysical ghost fields (Faddeev-Popov ghosts) preserve gauge-invariance and current conservation, respectively, and cancel the unphysical polarization degrees of freedom of the gluon fields emerging in covariant gauges, as the physical degrees of freedom have to be transverse.

Altogether, the quantized QCD Lagrangian reads in a covariant gauge

$$\begin{aligned}\mathcal{L}_{\text{QCD}} = & \sum_f \bar{\psi}_f (i\gamma_\mu D^\mu - m_f) \psi_f - \frac{1}{4} F_{\mu\nu}^a F^{a,\mu\nu} \\ & - \frac{1}{2\eta} (\partial^\mu A_\mu^a) (\partial^\nu A_\nu^a) \\ & + g_s f^{abc} \bar{\xi}^a \partial^\mu (A_\mu^c \xi^b) - \bar{\xi}^a \partial^\mu \partial_\mu \xi^a, \end{aligned} \quad (2.9)$$

and is invariant under local gauge transformations.

Analytic or perturbative solutions in QCD are difficult to obtain due to the non-Abelian nature of the strong force. Depending on the relevant energy regime, there are several approaches for calculating physical observables. In the low-energy regime one of the most common methods is Lattice QCD. In a lattice gauge theory, the space-time is Wick rotated into Euclidean space, discretized, and replaced by a lattice with lattice spacing a . The quark fields are only defined at the elements of the lattice, the gluon fields at the links of the lattice. This is to reduce the analytically intractable path integrals of the continuum theory to a numerical computation. While it is a slow and resource-intensive approach, it has wide applicability, giving insight into parts of the theory inaccessible by other means, such as the baryon mass spectrum or hadronic corrections to weak matrix elements. However, despite considerable progress, lattice calculations still suffer from very limited space-time volumes and the extrapolation to the continuum limit.

Another well-known method is the $1/N_c$ -expansion, which starts from the premise that the number of colors is infinite, and thus simplifies certain calculations. One then makes a series of corrections to account for the fact that $N_c = 3$. Until now it has been the source of qualitative insight, rather than a method for quantitative predictions.

In addition to the two approaches given above, another method in the low-energy regime is chiral perturbation theory. In this regime of QCD, the degrees of freedom are no longer quarks and gluons, but rather hadrons. Since chiral perturbation theory assumes chiral symmetry, and therefore massless quarks, it cannot be used to model interactions of the heavier quarks. In addition, unknown coupling constants, also called low-energy constants, are associated with terms in the Lagrangian that must be determined by fitting to experimental data. The range of applicability is also highly debatable.

These methods, of course, are indispensable for a qualitative insight in the structure of the strong interactions. However, for precise calculations of cross sections

and a quantitative description of QCD one must therefore apply the method of perturbative QCD, which is applicable in the mid-to-high-energy regime. It is also very important for an analysis of a wealth of experimental data and is known to work well in the presence of a hard scale. Thus, we choose this approach in our work. In the following we will explain the details and ingredients necessary for a calculation in pQCD.

In pQCD we make an expansion in the strong coupling constant g_s , with the use of the fact that $g_s(\mu_r)$ decreases if the scale μ_r increases. This implicates that quarks move mostly free as non-interacting particles within the nucleons (asymptotic freedom). QCD is a renormalizable field theory, which implies that the coupling constant g_s must be defined by its value at some renormalization scale μ_r , i.e., $g_s = g_s(\mu_r) \equiv \sqrt{4\pi\alpha_s(\mu_r)}$. This dependence on the renormalization scale μ_r can be expressed by the renormalization group equation (RGE)

$$\mu_r \frac{dg_s(\mu_r)}{d\mu_r} = \beta(g_s(\mu_r)), \quad (2.10)$$

where the QCD *beta function* is a power series in g_s beginning at $\mathcal{O}(g_s^3)$

$$\beta(g_s) = -g_s \left(\frac{\alpha_s}{4\pi} \beta_1 + \left(\frac{\alpha_s}{4\pi} \right)^2 \beta_2 + \dots \right). \quad (2.11)$$

β_1 and β_2 can be obtained from a 1- and 2-loop calculation, respectively, of any physical quantity that depends on μ_r in perturbation theory.

At LO and NLO the β_1 and β_2 have the form

$$\begin{aligned} \beta_1 &= \frac{1}{3} (11N_c - 2n_f) \\ \beta_2 &= \frac{1}{3} (102N_c - 38n_f), \end{aligned} \quad (2.12)$$

with n_f the number of active flavors. The solution of Eq. (2.10) can be written in NLO, i.e., taking into account both the β_1 and β_2 term in Eq. (2.11), in the following form [39]

$$\alpha_s(\mu_r) \simeq \frac{4\pi}{\beta_1 \ln(\mu_r^2/\Lambda^2)} \left[1 - \frac{\beta_2}{\beta_1^2} \frac{\ln[\ln(\mu_r^2/\Lambda^2)]}{\ln(\mu_r^2/\Lambda^2)} \right]. \quad (2.13)$$

Λ is the fundamental parameter in QCD and has to be determined from experiment, giving values $\Lambda \simeq \mathcal{O}(200 \text{ MeV})$. The theory of pQCD is then applicable only for hard scales $Q \gg \Lambda$. It should be noted that no analytical solution of Eq. (2.10) exists beyond the LO approximation. Some more details on renormalization and how it works in practice can be found in the next Section.

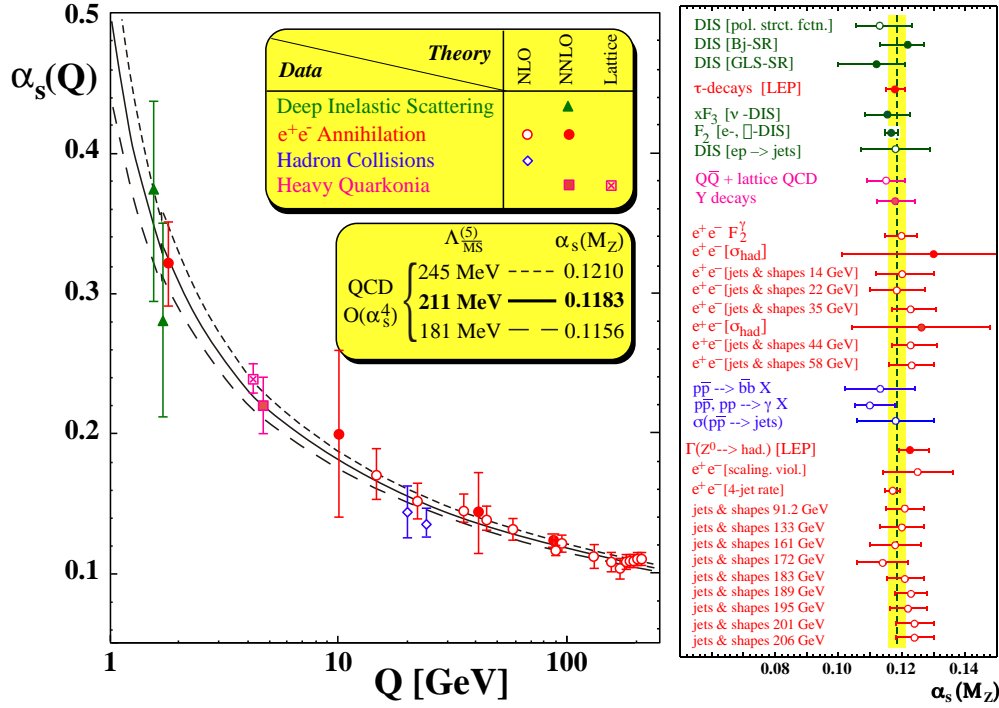


Figure 2.1: The running coupling constant $\alpha_s(Q)$. The Figure is taken from [40].

Since the strong coupling $\alpha_s(\mu_r)$ enters the calculation of all processes in leading order and beyond, it can be determined, in principle, in all processes involving hadronic particles. The energy dependence of the strong coupling $\alpha_s(\mu_r)$ provides the most powerful and decisive test of the validity of QCD. Figure 2.1 shows a compilation of many measurements of $\alpha_s(\mu_r)$ made in a variety of physical processes, at energy scales ranging from just above 1 GeV up to 200 GeV. The predicted logarithmic decrease with energy implied by Eq. (2.13) is dramatically seen. This is a fundamental property of QCD, known as *asymptotic freedom* [8]. It consists of the observation that at larger renormalization scales μ_r , or correspondingly shorter time scales, the coupling weakens, and indeed vanishes in the limit $\mu_r \rightarrow \infty$. As argued at the beginning of this Section, this is the basis for all pQCD calculations.

Thus, in the high-energy (short-distance) regime quarks and gluons can be treated as quasi-free particles, and interactions between them occur only as small perturbations. This allows us to calculate an experimentally observable quantity R in a power expansion of α_s :

$$R = \sum_{n=0}^{\infty} \alpha_s^n R^{(n)}. \quad (2.14)$$

Even if the limit $\alpha_s \rightarrow 0$ is considered, and the series in Eq. (2.14) is summed to all orders, the power expansion does not uniquely define R . One basic feature of pQCD is to assume this power expansion to be asymptotic, i.e.,

$$\left| R - \sum_{n=0}^N \alpha_s^n R^{(n)} \right| \leq B_{N+1} \alpha_s^{N+1}, \quad (2.15)$$

for all N . Provided $R^{(n)} \sim B_N$, the best approximation is achieved when the series is truncated at its minimal term and the truncation error is roughly given by the minimal term of the series. For a detailed discussion see, e.g., [41]. Asymptotic series may yield good approximations for the physical relevant quantity, even if the coefficients B_N do not converge. The divergence is due to non-perturbative effects. At collider energies it has been shown in numerous cases that perturbation theory works well in today's experiments, if the particle's energies are high enough.

The truncation of the series in Eq. (2.14) at a fixed order in the strong coupling α_s leads to a residual dependence on unphysical scales μ , such as μ_r introduced to renormalize the theory. In principle the quantity R in Eq. (2.14) is completely independent of a scale μ

$$\mu \frac{d}{d\mu} R = \mu \frac{d}{d\mu} \sum_{n=0}^{\infty} \alpha_s^n R^{(n)} = 0. \quad (2.16)$$

At a given fixed order in α_s the power series acquires a dependence on the scale. This residual dependence is due to the higher orders in α_s . It gives a gauge for the reliability of pQCD calculations, much more than the actual size of higher order corrections. Controlling the theoretical uncertainties stemming from scale dependence in a confident way motivates to go to NLO and beyond.

However, the connection between the perturbatively calculable partonic cross sections and hadrons in the initial and final states requires much more than asymptotic freedom. The problem arises already at the parton level. When one calculates partonic processes beyond LO (tree graphs), cross sections involving a definite number of particles in the final state will be divergent for certain kinematic configurations, in the limit of high energy or vanishing mass of the partons, even after renormalization. One can obtain finite results only for certain classes of cross sections, generally of the inclusive type, which are either “infrared safe”, or that can be factorized into an infrared safe (short-distance) component and a non-perturbative (long-distance) component, which are determined phenomenologically from experiment. An observable is infrared safe, when its value does not change abruptly, when an additional soft gluon is emitted, or a parton splits collinearly into a pair of partons. Such configurations are treated with the concept of factorization and renormalization, and will be discussed in detail in the next two Sections.

Before turning to the details of factorization and renormalization, we need to derive Feynman rules to obtain the amplitudes and matrix elements for every subprocess contributing to the considered process. These rules are defined from the operator

$$S_{\text{QCD}} = i \int d^4x \mathcal{L}_{\text{QCD}}, \quad (2.17)$$

with \mathcal{L}_{QCD} as given in Eq. (2.9). We can separate the Lagrangian density into a free piece \mathcal{L}_0 , which contains all the terms bi-linear in the fields, and an interaction piece \mathcal{L}_{int} containing all the rest

$$S_{\text{QCD}} = S_0 + S_{\text{int}} = i \int d^4x \mathcal{L}_0 + i \int d^4x \mathcal{L}_{\text{int}}. \quad (2.18)$$

One now obtains the Feynman rules for the inverse propagators from $-S_0$, and the interactions are derived from S_{int} . Thus, for example, the inverse fermion propagator in momentum space is obtained by making the identification

$$\partial^\mu = -ip^\mu \quad (2.19)$$

for an incoming field. In momentum space the two-point function of the quark field depends on a single momentum p . It can now be written as

$$\Gamma_{ij}^{(2)}(p) = -i\delta_{ij}(\not{p} - m), \quad (2.20)$$

which is the inverse of the propagator. Similar Feynman rules can be obtained for the gluon field and the interactions of quarks and gluons. We have listed all Feynman rules relevant for photoproduction in Appendix A. In the Appendix, the $i\epsilon$ prescription for the pole of the propagator is added to preserve causality.

2.2 Dimensional Regularization and Renormalization

After introducing the Lagrangian of QCD, Eq. (2.9), and establishing the Feynman rules, see Appendix A, we are in a position to carry out perturbative calculations of cross sections for any process involving (anti-)quarks and gluons. However, problems occur beyond the LO approximation, as one has to deal with divergencies showing up in the intermediate steps of the calculations. The procedure to make divergent integrals manifest by introducing some suitable prescription is generically called regularization. It is a purely mathematical procedure and has no physical consequences. Accordingly it is not a unique prescription, there is a variety of regularization schemes. Before going into the details of dimensional regularization [42, 43], commonly used in the most calculations in pQCD, we discuss first the different types of divergencies showing up beyond the LO.

There are three different types of divergencies:

1. Ultra-violet (UV) divergencies emerge, if one has to deal with closed loops in Feynman diagrams. As the loop momentum is not observed, it can reach in principle any value and thus has to be integrated from 0 to infinity. E.g., at high momentum p the integral over the internal propagator of a quark

$$\int_0^\infty d^4p \frac{\not{p} + m}{p^2 - m^2}$$

diverges. This is for example relevant for self-energies of gluons, quarks and antiquarks as well as box diagrams. We refer to Chapter 3 for a detailed discussion of diagrams of this type.

2. Infrared (IR) or soft divergencies show up, if the momentum of an emitted parton approaches zero.
3. Collinear divergencies are encountered, when the emission of a parton is collinear to another parton leg.

A physical cross section measured in experiment is, of course, free of any divergencies. UV divergencies are removed by the renormalization procedure. The IR and simultaneous IR and collinear divergencies cancel in the sum off all diagrams contributing to a specific process, according to a theorem by Kinoshita, Lee, and Nauenberg [44, 45, 46]. The remaining collinear divergencies are factorized from the hard partonic cross section into the bare parton distribution functions and fragmentation functions, depending on whether the collinearity is in the initial or final state. The factorization procedure will be discussed in detail in Section 2.3.

Throughout this work we use dimensional regularization [42, 43]. Here, one assumes that the space-time dimension is extended to $n = 4 - 2\varepsilon$ with an a priori arbitrary but small parameter ε . Integrals, which are divergent in four dimensions, are defined in n dimensions. The divergencies are “hidden” in quantities proportional to $1/\varepsilon$ and $1/\varepsilon^2$, whose coefficients must be canceled by renormalization and/or factorization and in the sum of all contributing diagrams to obtain physical quantities in the limit $\varepsilon \rightarrow 0$. Contrary to many other regulators, dimensional regularization is known to lead to consistent results (e.g., preserving Ward identities) to all orders in perturbation theory.

In dimensional regularization, every integral over momentum space has to be replaced by

$$\int \frac{d^4p}{(2\pi)^4} \quad \rightarrow \quad \int \frac{d^n p}{(2\pi)^n}, \quad (2.21)$$

and the contracted metric tensor is

$$g_\mu^\mu = g_{\mu\nu} g^{\mu\nu} = n. \quad (2.22)$$

To keep the action in Eq. (2.17) dimensionless, one has to replace the dimensionless coupling g_s by a dimensional one \tilde{g}_s

$$g_s \rightarrow \tilde{g}_s = \mu_d^{2-\frac{n}{2}} g_s, \quad (2.23)$$

with μ_d being an arbitrary mass scale. The Dirac algebra in n dimensions is unchanged - the Dirac matrices still satisfy the anticommutation relation of Eq. (2.5). However, problems occur in the polarized case. The projection onto specified helicities of spin-1/2 quarks and spin-1 gauge bosons (gluons and photons) requires objects like γ_5 and $\epsilon_{\mu\nu\rho\sigma}$, which are not defined in $n \neq 4$ dimensions from first principles. Throughout this work we use the so-called 't Hooft-Veltman-Breitenlohner-Maison (HVBM) scheme [43, 47]. Here, one carefully distinguishes between objects in the “usual” 4, or in the additional $(n-4)$ space-time dimensions. This is realized via a decomposition of the n -dimensional metric tensor $g_{\mu\nu}$ into a $(n-4)$ -dimensional part $\hat{g}_{\mu\nu}$ and a 4-dimensional part $\hat{\hat{g}}_{\mu\nu}$

$$g_{\mu\nu} = \hat{g}_{\mu\nu} + \hat{\hat{g}}_{\mu\nu}. \quad (2.24)$$

In the same way we get a decomposition of p_μ

$$p^\mu = (\hat{p}^\mu, \hat{\hat{p}}^\mu) = (p^0, p^1, \dots, p^{n-1}), \quad (2.25)$$

with \hat{p}^μ and $\hat{\hat{p}}^\mu$ the 4- and $(n-4)$ -dimensional part, and of the Dirac- γ matrices

$$\gamma^\mu = \hat{\gamma}^\mu + \hat{\hat{\gamma}}^\mu. \quad (2.26)$$

The tensor $\epsilon_{\mu\nu\rho\sigma}$ is defined as usual for $\mu, \nu, \rho, \sigma = 0, 1, 2, 3$ and vanishes in the extra dimensions. We note that an anticommuting γ_5 in n dimensions would lead to inconsistent results. Thus, it is defined to have a non-anticommuting part

$$\{\hat{\hat{\gamma}}^\mu, \gamma_5\} = 0, \quad [\hat{\gamma}^\mu, \gamma_5] = 0. \quad (2.27)$$

In the matrix elements the extension to n dimensions may lead to factors called “hat-momenta”, denoted by \hat{p}^μ in the additional $(n-4)$ dimensions. They appear in polarized matrix elements discussed in Sec. 3.4.2 in detail and require a special treatment when integrating over the phase space of unobserved partons. In addition, special care has to be taken for massless spin-1 bosons like gluons and photons. In n dimensions they do not have $(4-2) = 2$, but $(n-2) = 2(1-\varepsilon)$ spin degrees of freedom. This is relevant when averaging over polarizations, as, for instance, in unpolarized cross sections. In combination with poles in $1/\varepsilon$ and $1/\varepsilon^2$ the factor $1/[2(1-\varepsilon)]$ gives additional finite contributions.

In order to illustrate how dimensional regularization works in practice, we take a specific example of a UV divergent integral, namely the quark self-energy $\Sigma_{ij}(p)$,

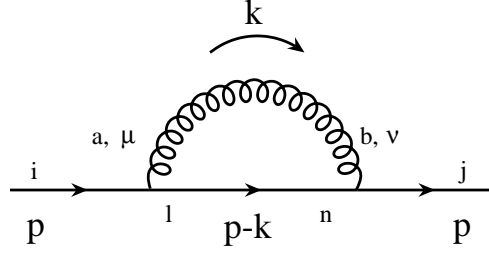


Figure 2.2: Quark self-energy. Latin indices denote the color, Greek indices the Lorentz structure.

schematically depicted in Fig. 2.2. The relation to the full quark propagator $S_{ij}(p)$, which contains all radiative corrections, reads

$$S_{ij}(p) = i \frac{\delta_{ij}}{\not{p} - m + \Sigma(p)}, \quad (2.28)$$

with $\Sigma_{ij}(p) = \delta_{ij} \Sigma(p)$.

Following the Feynman rules given in Appendix A and neglecting the masses of the quark and gluon, the quark self-energy in 4 dimensions can be written as

$$\Sigma_{ij}(p) = - \int \frac{d^4 k}{(2\pi)^4} g_s \gamma_\mu T_{il}^a \frac{\delta_{ln} (\not{p} - \not{k})}{(p-k)^2} g_s \gamma_\nu T_{nj}^b \frac{\delta_{ab}}{k^2} g^{\mu\nu}. \quad (2.29)$$

Keeping in mind that we use Einstein's sum convention, we get for the color factor

$$\delta_{ln} \delta_{ab} T_{il}^a T_{nj}^b = \sum_{a,b,l,n} \delta_{ln} \delta_{ab} T_{il}^a T_{nj}^b = C_F \delta_{ij}, \quad (2.30)$$

with $C_F = (N_c^2 - 1)/(2N_c) = 4/3$, and obtain for the self-energy

$$\Sigma(p) = -C_F g_s^2 \int \frac{d^4 k}{(2\pi)^4} \frac{\gamma_\mu (\not{p} - \not{k}) \gamma^\mu}{k^2 (p-k)^2}. \quad (2.31)$$

This 4-dimensional integral is linearly divergent, as can be easily seen by simple power counting in k

$$\int d^4 k \frac{k}{k^2 k^2} \sim \lim_{K \rightarrow \infty} K. \quad (2.32)$$

Thus, the divergence stems from the high-momentum region $|k| \rightarrow \infty$. Now, the divergence can be removed, if the dimension of the integral is changed to

$n = (4 - 2\varepsilon) < 4$. Using dimensional regularization, the regularized form of Eq. (2.31) reads

$$\Sigma(p) = C_F \tilde{g}_s^2 (2 - n) \int \frac{d^n k}{(2\pi)^n} \frac{\not{k} - \not{p}}{k^2 (p - k)^2}, \quad (2.33)$$

where we have used

$$\gamma_\mu \gamma_\nu \gamma^\mu = (2 - n) \gamma_\nu, \quad (2.34)$$

and replacing g_s according to Eq. (2.23). Using Feynman parameterization and going to the Euclidean space by a Wick rotation, one can compute the integral over k and obtains for the quark self-energy

$$\Sigma(p) = iC_F \frac{g_s^2}{(4\pi)^2} \not{p} \left(\frac{4\pi\mu_d^2}{-p^2} \right)^\varepsilon (1 + \varepsilon) \left(\frac{1}{\varepsilon} - \gamma_E \right) + \mathcal{O}(\varepsilon), \quad (2.35)$$

where γ_E is the Euler-Mascheroni constant. This unrenormalized expression for the quark self-energy is obviously divergent as $\varepsilon \rightarrow 0$, and hence this limit cannot be taken yet. Inserting Eq. (2.35) in Eq. (2.28) and again neglecting the mass m yields

$$S_{ij}(p) = i \frac{\delta_{ij}}{\not{p}} \frac{1}{1 + \tilde{\Sigma}(p^2)}, \quad (2.36)$$

where

$$\tilde{\Sigma}(p^2) = iC_F \frac{g_s^2}{(4\pi)^2} \left(1 + \frac{1}{\varepsilon} - \gamma_E + \ln \frac{4\pi\mu_d^2}{-p^2} \right) + \mathcal{O}(\varepsilon). \quad (2.37)$$

The procedure to remove UV divergencies like in Eq. (2.37) is called renormalization. In a renormalizable field theory like QCD, this is achieved by redefining the gluon, quark, and ghost fields as well as coupling constants

$$\begin{aligned} A_\mu^a &= Z_3^{1/2} A_{r,\mu}^a, \\ \psi &= Z_2^{1/2} \psi_r, \\ \xi^a &= \tilde{Z}_3^{1/2} \xi_r^a, \\ g_s &= Z_g g_{r,s}, \\ \eta &= Z_3 \eta_r, \\ m &= Z_m m_r, \end{aligned} \quad (2.38)$$

by so-called renormalization constants for gluon fields (Z_3), quark fields (Z_2), ghost fields (\tilde{Z}_3), masses (Z_m), and coupling constants (Z_g). The renormalization constant for the gauge parameter η is chosen to be the same as for the gluon field A_μ^a , so that the gauge-fixing term is kept in the same form under this redefinition. This redefinition can be done systematically order-by-order in perturbation

theory. The renormalization constants are not independent, but related among each other via Slavnov-Taylor identities [48, 49], reflecting the gauge-symmetry of \mathcal{L}_{QCD} .

In a consistent way, we now renormalize the full quark propagator by the factor Z_2

$$S_{r,ij}(p) = \frac{1}{Z_2} S_{ij}(p), \quad (2.39)$$

with $S_{r,ij}(p)$ being the renormalized (finite) quark propagator. Z_2 is now expanded in powers of the strong coupling constant g_s

$$Z_2 = 1 - z_2 + \mathcal{O}(g_s^4), \quad (2.40)$$

with z_2 being the term of order g_s^2 , which is assumed to be divergent. The renormalized full quark propagator now takes the form (up to $\mathcal{O}(g_s^2)$)

$$S_{r,ij}(p) = i \frac{\delta_{ij}}{\not{p}} \frac{1}{1 + \tilde{\Sigma}(p^2) - z_2}. \quad (2.41)$$

Now the propagator is free of any divergencies, and hence $(\tilde{\Sigma}(p^2) - z_2)$ should be finite. This requirement determines the constant z_2 up to a finite additive constant. In order to fix this arbitrariness in z_2 , we need an additional requirement, which defines a renormalization scheme. There are a variety of schemes depending on the specific problem. The most common one is the Modified Minimal Subtraction scheme ($\overline{\text{MS}}$ scheme) [50], used throughout this work. It results from the observation that poles always appear in the following combination

$$\frac{1}{\varepsilon} - \gamma_E + \ln 4\pi, \quad (2.42)$$

which is a special feature in dimensional regularization. Hence, it is convenient to not only eliminate the pole $1/\varepsilon$, as it is done in the Minimal Subtraction scheme (MS scheme) [51], but to subtract the accompanied terms as well. The renormalization constant z_2 takes the following form in the $\overline{\text{MS}}$ scheme

$$z_2 = i C_F \frac{g_s^2}{(4\pi)^2} \left(\frac{1}{\varepsilon} - \gamma_E + \ln 4\pi \right). \quad (2.43)$$

The renormalized and finite $\overline{\text{MS}}$ quark propagator reads

$$S_{r,ij} = i \frac{\delta_{ij}}{\not{p}} \left[1 + i C_F \frac{g_s^2}{(4\pi)^2} \left(1 + \ln \frac{\mu_d^2}{-p^2} \right) \right]^{-1}. \quad (2.44)$$

Equation (2.44) is only valid for the off-shell case, i.e., $p^2 \neq 0$. The renormalization prescription has to be slightly modified for on-shell quarks appearing in Feynman graphs with external quark lines. Such details are discussed, e.g., in [31].

2.3 Factorization, Parton Distribution Functions, and Fragmentation Functions

In this Section we introduce the concept of factorization and give definitions for parton distribution functions and fragmentation functions, which link us to apply perturbative calculations to processes involving hadrons instead of partons. Factorization is the property that some cross section or amplitude is a product of two or more factors and that each factor depends only on physics happening on one momentum (or distance/time) scale [30]. The process is supposed to involve some large momentum transfer, in our case the high transverse momentum P_T of an observed hadron, and corrections to the factorized form are suppressed by inverse powers of this scale. Factorization allows to derive predictions for cross sections by separating (factorizing) long-distance from short-distance behavior in a systematic fashion. We note that a rigorous proof of factorization to all orders in perturbation theory is an intricate problem and has been established only in very few cases like DIS. Nevertheless, pQCD calculations are in excellent agreement with a wealth of experimental data, making pQCD to a well established framework.

We now assume that all UV divergencies are canceled via the renormalization procedure and IR as well as simultaneous IR and collinear divergencies have been removed in the appropriate sum of all diagrams. Thus, the only divergencies appearing in this step of a NLO calculation are simple collinear poles. In the factorization procedure, these poles are now factorized from the hard partonic cross section into the bare parton distribution and fragmentation functions, which thereby become scale dependent.

We are interested in polarized photoproduction with two observed hadrons in the final state. The polarized hadronic cross section for this process, characterized by a hard momentum transfer Q , can generically be written as convolution, denoted by the symbol \otimes , of soft (long-distance) and hard (short-distance) components

$$\begin{aligned} d\Delta\sigma(Q) &= \Delta f_a(\mu_f) \otimes \Delta f_b(\mu_f) \\ &\otimes d\Delta\hat{\sigma}(Q/\mu_f, \mu_f/\mu'_f, Q/\mu'_f) \otimes D_c(\mu'_f) \otimes D_d(\mu'_f). \end{aligned} \quad (2.45)$$

$\Delta f_{a,b}(\mu_f)$ denote polarized parton distribution functions (PDF), evaluated at a factorization scale μ_f , and $D_{c,d}(\mu'_f)$ are the fragmentation functions at an in principle other factorization scale μ'_f . A detailed definition of these objects will be given at the end of this Section. $d\Delta\hat{\sigma}$ represents the hard partonic cross section, evaluated at a given order in the strong coupling constant α_s , at a momentum scale Q , and depending on the ratios of the appearing scales Q, μ_f, μ'_f . The dependence on the renormalization scale μ_r is suppressed for simplicity.

The reshuffling of the collinear poles from the hard partonic cross section to the bare parton distributions involves some degree of arbitrariness, which is known as factorization scheme dependence. One can shift finite terms together with the poles in ε . As in the renormalization procedure, we will mostly employ the $\overline{\text{MS}}$ factorization scheme, where $1/\varepsilon$ poles are subtracted together with the $(\ln 4\pi - \gamma_E)$ -terms appearing in dimensional regularization.

The computation of two-hadron production in lepton-nucleon scattering involves also processes, where the exchanged photon fluctuates into a vector meson with the same quantum numbers (“resolved photon”). A proper factorization of all collinear divergencies requires the introduction of photon PDFs. In this case, we slightly deviate from the $\overline{\text{MS}}$ scheme, and use the DIS_γ scheme [52], where the coefficient function C_γ in F_2^γ for the NLO process $\gamma^*\gamma \rightarrow q\bar{q}$ is absorbed into the definition of the photonic parton densities. Details about the transformation from one scheme to another will be given in Chapter 3.

The expression for the hadronic cross section in Eq. (2.45) is then free of any divergencies and is the starting point for the calculation of any observable in pQCD involving two hadrons in the final state.

We now turn to a detailed definition of the (un)polarized parton distribution and fragmentation functions. Parton distribution functions $f_i^H(x, \mu)$ describe the internal structure of hadrons. They are defined directly in terms of hadronic matrix elements of bi-local operators [53]. In their simplest form, these matrix elements may be given in terms of operators $b_i(xp, \vec{k}_T)$ and $b_i^\dagger(xp, \vec{k}_T)$, which annihilate and create a parton i with longitudinal momentum xp and transverse momentum \vec{k}_T in a hadron H of momentum p

$$f_i^H(x, \mu) = \int \frac{d^2\vec{k}_T}{(2\pi)^2} \langle H(p) | b_i^\dagger(xp, \vec{k}_T) b_i(xp, \vec{k}_T) | H(p) \rangle. \quad (2.46)$$

In the light-cone gauge, $A^+ = 0$, the quark distribution function can be re-expressed in terms of the quark fields for parton i by

$$f_i^H(x, \mu) = \int_{-\infty}^{\infty} \frac{dy^-}{4\pi} e^{-ixp^+y^-} \langle H(p) | \bar{\psi}_i(0^+, y^-, \vec{0}_T) \gamma^+ \psi_i(0) | H(p) \rangle, \quad (2.47)$$

with the use of light-cone coordinates. Similar definitions of distribution functions can be made for antiquarks and gluons. At the LO in pQCD, they give the probability for finding a parton i in a hadron H at a scale μ with longitudinal momentum fraction x of the hadron’s momentum. Beyond the LO, Eq. (2.47) is subject to renormalization and hence requires the choice of a particular scheme, e.g., the $\overline{\text{MS}}$ scheme.

Although perturbative QCD cannot predict the absolute normalization of these parton distributions, their evolution with the factorization scale can be calculated.

More precisely, the scale dependence is governed by a set of coupled integro-differential evolution equations, valid to all orders in $\alpha_s(\mu)$, known as DGLAP evolution equations [54]

$$\mu \frac{d}{d\mu} \begin{pmatrix} f_q^H(x, \mu) \\ f_g^H(x, \mu) \end{pmatrix} = \frac{\alpha_s}{2\pi} \int_x^1 \frac{dy}{y} \begin{pmatrix} P_{qq} & P_{qg} \\ P_{gq} & P_{gg} \end{pmatrix}_{(y, \alpha_s(\mu))} \begin{pmatrix} f_q^H(x/y, \mu) \\ f_g^H(x/y, \mu) \end{pmatrix}. \quad (2.48)$$

The kernels $P_{ij}(x, \mu)$, known as splitting functions, have the physical interpretation as probability densities for obtaining a parton of type i from one of type j with a fraction x of the parent parton's momentum. They have a perturbative expansion

$$P_{ij}(x, \mu) = P_{ij}^{(1)}(x) \frac{\alpha_s(\mu)}{\pi} + P_{ij}^{(2)}(x) \left(\frac{\alpha_s(\mu)}{\pi} \right)^2 + \dots, \quad (2.49)$$

and the $P_{ij}^{(k)}$ are known up to three loops (next-to-next-to-leading order) in the unpolarized case [55]. Equation (2.48) can also be obtained by demanding that the left side of Eq. (2.45) is independent of μ_f , i.e.,

$$\frac{d\sigma(Q)}{d\ln \mu_f} = 0. \quad (2.50)$$

The definition giving the PDFs in terms of operators, Eq. (2.47), is process independent. The same distributions then appear in the QCD formula for any process with one or two hadrons in the initial state, and thus exhibit the property of universality. Needless to say, the parton distributions and the partonic cross section in Eq. (2.45) have to be evaluated in the same renormalization/factorization scheme.

In principle, some integer moments of Eq. (2.47) can be calculated by using the method of Lattice QCD. Taking Mellin moments of Eq. (2.47) turns the bi-local into local operators, which is required for a Lattice calculation. However, a few moments are insufficient to reconstruct the x -shape of the parton distribution functions. For this reason, they have to be determined by a phenomenological global QCD analysis of experimental data.

The most comprehensive analyses are being done by the CTEQ [56, 57] and MRST [58] groups. To perform such a fit one chooses a parameterization for the distributions at some initial scale μ_0 . Certain sum rules that follow from the definition of the PDFs constrain the parameterization. An example is the momentum sum rule

$$\sum_i \int_0^1 x f_i^H(x, \mu) dx = 1, \quad (2.51)$$

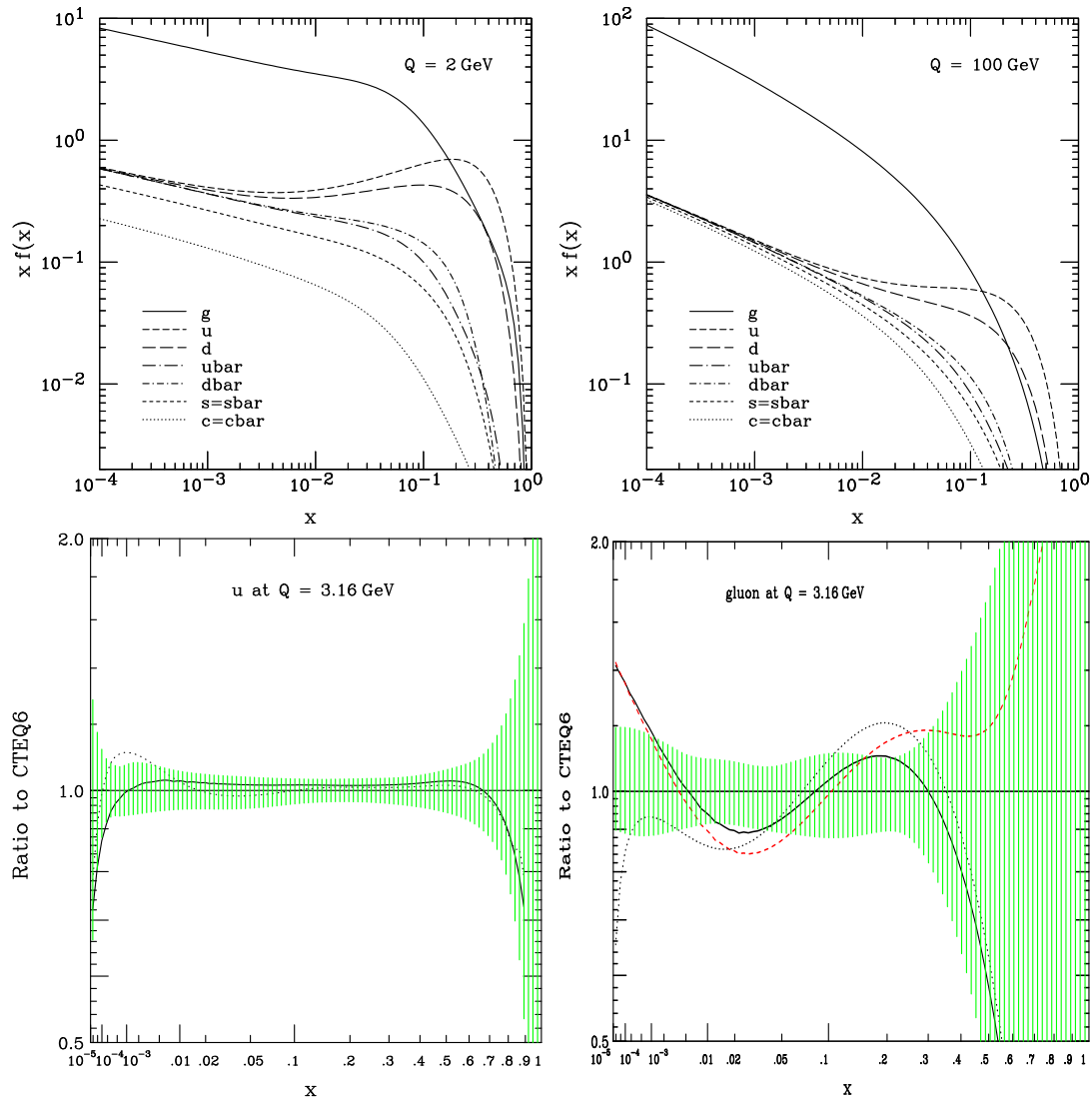


Figure 2.3: The two upper plots show parton densities $x f_i^p(x, Q)$ for the proton in the CTEQ6 NLO parameterization at a scale $Q = 2 \text{ GeV}$ (left) and $Q = 100 \text{ GeV}$ (right). The lower plots show the uncertainty bands for the up-quark and the gluon, represented by the shaded area. In addition, ratios to other results for PDFs are shown. The solid and dashed lines stand for the comparison to CTEQ5 [59], the dotted line for MRST2001 [58]. The lower plots are evaluated at a scale $Q = 3.16 \text{ GeV}$. Figures are taken from [56].

stating that the total momentum of a hadron H must be carried by all different types of partons i , indicated by the sum in Eq. (2.51).

Using the obtained parton densities for the calculation of a measurable quantity and comparing it with the experimental results, one gets an estimate for the quality of the used parameterization in terms of χ^2 . One then finds an optimized functional shape for the parton densities by minimizing χ^2 . Given some set of values for the parameters describing the $f_i^H(x, \mu_0)$, one can determine $f_i^H(x, \mu)$ for $\mu > \mu_0$ relevant for experimental data, by using the DGLAP equations in Eq. (2.48). These distributions can then be used to predict other physical observables at scales far beyond those presently achievable. Beyond this, however, the very possibility of a global fit tests the internal consistency of our fundamental theoretical picture of hard scattering, based on factorization and the universality of parton distributions.

Figure 2.3 shows the unpolarized CTEQ6 NLO parton distribution functions at scales $\mu = Q = 2$ GeV, and $Q = 100$ GeV for a proton in the $\overline{\text{MS}}$ scheme used throughout this work. The lower plots show uncertainty bands for the up-quark and gluon distributions at a scale $Q = 3.16$ GeV. One can see that both the up and down distribution is peaked at a value of $x \approx 0.3$, as expected in the naive parton model, where the three valence quarks share almost all the momentum of the nucleon. At lower values of x , the gluon dominates the parton content of a proton. The lower plots show that the up-quark is determined very well up to $x \simeq 0.6$, in contrast to the gluon distribution, where the errors are in general larger, in particular, for $x > 0.3$. This complicates also a future extraction of Δg in this region of x from measurements of spin asymmetries, which are sensitive to $\Delta g/g$. Clearly, our knowledge of the unpolarized gluon distribution has to be improved as well. A more precise extraction of unpolarized PDFs is one of the subjects at the Tevatron at Fermilab and the upcoming Large Hadron Collider (LHC) at CERN [60, 61].

Polarized, helicity-dependent parton distributions are defined via

$$\Delta f_i^H(x, \mu) \equiv f_{i+}^{H+}(x, \mu) - f_{i-}^{H+}(x, \mu), \quad (2.52)$$

whereas in the unpolarized case it takes the form

$$f_i^H(x, \mu) \equiv f_{i+}^{H+}(x, \mu) + f_{i-}^{H+}(x, \mu). \quad (2.53)$$

$f_{i+}^{H+}(x, \mu)$ [$f_{i-}^{H+}(x, \mu)$] denote the distribution of partons with its spin [anti-]aligned to the direction of the hadron's spin. Because of parity conservation we have two constraints:

$$f_{i+}^{H+}(x, \mu) = f_{i-}^{H-}(x, \mu), \quad \text{and} \quad f_{i-}^{H+}(x, \mu) = f_{i+}^{H-}(x, \mu). \quad (2.54)$$

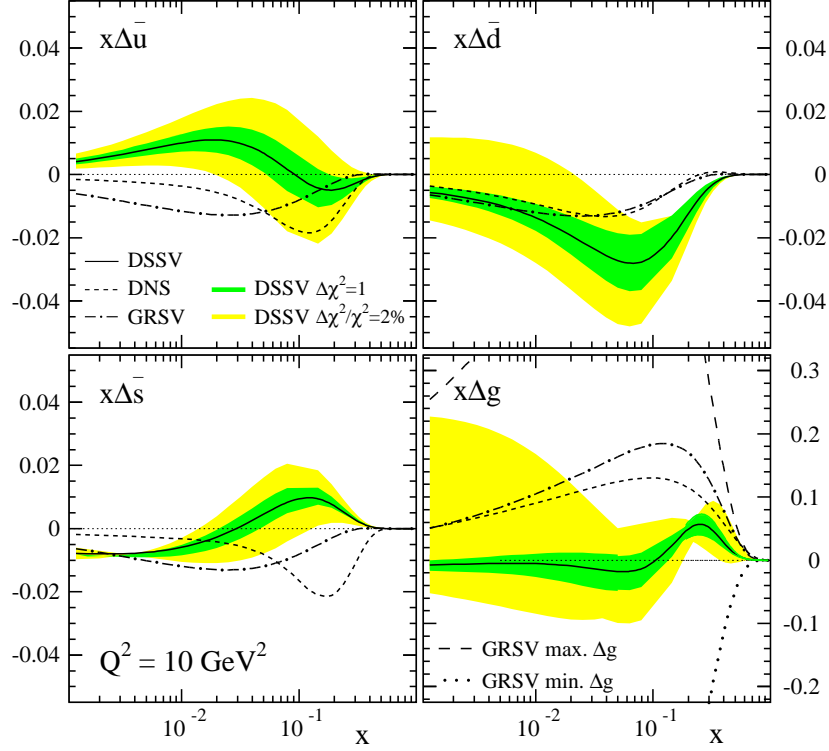


Figure 2.4: The polarized parton densities by DSSV for the sea and gluon distributions as a function of the Bjorken- x , compared to previous fits [17, 62]. The PDFs are evaluated at a scale $\mu^2 = Q^2 = 10 \text{ GeV}^2$. The uncertainty bands correspond to $\Delta\chi^2 = 1$ and $\Delta\chi^2/\chi^2 = 2\%$, respectively. The Figure is taken from [24].

The helicity-dependent parton distributions are sensitive to the longitudinal polarization of the parton inside the hadron at given momentum fraction x and scale μ . The first moments of these polarized PDFs enter the spin sum rule in Eq. (1.5) and are therefore closely related to the total spin of the respective hadron. To minimize extrapolation uncertainties in the first moment, it is crucial to know the x -shape of the polarized PDFs as accurate as possible. Generally, the first moment of Δg , the polarized gluon distribution, is not a local operator and hence not amenable to Lattice QCD.

There are DGLAP-like evolution equations also for polarized PDFs by simply replacing the unpolarized quantities by their polarized counterparts in Eq. (2.48). The polarized splitting functions are known up to two loops, i.e. NLO [63, 64]. The procedure for determining helicity-dependent distributions is similar to that

one in the unpolarized case. However, due to the lack of experimental data containing information on the structure of the longitudinally polarized proton, the polarized PDFs are not determined with high accuracy. The positivity constraint,

$$|\Delta f(x, \mu)| \leq f(x, \mu), \quad (2.55)$$

provides some guidance in LO. This constraint no longer strictly holds true in NLO, as parton densities become scheme dependent unphysical objects.

Several groups provide sets of polarized PDFs, mainly extracted from polarized Deep-Inelastic Scattering, where the light sea is assumed to be flavor-symmetric [17, 65, 66]. However, other groups provided sets of helicity-dependent distributions including Semi-Inclusive DIS (SIDIS) data [62], and also data from RHIC proton-proton measurements [24] in their fits. Here, a discrimination of the light sea distributions can be achieved. Figure 2.4 shows the best fits of the DSSV group of polarized parton densities for the sea and gluon distributions as a function of the Bjorken- x at a scale $\mu^2 = Q^2 = 10 \text{ GeV}^2$. The uncertainty bands correspond to $\Delta\chi^2 = 1$ (darker band), and $\Delta\chi^2/\chi^2 = 2\%$ (light shaded band), respectively. Their fits are compared to previous fits by GRSV [17] and DNS [62]. The dotted lines indicate the positivity constraint of Eq. (2.55), giving a maximal and minimal boundary for Δg . Whereas valence quark distributions are determined very well, the sea quark distributions exhibit larger error bands. At the same degree, the situation is completely unsatisfactory for the helicity-dependent gluon distribution $\Delta g(x, \mu)$. There is some evidence that it is small in the region $0.05 \lesssim x \lesssim 0.2$, but the first moment still suffers from large extrapolation uncertainties, and thus no reliable value for it can be quoted.

In this Thesis we will provide the theoretical framework necessary for an extraction of $\Delta g(x, \mu)$ in the photoproduction of hadron pairs at fixed-target experiments like COMPASS and HERMES. These results can then be included in a future NLO global analysis.

As mentioned before, such a calculation involves leptons in the initial state. Thus, we also have to discuss the partonic structure of the photon radiated off the lepton. This is relevant for the resolved contributions to the cross section. It has been shown that such resolved processes contribute significantly to photoproduction cross sections at HERA energies [67], and hence should not be disregarded. In any case, they are required for consistently factorizing all collinear singularities in a photoproduction cross section.

In practice, this is conveniently done by introducing a [polarized] parton distribution function in a lepton $[\Delta]f^l$, which is a convolution of a [polarized] lepton-to-photon splitting function $[\Delta]P_{\gamma l}$, and a [polarized] photon structure function $[\Delta]f_\gamma$

$$[\Delta]f^l(x, \mu) = \int_x^1 \frac{dy}{y} [\Delta]P_{\gamma l}(y) [\Delta]f_\gamma(x_\gamma = \frac{x}{y}, \mu). \quad (2.56)$$

Calculating $[\Delta]P_{\gamma l}$, the Weizsäcker-Williams equivalent photon spectrum, is a Quantum Electrodynamics (QED) issue. In the polarized case it reads [68]

$$\Delta P_{\gamma l}(y) = \frac{\alpha_{em}}{2\pi} \left[\frac{1 - (1-y)^2}{y} \ln \frac{Q_{max}^2(1-y)}{m_l^2 y^2} + 2m_l^2 y^2 \left(\frac{1}{Q_{max}^2} - \frac{1-y}{m_l^2 y^2} \right) \right], \quad (2.57)$$

where $\alpha_{em} = g_e^2/(4\pi)$ is the electromagnetic coupling constant. $\Delta P_{\gamma l}(y)$ describes the radiation of a photon with momentum fraction y off the lepton of mass m_l with a virtuality less than Q_{max}^2 . The terms in Eq. (2.57) containing logarithms are of special relevance for muon beam experiments, i.e., COMPASS.

The photon differs from a hadron in hard scattering processes. On the one hand, it can interact directly as a pointlike particle, where

$$[\Delta]f_\gamma(x, \mu) = \delta(1-x), \quad (2.58)$$

on the other hand, it can fluctuate into a hadron-like structure of quarks, anti-quarks and gluons. In the resolved case, the unpolarized densities f_γ have been mainly determined from $\gamma^*\gamma$ DIS in e^+e^- annihilations [69]. The polarized parton distributions are completely unknown at the moment. Their evolution equations (similarly for spin-averaged distributions) have an additional inhomogeneity [52, 70, 71]

$$\begin{aligned} \mu \frac{d\Delta q_\gamma(x, \mu)}{d\mu} &= \frac{\alpha_s}{2\pi} (\Delta k_q(x, \mu) + \{\Delta P_{qq} \otimes \Delta q_\gamma + \Delta P_{qg} \otimes \Delta g_\gamma\}) \\ \mu \frac{d\Delta g_\gamma(x, \mu)}{d\mu} &= \frac{\alpha_s}{2\pi} (\Delta k_g(x, \mu) + \Delta P_{gq} \otimes \{\Delta q_\gamma + \Delta \bar{q}_\gamma\} \\ &\quad + \Delta P_{gg} \otimes \Delta g_\gamma). \end{aligned} \quad (2.59)$$

Here, $\Delta P_{ij} \otimes \Delta f_\gamma$ is a shortcut for the convolution of a splitting function with a parton density

$$\Delta P_{ij} \otimes \Delta f_\gamma \equiv \int_x^1 \frac{dy}{y} \Delta P_{ij} \left(\frac{x}{y}, \mu \right) \Delta f_\gamma(y, \mu). \quad (2.60)$$

Altogether the $[\Delta]f_\gamma$ are of order $\mathcal{O}(\alpha_{em}/\alpha_s)$, such that direct and resolved contributions to photoproduction enter at the same footing. The solution of Eq. (2.59) consists of an additional inhomogeneity, which ends up in a so-called pointlike solution Δf_γ^p together with the homogeneous hadronic solution Δf_γ^h ,

$$\Delta f_\gamma(x, \mu) = \Delta f_\gamma^p(x, \mu) + \Delta f_\gamma^h(x, \mu). \quad (2.61)$$

As mentioned before, the spin-dependent photon parton distributions are com-

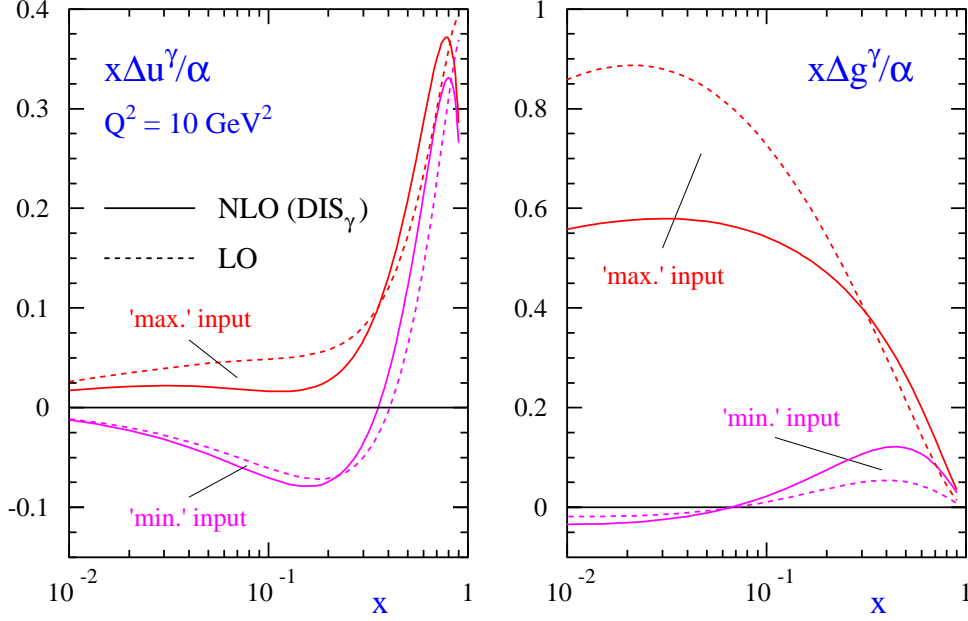


Figure 2.5: The polarized parton distribution functions in the photon. The left plot shows the up-quark distribution, the right one the gluon distribution. Both scenarios, (2.62) and (2.63), are shown at $\mu^2 = Q^2 = 10 \text{ GeV}^2$ in LO and NLO. The Figures are taken from [71].

pletely unknown to this day. To solve this dilemma one uses two extreme scenarios. In the minimal scenario the hadronic contribution is set to zero at a scale $\mu = \mu_0$,

$$\Delta f_\gamma^h(x, \mu_0) = 0, \quad (2.62)$$

whereas in the maximal scenario it is chosen to saturate the positivity constraint for Δf_γ similar to (2.55)

$$\Delta f_\gamma^h(x, \mu_0) = f_\gamma^h(x, \mu_0). \quad (2.63)$$

In both scenarios the pointlike solution vanishes at the input scale μ_0 .

Figure 2.5 shows the used spin-dependent parton distributions in the photon at a scale $\mu^2 = Q^2 = 10 \text{ GeV}^2$ in the DIS_γ scheme. The left plot shows the up quark distribution, the right one the gluon distribution. Noticeable is the fact that the difference between both scenarios diminishes at $x \rightarrow 1$. This observation is of relevance for our phenomenological studies in Chapter 6. We will demonstrate that at c.m.s. energies relevant for di-hadron photoproduction at COMPASS and HERMES, one mainly probes Δf_γ at rather large values. This greatly reduces the

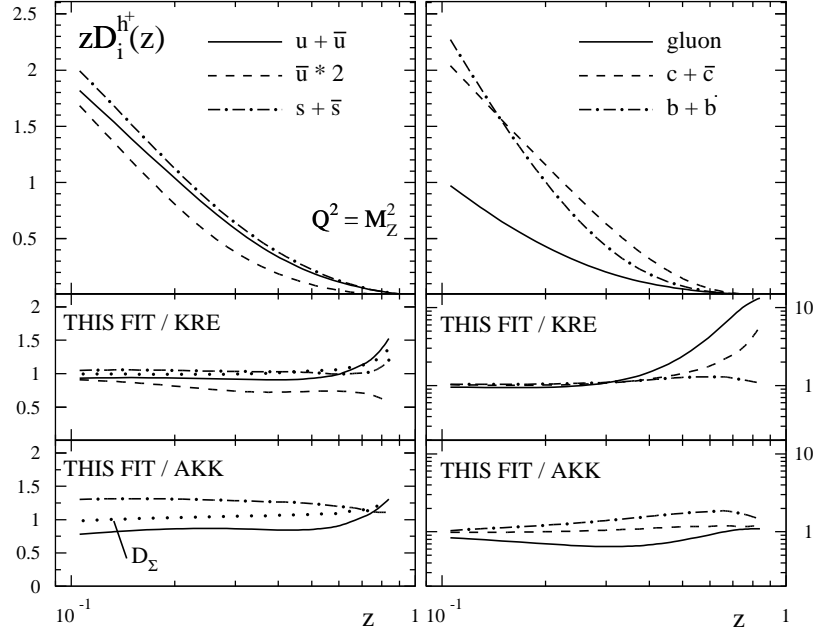


Figure 2.6: Upper panels: individual fragmentation functions for positively charged hadrons $zD_i^{h^+}(z, Q^2)$ at $Q^2 = M_Z^2 = 91.19 \text{ GeV}^2$ for $i = u + \bar{u}$, $2\bar{u}$, $s + \bar{s}$, g , $c + \bar{c}$, and $b + \bar{b}$. Middle panels: ratios of the fragmentation functions to the ones of Kretzer [72]. The dotted line indicates the ratio for singlet combination of fragmentation functions $zD_\Sigma^{h^+}$. Lower panels: ratios of the fragmentation functions to the ones of AKK; note that $D_{\bar{u}}^{h^+}$ is not available in the AKK analysis. The Figure is taken from [73].

error stemming from the lack of knowledge of the Δf_γ . As for H1 and ZEUS at DESY, the planned EIC project will operate at higher energies and hence will be sensitive to the non-perturbative structure of Δf_γ and the hadronic input $\Delta f_\gamma^h(x, \mu_0)$.

The last non-perturbative object in the factorized cross section formula, Eq. (2.45), to be defined, are fragmentation functions, denoted by $D_i^H(z, \mu)$. They describe the collinear fragmentation of a parton i into the observed hadron H at a scale μ . z is the momentum share that the hadron H inherits from its parent hadron i in the hadronization process. Again, using light-cone coordinates, the operator definition is given by [53, 74]

$$D_i^H(z, \mu) = \sum_X \int \frac{dy^-}{12\pi} e^{ik^+ y^-} \text{Tr} \gamma^+ \langle 0 | \psi_i(0, y^-, y_\perp) | H X \rangle \langle H X | \bar{\psi}_i(0) | 0 \rangle, \quad (2.64)$$

where the sum is over all final states X containing the chosen hadron H . So far, there are no results on moments of $D_i^H(z, \mu)$ in Eq. (2.64) from Lattice QCD.

Similar to parton densities, the scale evolution of fragmentation functions is governed by DGLAP-type evolution equations [54]. To extract fragmentation functions from data, similar methods are used as for parton densities explained above. However, one has to keep in mind that the bulk of experimental information about fragmentation functions comes from data of the Z resonance. It is not guaranteed that they also provide a good description at much lower energies, $1 \div 3$ GeV, relevant at fixed-target experiments.

So far, COMPASS and HERMES observe charged hadrons, with no further identification of the hadron type. From the theoretical side, the specification of certain hadrons, e.g., pions, would have more predictive power, as their fragmentation functions are determined at a much more confident level. Several groups like Kretzer [72], KKP [75], and AKK [76, 77] provide sets of fragmentation functions for charged hadrons. Throughout this work we use the sets by DSS [73], including single-inclusive hadron production in electron-positron annihilation, proton-proton collisions and deep-inelastic lepton-proton scattering, as this sets uniquely are obtained within a global analysis.

Figure 2.6 shows the fragmentation functions of DSS for positively charged hadrons and a comparison to sets of Kretzer and AKK. One feature of these distributions shown in Fig. 2.6 is the only slightly broken flavor democracy for $q + \bar{q}$ fragmentation functions into charged hadrons.

3 The Analytic NLO Calculation

In this Chapter we give the theoretical framework for a calculation of both unpolarized and polarized cross sections at the next-to-leading order (NLO) of perturbative QCD. Here, we concentrate on an *analytic approach*, i.e., the integration over unobserved particles is done analytically at the partonic level. Monte-Carlo methods are applied only for the convolution of the hard partonic cross section with the non-perturbative parton distribution and fragmentation functions. We will turn to a different approach, based on Monte-Carlo techniques already at the partonic level, in Chapter 5.

In this Thesis, we are interested in the polarized photoproduction of two hadrons at high transverse momenta. We first show the basic ideas and concepts used in all pQCD calculations. Section 3.2 is dedicated to tree level contributions (LO). We show how to calculate Feynman diagrams together with their color structure and give the relevant phase space for two partons in the final state. We treat the LO contributions already in n dimensions, as this is needed for the subsequent NLO calculation, discussed in the next three Sections.

Starting with virtual corrections, we show what types of contributions appear and how to compute such diagrams technically. Next, real corrections with three particles in the final state are considered. A detailed derivation of the two-particle inclusive phase space for the unpolarized and polarized case is given, and methods to integrate analytically all different types and combinations of Mandelstam variables, stemming from the matrix elements, are presented. The interested reader is referred to Appendix B for a detailed discussion of the explicit integrals. We close this Chapter by showing how to remove the remaining collinear poles with the concept of factorization and give all relevant formulas for this procedure.

3.1 Basic Concepts

The basic concept that underlies all perturbative QCD calculations and hence also our calculations for di-hadron photoproduction is the factorization theorem [30], which was introduced in Sec. 2.3. It states that large-momentum transfer reactions may be factorized into long- (non-perturbative) and short-distance (perturbative) contributions. The long-distance pieces contain information on

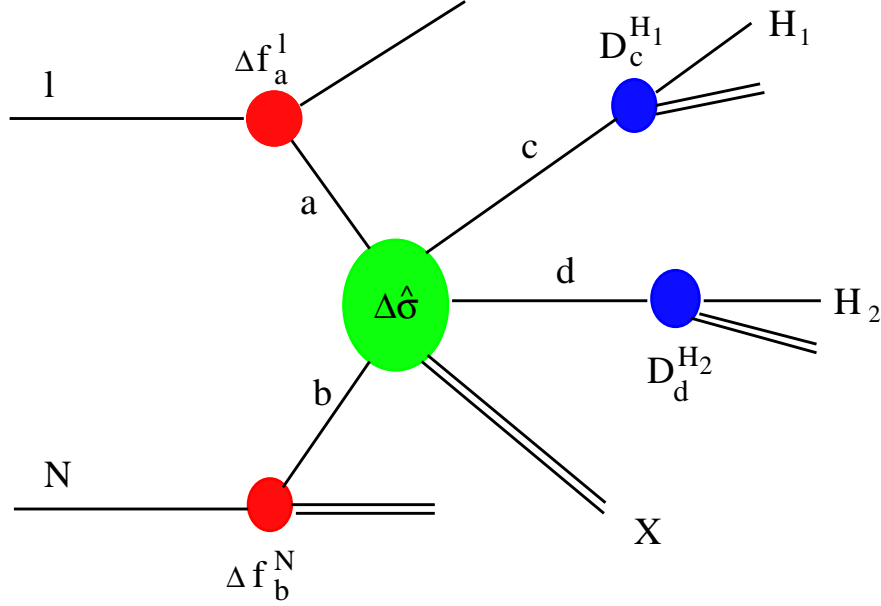


Figure 3.1: Factorization of $lN \rightarrow H_1 H_2 X$ in terms of parton distribution functions (red blobs), partonic hard-scattering cross sections (green blob), and fragmentation functions (blue blobs).

the structure of nucleons or leptons (photons) in terms of its distributions of constituents, namely partons. The short-distance parts describe the hard interactions of these partons and can be calculated from first principles in pQCD. While the parton distributions describe universal properties of the nucleon, that is, are the same in each reaction, the short-distance parts carry the process-dependence and have to be calculated for each reaction on their own.

The process considered in this work is the inclusive photoproduction of two high- P_T hadrons H_1 and H_2 in collisions of longitudinally polarized leptons and nucleons

$$l(P_l, \lambda_l) N(P_N, \lambda_N) \rightarrow l'(P_{l'}) H_1(P_1) H_2(P_2) X. \quad (3.1)$$

The exchanged photon is assumed to have low virtuality Q^2 . In the analytic approach we concentrate on the direct part to the photoproduction cross section. Here, the photon interacts as an elementary particle with one of the partons of the nucleon N . The P_i in Eq. (3.1) are the four-momenta of the external lepton and hadrons with helicity λ_i , and X contains all the additional hadronic activity not observed in experiment.

More explicitly as in Eq. (2.45), the factorization theorem states then for the

[polarized] experimentally measurable hadronic cross section:

$$\begin{aligned}
\frac{d[\Delta]\sigma}{d\mathcal{P}} &= \sum_{a,b,c,d} \int dx_l \int dx_N \int dz_1 \int dz_2 [\Delta]f_a^l(x_l, \mu_f) [\Delta]f_b^N(x_N, \mu_f) \\
&\times D_c^{H_1}(z_1, \mu_f') D_d^{H_2}(z_2, \mu_f') \\
&\times \frac{d[\Delta]\hat{\sigma}_{ab \rightarrow cdX}}{d\mathcal{P}}(x_l P_l, x_N P_N, P_1/z_1, P_2/z_2, \mu_r, \mu_f, \mu_f'), \quad (3.2)
\end{aligned}$$

where the sum is over all contributing partonic channels $ab \rightarrow cdX$ with $d[\Delta]\hat{\sigma}_{ab \rightarrow cdX}$ the associated [polarized] partonic cross section. \mathcal{P} stands for any appropriate set of the kinematic variables of the reaction, and the $[\Delta]f_{a,b}^{l,N}(x, \mu_f)$ and $D_{c,d}^{H_1,H_2}(z, \mu_f')$ are the [polarized] parton distribution functions and unpolarized fragmentation functions as introduced in Sec. 2.3. Equation (3.2) includes both direct and resolved contributions to the [polarized] photoproduction cross section via an appropriate choice for $[\Delta]f_a^l$, as it was discussed in Sec. 2.3. The idea of factorization for two-hadron production is illustrated schematically in Fig. 3.1.

The unpolarized and polarized hadronic cross sections are defined via

$$\begin{aligned}
\frac{d\sigma}{d\mathcal{P}} &\equiv \frac{1}{4} \left[\frac{d\sigma^{++} + d\sigma^{+-} + d\sigma^{-+} + d\sigma^{--}}{d\mathcal{P}} \right] \\
\frac{d\Delta\sigma}{d\mathcal{P}} &\equiv \frac{1}{4} \left[\frac{d\sigma^{++} - d\sigma^{+-} - d\sigma^{-+} + d\sigma^{--}}{d\mathcal{P}} \right], \quad (3.3)
\end{aligned}$$

and, equivalently, their partonic counterparts

$$\begin{aligned}
\frac{d\hat{\sigma}_{ab \rightarrow cdX}}{d\mathcal{P}} &\equiv \frac{1}{4} \left[\frac{d\hat{\sigma}_{ab \rightarrow cdX}^{++} + d\hat{\sigma}_{ab \rightarrow cdX}^{+-} + d\hat{\sigma}_{ab \rightarrow cdX}^{-+} + d\hat{\sigma}_{ab \rightarrow cdX}^{--}}{d\mathcal{P}} \right] \\
\frac{d\Delta\hat{\sigma}_{ab \rightarrow cdX}}{d\mathcal{P}} &\equiv \frac{1}{4} \left[\frac{d\hat{\sigma}_{ab \rightarrow cdX}^{++} - d\hat{\sigma}_{ab \rightarrow cdX}^{+-} - d\hat{\sigma}_{ab \rightarrow cdX}^{-+} + d\hat{\sigma}_{ab \rightarrow cdX}^{--}}{d\mathcal{P}} \right], \quad (3.4)
\end{aligned}$$

where the superscripts denote the helicities of the incoming particles. From parity conservation of QCD follows

$$\begin{aligned}
d\sigma_{++} &= d\sigma_{--} \\
d\sigma_{+-} &= d\sigma_{-+}, \quad (3.5)
\end{aligned}$$

and similarly on the partonic level. The main quantity of interest for experiments is the double-spin asymmetry $A_{LL}^{H_1 H_2}$, defined via

$$A_{LL}^{H_1 H_2} \equiv \frac{d\Delta\sigma}{d\sigma} = \frac{d\sigma^{++} - d\sigma^{+-}}{d\sigma^{++} + d\sigma^{+-}}. \quad (3.6)$$

We now focus on the analytic calculation of [polarized] cross sections $d[\Delta]\hat{\sigma}/d\mathcal{P}$ at the partonic level. Here, $d\mathcal{P}$ shall be an appropriate set of kinematic variables in the sense that we have maximal information on the two final state partons, which hadronize to the hadrons H_1 and H_2 .

3.2 Leading Order Contributions

With the methods of dimensional regularization, renormalization and factorization introduced in the last Chapter we are now in a position to compute partonic hard-scattering cross sections in LO and NLO accuracy. Although the main focus of this work should be on NLO corrections to the photoproduction of a hadron pair, we start with presenting LO contributions, as some concepts and important techniques in the calculation show up already at this order in the strong coupling. We extend the space-time from 4 to n already at LO, since the n -dimensional expressions of the LO results are needed in our NLO calculation for, e.g., factorization or the soft limit. At LO, the scattering of two partons with helicities λ_a and λ_b is described by the reaction

$$a(p_a, \lambda_a) + b(p_b, \lambda_b) \rightarrow c(p_c) + d(p_d), \quad (3.7)$$

with $a - d$ denoting partons, i.e., quarks, antiquarks, and gluons, respectively, and p_i their four-momenta. We consider only up-, down-, and strange-quarks, and neglect their masses, i.e.,

$$p_i^2 = m_i^2 = 0, \quad \text{for } i = a, b, c, d, \quad (3.8)$$

which is appropriate for our studies. In the calculation of partonic cross sections we emphasize that there are advantages using Mandelstam variables instead of four-momenta. In the first order of the strong coupling constant α_s we use three variables defined via

$$s = (p_a + p_b)^2, \quad t = (p_a - p_c)^2, \quad u = (p_b - p_c)^2. \quad (3.9)$$

Due to momentum conservation $p_a + p_b = p_c + p_d$ only two of the three variables are independent. With the condition of massless particles we get the constraint

$$s + t + u = m_a^2 + m_b^2 + m_c^2 + m_d^2 = 0. \quad (3.10)$$

Up to phase space factors, the [polarized] partonic cross section $d[\Delta]\hat{\sigma}_{ab \rightarrow cd}$ is proportional to the [polarized] matrix element squared $[\Delta]|\mathcal{M}|_{ab \rightarrow cd}^2$, which contains the actual information of the hard-scattering process and can be calculated

to a fixed order in the strong coupling constant α_s . Hence, $d[\Delta]\hat{\sigma}_{ab \rightarrow cd}^{(0)}$ as the LO contribution is given by

$$d[\Delta]\hat{\sigma}_{ab \rightarrow cd}^{(0)} = \frac{1}{2s} \frac{d^n p_c}{(2\pi)^{n-1}} \frac{d^n p_d}{(2\pi)^{n-1}} (2\pi)^n \overline{\sum} [\Delta] |\mathcal{M}|_{ab \rightarrow cd}^2 \times \delta(p_c^2) \delta(p_d^2) \delta^{(n)}(p_a + p_b - p_c - p_d). \quad (3.11)$$

Here, the factor $1/(2s)$ represents the flux factor for two incoming partons, the $d^n p_i/(2\pi)^{n-1}$ are the phase space factors for each outgoing parton, and the delta functions ensure the conditions for massless, on-shell partons and momentum conservation. The sum $\overline{\sum}$ in Eq. (3.11) denotes the summation over unobserved color and spin degrees of freedom for outgoing and appropriate averaging for incoming partons. As QCD is an SU(3) theory, quarks and gluons in the initial state are accompanied by factors $1/C_A = 1/3$ and $1/(C_A^2 - 1) = 1/8$, respectively, for averaging over color. For unpolarized particles the cross sections for incoming quarks require a factor $1/2$, and for incoming massless spin-1 bosons like photons and gluons we need a factor $1/[2(1 - \varepsilon)]$ in dimensional regularization.

We limit ourselves to the scattering of partons with definite helicities, without observing any polarization in the final state. This makes it convenient to utilize the following definition for unpolarized and polarized matrix elements in analogy to Eqs. (3.3) and (3.4)

$$\begin{aligned} |\mathcal{M}|^2 &= \frac{1}{2} [|\mathcal{M}|^2(+, +) + |\mathcal{M}|^2(+, -)] \\ \Delta|\mathcal{M}|^2 &= \frac{1}{2} [|\mathcal{M}|^2(+, +) - |\mathcal{M}|^2(+, -)], \end{aligned} \quad (3.12)$$

where we again employed parity conservation, i.e., $|\mathcal{M}|^2(+, +) = |\mathcal{M}|^2(-, -)$ and $|\mathcal{M}|^2(+, -) = |\mathcal{M}|^2(-, +)$. The arguments \pm in Eqs. (3.12) denote the helicities of the incoming particles, which can acquire the values ± 1 . We shall emphasize here that the two parts do not mix, i.e.,

$$|\mathcal{M}|^2(\lambda_a, \lambda_b) = |\mathcal{M}|^2 + \lambda_a \lambda_b \Delta|\mathcal{M}|^2, \quad (3.13)$$

with λ_a and λ_b being the helicities of parton a and b . We can interpret the first part in Eq. (3.13) as the spin-averaged and the second part as the spin-dependent contribution to the matrix element.

In the case, where the photon directly interacts with a parton stemming from the nucleon, we only have two relevant processes at the first order in the strong coupling constant α_s , namely the QCD Compton process

$$\gamma q \rightarrow qg, \quad (3.14)$$

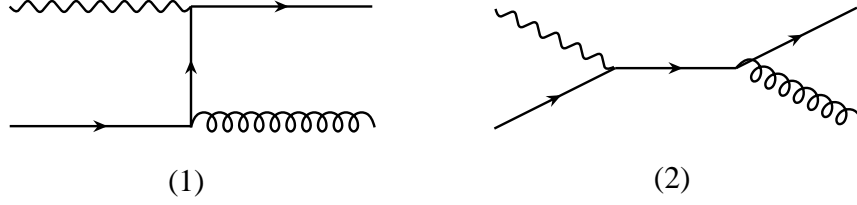


Figure 3.2: The two Feynman diagrams contributing to $\gamma q \rightarrow qg$.

and photon-gluon fusion (PGF)

$$\gamma g \rightarrow q\bar{q}, \quad (3.15)$$

whereas if the photon resolves into its hadronic constituents, as discussed in detail in Sec. 2.3, we have eight additional processes in LO accuracy of pQCD

$$\begin{aligned}
 qq' &\rightarrow qq' \\
 q\bar{q} &\rightarrow q'\bar{q}' \\
 qq &\rightarrow qq \\
 q\bar{q} &\rightarrow q\bar{q} \\
 q\bar{q} &\rightarrow gg \\
 gg &\rightarrow q\bar{q} \\
 qg &\rightarrow qg \\
 gg &\rightarrow gg.
 \end{aligned} \quad (3.16)$$

Here q' denotes a quark having a different flavor compared to quark q . Needless to say, every quark line can be replaced by an antiquark line.

We will now give an outline how to calculate matrix elements $\overline{\sum} \Delta |\mathcal{M}|^2$ at LO from first principles. As exemplary case, we consider the QCD Compton process

$$\gamma(p_a, \lambda_a) q(p_b, \lambda_b) \rightarrow q(p_c) g(p_d), \quad (3.17)$$

with λ_a and λ_b denoting the helicities of the photon and the quark, and p_i the four-momenta. Figure 3.2 shows the two Feynman diagrams contributing to the QCD Compton process at $\mathcal{O}(\alpha_{em}\alpha_s)$. We now concentrate on the calculation of the amplitude for the t -channel diagram (1), shown on the left-hand-side (l.h.s.) of Fig. 3.2. The same steps have to be applied for the s -channel diagram (2), shown on the right-hand-side, and for the interference term $\mathcal{M}_1 \mathcal{M}_2^*$, with the

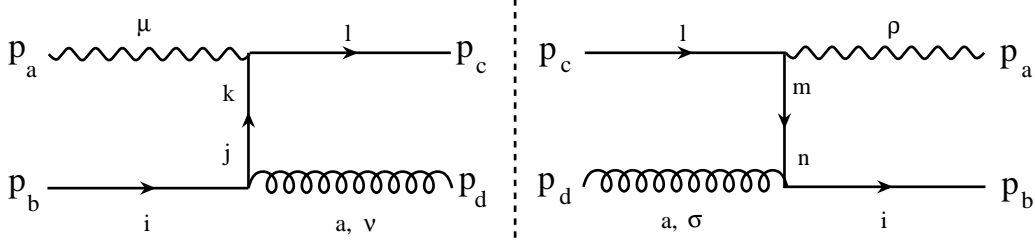


Figure 3.3: Diagram (1) of the QCD Compton process depicted in Fig. 3.2, together with its complex conjugated. Roman letters denote color indices, Greek letters Lorentz indices.

superscript $*$ denoting the complex conjugated. The final result is given by the sum of the contributing diagrams squared

$$[\Delta]|\mathcal{M}|_{\gamma q \rightarrow qg}^2 = [\Delta]|\mathcal{M}_1 + \mathcal{M}_2|^2 = [\Delta] \left[|\mathcal{M}_1|^2 + |\mathcal{M}_2|^2 + \text{Re}(2\mathcal{M}_1\mathcal{M}_2^*) \right]. \quad (3.18)$$

The calculations of all diagrams and interference terms of diagrams are straightforward.

Figure 3.3 shows diagram (1) together with its complex conjugated diagram and all Lorentz (Greek letters) and color (Roman letters) indices. Using the Feynman rules of Appendix A, one gets for the matrix element squared

$$\begin{aligned} |\mathcal{M}_1|^2 &= \sum_{\lambda_c, \lambda_d} \epsilon_\mu(p_a, \lambda_a) \epsilon_\nu(p_d, \lambda_d) \epsilon_\sigma^*(p_d, \lambda_d) \epsilon_\rho^*(p_a, \lambda_a) \\ &\times \bar{u}(p_c, \lambda_c) (g_e \delta_{lk} \gamma^\mu) \left(\delta_{jk} \frac{\not{p}_a - \not{p}_c}{(p_a - p_c)^2} \right) (g_s \gamma^\nu T_{ij}^a) u(p_b, \lambda_b) \\ &\times \bar{u}(p_b, \lambda_b) (g_s \gamma^\sigma T_{ni}^a) \left(\delta_{nm} \frac{\not{p}_a - \not{p}_c}{(p_a - p_c)^2} \right) (g_e \delta_{ml} \gamma^\rho) u(p_c, \lambda_c). \end{aligned} \quad (3.19)$$

As the helicities of the outgoing particles are not observed, we have to sum them. All factors containing the color structure of the process are independent of the γ -matrices and can be calculated separately, obtaining

$$\sum_{a,i,j,k,l,m,n} \delta_{lk} \delta_{jk} T_{ij}^a T_{ni}^a \delta_{nm} \delta_{ml} = \sum_{a,i,j} T_{ij}^a T_{ji}^a = \text{Tr}_c[T^a T^a] = C_A C_F. \quad (3.20)$$

With the help of the projection operators for quarks, given in Eq. (A.1) in Appendix A, we end up with

$$\begin{aligned} |\mathcal{M}_1|^2 &= C_A C_F \frac{g_s^2 g_e^2}{t^2} \sum_{\lambda_d} \epsilon_\mu(p_a, \lambda_a) \epsilon_\nu(p_d, \lambda_d) \epsilon_\sigma^*(p_d, \lambda_d) \epsilon_\rho^*(p_a, \lambda_a) \\ &\times \text{Tr} \left[\not{p}_c \gamma^\mu (\not{p}_a - \not{p}_c) \gamma^\nu \frac{1}{2} \not{p}_b (1 - \lambda_b \gamma_5) \gamma^\sigma (\not{p}_a - \not{p}_c) \gamma^\rho \right]. \end{aligned} \quad (3.21)$$

For the unpolarized gluon in the final state, labeled with four-momentum p_d , the summation over the helicity degrees of freedom λ_d has to be performed, which is usually done by

$$\sum_{\lambda} \epsilon_{\mu}(p, \lambda) \epsilon_{\nu}^*(p, \lambda) = -g_{\mu\nu}. \quad (3.22)$$

This prescription is used in all our calculations. The advantage is that the gluonic and photonic polarization sums are simply replaced by the metric tensor $g_{\mu\nu}$. The price to pay is that one has to calculate additional diagrams involving Faddeev-Popov ghosts to cancel unphysical polarization degrees of freedom. These ghosts show up only in diagrams involving the three-gluon vertex and hence are not subject to the QCD Compton process. To avoid this, one can also use the full expression

$$\sum_{\lambda} \epsilon_{\mu}(p, \lambda) \epsilon_{\nu}^*(p, \lambda) = -g_{\mu\nu} + \frac{p_{\mu} r_{\nu} + p_{\nu} r_{\mu}}{p \cdot r}, \quad (3.23)$$

with an arbitrary momentum r_{μ} fulfilling the condition $r^2 = 0$ and $p \cdot r \neq 0$. With this expression the structure of the Dirac γ -matrices gets more complicated and the calculation can become very time-consuming, especially if more particles are involved like for real corrections.

In Eq. (3.21) the trace of Dirac γ -matrices in $n = 4 - 2\varepsilon$ dimensions can be calculated, for example, using the algebraic computer package TRACER [78], written for the program MATHEMATICA [79]. With the projection onto specified helicity for the incoming photon, as given in Eq. (A.3) of Appendix A, contraction of all Lorentz indices, and the calculation of $|\mathcal{M}_2|^2$ and $\mathcal{M}_1 \mathcal{M}_2^*$ we find the following expressions for the unpolarized and polarized matrix elements squared

$$\begin{aligned} \overline{\sum} |\mathcal{M}|_{\gamma q \rightarrow qg}^2 &= -2C_F \frac{1}{st} \left[s^2 + t^2 - \varepsilon(s+t)^2 \right], \\ \overline{\sum} \Delta |\mathcal{M}|_{\gamma q \rightarrow qg}^2 &= 2C_F \frac{u}{st} \left[2s + u - \varepsilon u \right]. \end{aligned} \quad (3.24)$$

The terms proportional to ε are, of course, negligible at LO, but give finite contributions at NLO, when combined with poles $1/\varepsilon$ and $1/\varepsilon^2$.

Inevitably, in dimensional regularization we have to deal with contributions from hat-momenta, as discussed in Sec. 2.2. However, in LO all hat-momenta can be safely set to zero, as all momenta can be parameterized in such a way, that they have components only in the physical four space-time dimensions.

The next step in the calculation of partonic cross sections is the evaluation of the two-particle inclusive phase space. As we consider di-hadron production, we do not have any unobserved partons at the LO of pQCD, simplifying the calculation. This will be different in NLO, with an additional *unobserved* parton in the final state, and an integration of its momentum over the entire phase space.

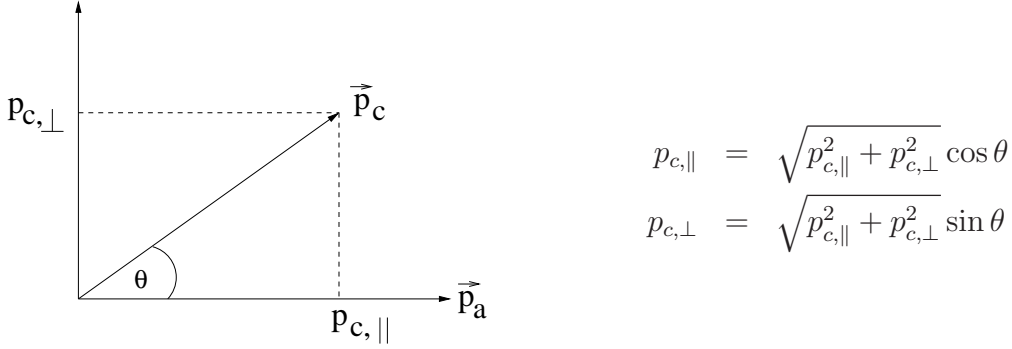


Figure 3.4: The decomposition of the momentum p_c and the definition of the scattering angle θ .

We start with the definition of the two-particle Lorentz-invariant phase space in n dimensions, and evaluate the n -dimensional δ -function ensuring momentum conservation

$$\begin{aligned} dPS_2 &= \int \frac{d^n p_c}{(2\pi)^{n-1}} \frac{d^n p_d}{(2\pi)^{n-1}} (2\pi)^n \delta(p_c^2) \delta(p_d^2) \delta^{(n)}(p_a + p_b - p_c - p_d) \\ &= \frac{1}{(2\pi)^{n-2}} \int d^n p_c \delta(p_c^2) \delta\left((p_a + p_b - p_c)^2\right). \end{aligned} \quad (3.25)$$

Equation (3.25) can be evaluated further in the c.m.s. of the incoming particles a and b , where the following conditions for the spatial parts and zero components of the four-momenta hold true

$$\vec{p}_a + \vec{p}_b = 0, \quad (p_a + p_b)^2 = (p_a^0 + p_b^0)^2 = s. \quad (3.26)$$

The spatial components of p_c can be decomposed into a part parallel to the axis of the incoming partons ($p_{c,||}$) and a $(n-2)$ -dimensional part perpendicular to it ($p_{c,\perp}$), as depicted in Fig. 3.4. The phase space takes now the form

$$dPS_2 = \frac{1}{(2\pi)^{n-2}} \int dp_{c,0} dp_{c,||} dp_{c,\perp}^{n-2} \delta(p_c^2) \delta(s - 2p_{c,0}\sqrt{s}). \quad (3.27)$$

The $(n-2)$ -dimensional components $p_{c,\perp}$ can be evaluated with the use of generalized spherical coordinates, giving

$$dp_{c,\perp}^{n-2} = \frac{\pi^{\frac{n-2}{2}}}{\Gamma\left(\frac{n-2}{2}\right)} (p_{c,\perp}^2)^{\frac{n-4}{2}} dp_{c,\perp}^2. \quad (3.28)$$

Rewriting the argument of the first δ -function as $p_c^2 = p_{c,0}^2 - p_{c,||}^2 - p_{c,\perp}^2$, and

integrating over $p_{c,\perp}^2$ yields

$$dPS_2 = \frac{\pi^{\frac{n-2}{2}}}{(2\pi)^{n-2}} \frac{1}{\Gamma(\frac{n-2}{2})} \frac{1}{2\sqrt{s}} \int dp_{c,0} dp_{c,\parallel} \times (p_{c,0}^2 - p_{c,\parallel}^2)^{\frac{n-4}{2}} \delta\left(\frac{\sqrt{s}}{2} - p_{c,0}\right). \quad (3.29)$$

We now evaluate the $p_{c,0}$ -integration with the use of the δ -function and introduce the scattering angle θ (see Fig. 3.4)

$$dPS_2 = \frac{\pi^{\frac{n-2}{2}}}{(2\pi)^{n-2}} \frac{1}{\Gamma(\frac{n-2}{2})} \frac{1}{2\sqrt{s}} \int d\cos\theta p_{c,0}^{n-3} \sin^{n-4}\theta, \quad (3.30)$$

with $p_{c,0} = \frac{\sqrt{s}}{2}$. It is convenient to re-express any dependence on the scattering angle θ in terms of the Mandelstam variables t and u , defined in Eq. (3.9), via

$$t = -\frac{s}{2}(1 - \cos\theta), \quad \text{and} \quad u = -\frac{s}{2}(1 + \cos\theta). \quad (3.31)$$

The final result for the two-particle phase space in $n = 4 - 2\varepsilon$ dimensions reads

$$\frac{dPS_2}{du dt} = \frac{1}{\Gamma(1 - \varepsilon)} \left(\frac{1}{4\pi}\right)^{1-\varepsilon} \frac{1}{2s} \left(\frac{tu}{s}\right)^{-\varepsilon} \delta(s + t + u). \quad (3.32)$$

In NLO calculations it is customary to use the variables v and w , instead of t and u , defined by

$$v = 1 + \frac{t}{s}, \quad w = -\frac{u}{s+t}. \quad (3.33)$$

As will be discussed in Sec. 3.4, an analytic calculation of the three-particle phase space in NLO requires the introduction of a variable z [80], defined by

$$z = -\frac{\vec{p}_{T,c} \cdot \vec{p}_{T,d}}{p_{T,c}^2}, \quad (3.34)$$

with $\vec{p}_{T,i}$ being the two-dimensional transverse momentum of parton i relative to the beam axis of the two incoming partons. LO contributions and virtual, one-loop corrections at NLO only have two partons in the final state, and their transverse momenta perpendicular to the beam axis have to balance each other due to momentum conservation. Thus, we get the following constraint

$$\vec{p}_{T,c} = -\vec{p}_{T,d} \quad \rightarrow \quad z = 1, \quad (3.35)$$

at the parton level.

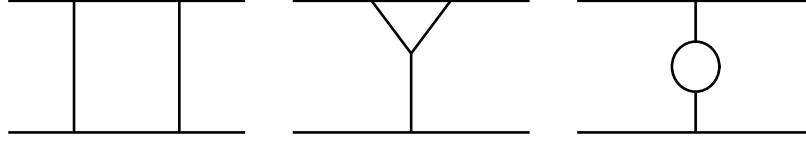


Figure 3.5: Generic diagrams for virtual contributions: box diagrams, vertex corrections and self-energy corrections.

The two-particle phase space differential in v, w , and z is given by

$$\frac{dPS_2}{dv dw dz} = \frac{1}{2\Gamma(1-\varepsilon)} \left(\frac{1}{4\pi}\right)^{1-\varepsilon} \left(\frac{1}{sv(1-w)}\right)^\varepsilon \delta(1-w)\delta(1-z). \quad (3.36)$$

Together with the matrix elements squared, we now have all building blocks for the calculation of partonic cross sections in LO

$$\frac{d\Delta\hat{\sigma}_{ab\rightarrow cd}^{(0)}}{dv dw dz} = \frac{1}{2s} \sum |\Delta\mathcal{M}_{ab\rightarrow cd}|^2 \frac{dPS_2}{dv dw dz}. \quad (3.37)$$

Results for polarized and unpolarized partonic LO cross sections are well known. Explicit expressions for both QCD processes and processes involving also photons, polarized and unpolarized, can be found, for example, in [31]. Phenomenological studies based on LO results have been performed, for instance, in [81, 82, 83] and most recently in [23, 84]. In Chapter 4 and 6 these results will be compared to our NLO predictions.

3.3 Virtual Contributions

At NLO, one class of corrections to the Born cross sections arise, if additional unobserved - virtual - particles are emitted and again reabsorbed in the scattering process. Each interaction brings in an additional coupling constant g_s , yielding an extra α_s for each virtual, one-loop diagram. Therefore at NLO, i.e., $\mathcal{O}(\alpha_s^2\alpha_{em})$, one has to consider only the interference of virtual and Born diagrams. One-loop amplitudes squared are $\mathcal{O}(\alpha_s^3\alpha_{em})$, and hence part of a next-to-next-to-leading order calculation, which is far beyond the scope of this work.

Three topological different diagrams are possible, which are shown schematically in Fig. 3.5: box diagrams, vertex corrections and self-energy corrections. Each line can stand for a photon, gluon or quark, taking into account that only $q\bar{q}\gamma$ -, $q\bar{q}g$ -, and ggg -vertices are possible. Whereas box diagrams are UV finite and not subject to the renormalization procedure, vertex corrections and self-energies exhibit IR and UV divergencies, and therefore require a proper renormalization. Throughout this work we adopt the $\overline{\text{MS}}$ scheme introduced in Sec. 2.2.

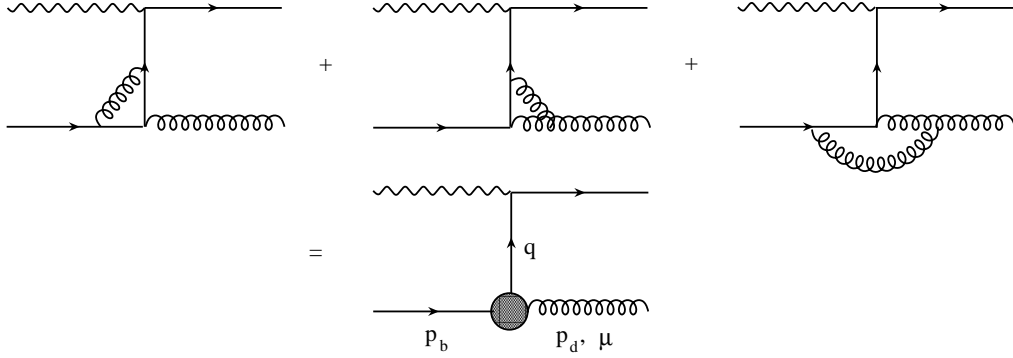


Figure 3.6: Vertex corrections at the qgq -vertex for the process $\gamma q \rightarrow qg$.

Since no additional particles are present in the final state, we can employ the usual two-particle phase space and kinematics for $2 \rightarrow 2$ Born diagrams introduced in the previous Section, see Eq. (3.36). The virtual corrections to the [polarized] cross section read

$$\begin{aligned} \frac{d\hat{\sigma}_{ab \rightarrow cd}^{virt}}{dv dw dz} &= \frac{1}{2s} \frac{dPS_2}{dv dw dz} \overline{\sum} |\mathcal{M}_v \mathcal{M}_b^*|_{ab \rightarrow cd} \delta(1-w) \delta(1-z) \\ \frac{d\Delta\hat{\sigma}_{ab \rightarrow cd}^{virt}}{dv dw dz} &= \frac{1}{2s} \frac{dPS_2}{dv dw dz} \overline{\sum} \Delta |\mathcal{M}_v \mathcal{M}_b^*|_{ab \rightarrow cd} \delta(1-w) \delta(1-z), \end{aligned} \quad (3.38)$$

with $(\Delta)|\mathcal{M}_v \mathcal{M}_b^*|_{ab \rightarrow cd}$ the appropriate interference matrix elements for boxes, vertices, and self-energies, and $\overline{\sum}$ the appropriate summation and averaging over unobserved color and spin degrees of freedom. Note that the virtual cross sections are proportional to $\delta(1-w)\delta(1-z)$ as for LO contributions.

3.3.1 Vertex Corrections and Self-Energies

In vertex corrections we have to take into account the emission and reabsorption of an additional gluon. Figure 3.6 shows the three contributions for such corrections in the example of the QCD Compton process for the qgq -vertex. Instead of computing each diagram on its own, including appropriate counter terms as discussed in Sec. 2.2, we can exploit renormalized vertex and self-energy insertions listed in [85]. This amounts to using “modified” Feynman rules for the “blob” indicated in Fig. 3.6, which greatly facilitates the computations. In practice, we simply have to replace the Feynman rules for the bare quark-gluon vertex in Appendix A by the renormalized one

$$-ig_s \gamma^\mu \rightarrow -ig_s \frac{\alpha_s}{4\pi} \Lambda^\mu, \quad (3.39)$$

where Λ^μ is a function of the four-momenta p_b , p_d , and q as well as the renormalization scale μ_r . In this way, all UV singularities are properly dealt with. However, the final expression still contains IR poles, which are handled within a later step of the calculation. The explicit form of Λ^μ depends on which leg goes off-shell. Instead of reproducing the rather lengthy expressions for Λ^μ , we refer the reader to Table B.II. of [85]. A similar replacement can be done for the ghost-gluon and the three-gluon vertex. However, in the direct case with only two processes, photon gluon fusion and QCD Compton, these vertices are absent and thus do not need to be considered here.

Like for vertex corrections, similar renormalized insertions exist for self-energy contributions, which read in the case of the quark propagator

$$-i\not{p}C_F\frac{\alpha_s}{4\pi}\Sigma(p^2). \quad (3.40)$$

For the gluon propagator one has

$$i\frac{\alpha_s}{4\pi}\Pi^{\mu\nu}(p). \quad (3.41)$$

The explicit expressions for $\Sigma(p^2)$ and $\Pi^{\mu\nu}(p)$ differ for on- and off-shell lines, i.e., $p^2 = 0$ and $p^2 \neq 0$, respectively. Again, they can be found in [85].

In the case of self-energies for internal lines, the procedure for calculating matrix elements is rather straightforward. E.g., considering the self-energy corrections to the internal quark propagator in the QCD Compton process, which have been calculated in Sec. 2.2, the interference of the virtual diagram with the appropriate tree level diagram reads

$$\begin{aligned} [\mathcal{M}_s\mathcal{M}_b^*](\lambda_a, \lambda_b) &= C_A C_F g_s^2 g_e^2 \sum_{\lambda_d} \epsilon_\mu(p_a, \lambda_a) \epsilon_\nu(p_d, \lambda_d) \epsilon_\sigma^*(p_d, \lambda_d) \epsilon_\rho^*(p_a, \lambda_a) \\ &\times \text{Tr} \left\{ \not{p}_c \gamma^\mu \frac{(\not{p}_a - \not{p}_c)}{(p_a - p_c)^2} \left[C_F (\not{p}_a - \not{p}_c) \frac{\alpha_s}{4\pi} \Sigma((p_a - p_c)^2) \right] \right. \\ &\times \left. \frac{(\not{p}_a - \not{p}_c)}{(p_a - p_c)^2} \gamma^\rho \frac{1}{2} \not{p}_b (1 - \lambda_b \gamma_5) \gamma^\sigma (\not{p}_a - \not{p}_c) \gamma^\nu \right\}. \quad (3.42) \end{aligned}$$

While the calculation is straightforward for internal lines, virtual corrections to external legs have to be treated with special care. Due to an additional propagator with the momentum of the external line, e.g., $1/p_b^2$, this would naively result in an infinite quantity. However, in combination with the proper insertion from [85], this artificial pole cancels and one gets a finite quantity in the end. Technically, this is done by putting them off the mass-shell, e.g., $p_b^2 = q^2$. Then all terms proportional to q^2 are kept explicitly and cancel at the end of the calculation. External lines receive an additional factor 1/2 from the renormalization procedure, as is discussed, e.g., in [31].

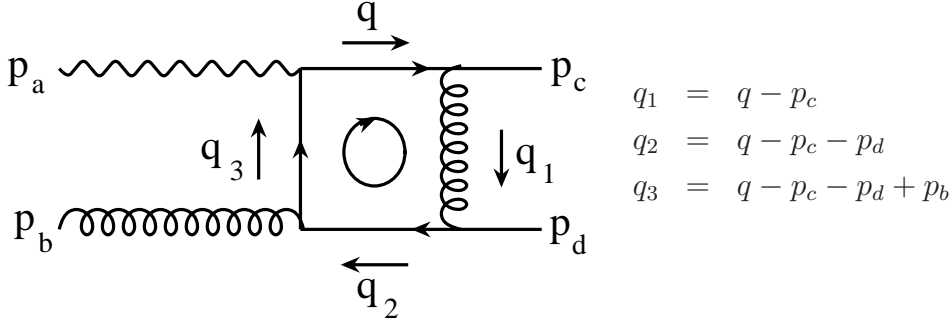


Figure 3.7: Example for a box diagram occurring in NLO photoproduction calculations. The loop momentum q is unrestricted.

3.3.2 Box Contributions

As mentioned before, box diagrams have no UV divergencies and thus are not subject to the renormalization procedure. However, IR singularities show up as single poles in $1/\varepsilon$ and double poles $1/\varepsilon^2$ in combination with collinear singularities. No precalculated building blocks exist in literature, so they have to be calculated from scratch. To exemplify this, we outline the steps necessary to evaluate one of the one-loop box contributions to photon-gluon fusion, depicted in Fig. 3.7.

With the Feynman rules of Appendix A one ends up with the following structure for the matrix element

$$\mathcal{M}_{\text{box}} \sim \left[\int \frac{d^n q}{(2\pi)^n} \gamma^\rho \frac{\not{q}}{q^2} \gamma^\mu \frac{\not{q}_3}{q_3^2} \gamma^\nu \frac{\not{q}_2}{q_2^2} \gamma_\rho \frac{1}{q_1^2} \right]. \quad (3.43)$$

q is the unobserved loop momentum and can take any value from zero to infinity. Now, the main task is the computation of tensor integrals. For our example the integral takes the form

$$\begin{aligned} \int \frac{d^n q}{(2\pi)^n} \frac{q^\alpha q_3^\beta q_2^\gamma}{q^2 q_1^2 q_2^2 q_3^2} &= \int \frac{d^n q}{(2\pi)^n} \frac{q^\alpha q^\beta q^\gamma}{q^2 q_1^2 q_2^2 q_3^2} \\ &- (p_c + p_d - p_b)^\beta \int \frac{d^n q}{(2\pi)^n} \frac{q^\alpha q^\gamma}{q^2 q_1^2 q_2^2 q_3^2} \\ &- (p_c + p_d)^\gamma \int \frac{d^n q}{(2\pi)^n} \frac{q^\alpha q^\beta}{q^2 q_1^2 q_2^2 q_3^2} \\ &+ (p_c + p_d - p_b)^\beta (p_c + p_d)^\gamma \int \frac{d^n q}{(2\pi)^n} \frac{q^\alpha}{q^2 q_1^2 q_2^2 q_3^2}. \end{aligned} \quad (3.44)$$

These tensor integrals with some definite Lorentz structure in the numerator of the integrand can be decomposed into a set of calculable scalar integrals with

the help of the Passarino-Veltman decomposition [86, 87]. This procedure relies on the fact that the Lorentz structure of a tensor integral is determined by the external momenta and the metric tensor $g^{\mu\nu}$, which are the only quantities in the calculation exhibiting Lorentz indices. All relevant formulas for this decomposition can be found, e.g., in Appendix C of [31]. With the help of this procedure one ends up with a finite number of scalar integrals. They are tabulated and can be found in [85, 88, 89].

After applying this procedure and calculating the scalar integrals, \mathcal{M}_{box} no longer depends on the loop momentum q . The further evaluation is straightforward as in LO, but tedious and lengthy. \mathcal{M}_{box} has to be combined with the appropriate Born amplitude \mathcal{M}_b^* to obtain the result for $\text{Re}(\mathcal{M}_{\text{box}}\mathcal{M}_b^*)$.

3.4 Real Contributions

In addition to the virtual contributions just discussed, a full NLO calculation includes also real contributions. In this class of processes a third particle is emitted, i.e., one has to deal with a $2 \rightarrow 3$ body kinematics,

$$a(p_a) + b(p_b) \rightarrow c(p_c) + d(p_d) + e(p_e), \quad (3.45)$$

with $a - e$ denoting the massless partons, and p_i their corresponding four-momenta. Partons c and d shall hadronize into the two observed hadrons in the fragmentation process, and parton e remains unobserved and hence has to be integrated over its entire phase space.

The computation with largely analytical methods becomes feasible thanks to the introduction of the variable z [80], defined in Eq. (3.34). This is, to avoid some certain singular configurations of two final state partons. For instance, momenta p_c parallel to p_d correspond to negative values of z . In this case, the partonic cross section is incomplete and contains uncanceled poles, which would require the introduction of additional non-perturbative functions describing the simultaneous fragmentation of a single parton into two hadrons. Situations, where the momentum p_d is parallel to the direction of the incoming photon, are characterized by $z = 0$. For the phase space integrations we therefore restrict ourselves to

$$z > z_{\text{min}} > 0, \quad (3.46)$$

equivalent to the condition that the two hadrons are produced by partons in opposite hemispheres.

In contrast to the $2 \rightarrow 2$ processes like LO processes and virtual corrections, characterized by three Mandelstam variables and one constraint, we now need a

set of ten variables, which are chosen as follows:

$$\begin{aligned}
s &= (p_a + p_b)^2, & t &= (p_a - p_c)^2, & u &= (p_b - p_c)^2, \\
s_{12} &= (p_c + p_d)^2, & t_2 &= (p_a - p_d)^2, & u_2 &= (p_b - p_d)^2, \\
s_{13} &= (p_c + p_e)^2, & t_3 &= (p_a - p_e)^2, & u_3 &= (p_b - p_e)^2, \\
s_{23} &= (p_d + p_e)^2.
\end{aligned} \tag{3.47}$$

This set of course is not unique, but useful for our purposes. Due to momentum conservation, $p_a + p_b = p_c + p_d + p_e$, the variables have the following constraints

$$\begin{aligned}
t_3 &= -s - t - t_2 \\
u_3 &= -s - u - u_2 \\
s_{23} &= s + t + u \\
s_{13} &= s + t_2 + u_2 \\
s_{12} &= -s - t - t_2 - u - u_2.
\end{aligned} \tag{3.48}$$

As a consequence, only five of the ten Mandelstam variables are actually independent. In our calculations we make extensive use of rewriting variables in terms of different sets of variables to integrate the matrix elements over phase space analytically.

Before going into the details of how to integrate analytically the $2 \rightarrow 3$ matrix elements over phase space, we shall list the contributing processes at $\mathcal{O}(\alpha_{em}\alpha_s^2)$ first. In the case, where the quasi-real photon interacts directly with a parton of the nucleon, the relevant subprocesses at NLO are

$$\begin{aligned}
\gamma q &\rightarrow qgg \\
\gamma g &\rightarrow q\bar{q}g \\
\gamma q &\rightarrow q'\bar{q}'q \\
\gamma q &\rightarrow q\bar{q}q,
\end{aligned} \tag{3.49}$$

where the first two are the QCD Compton and the photon-gluon fusion process in Eqs. (3.14) and (3.15), with emission of an additional gluon. The other two processes in Eq. (3.49) show up in NLO for the first time. For processes, where the photon resolves into its partonic structure, we have ten additional processes

$$\begin{aligned}
qq' &\rightarrow qq'g \\
q\bar{q} &\rightarrow q'\bar{q}'g \\
qq &\rightarrow qqg \\
q\bar{q} &\rightarrow q\bar{q}g
\end{aligned}$$

$$\begin{aligned}
q\bar{q} &\rightarrow ggg \\
qg &\rightarrow qgg \\
qg &\rightarrow qq'\bar{q}' \\
qg &\rightarrow qq\bar{q} \\
gg &\rightarrow q\bar{q}g \\
gg &\rightarrow ggg.
\end{aligned} \tag{3.50}$$

Needless to say, any quark line can be replaced by an antiquark line. The processes in Eqs. (3.50) are of order $\mathcal{O}(\alpha_s^3)$. However, in combination with photonic parton distributions, which are $\mathcal{O}(\alpha_{em}/\alpha_s)$, these contributions enter already at $\mathcal{O}(\alpha_{em}\alpha_s^2)$. In Eqs. (3.49) and (3.50), the two observed hadrons can in principle be produced by any of the three particles in the final state, making it indispensable to take into account all combinatorical possibilities. For instance, in the first process of (3.50), $qq' \rightarrow qq'g$, the hadrons can be produced either by the q and q' , by q and g , or by q' and g . In addition, the two partons have to be exchanged among each other, since we can not select the ordering of the partons for fragmentation to hadron H_1 and H_2 .

The calculation of the matrix elements squared for all $2 \rightarrow 3$ processes given in Eqs. (3.49) and (3.50) is straightforward, but tedious. It follows the steps outlined for the computation of the LO QCD Compton process in Sec. 3.2. The relevant traces of Dirac γ -matrices are again conveniently computed in n dimensions with the help of the computer algebra tool TRACER [78]. Both the Dirac algebra and the color structure of each contribution are much more involved than in a simple LO calculation. The results for the matrix elements squared are too lengthy to be given here explicitly, but are available upon request.

In addition, integrating the expressions for matrix elements squared analytically over phase space is very cumbersome, as we will demonstrate in some detail next. Thus, in the analytic calculation we concentrate on the direct part of the spin-dependent cross section for two-hadron photoproduction, as there are less processes. Nevertheless, these results are very important, both theoretically and phenomenologically. On the one hand, the analytic results will serve as an important check on more versatile Monte-Carlo (MC) techniques like the “two cut-off phase space slicing method” [32], discussed in Chapter 5. On the other hand, it was demonstrated in our LO study [23], that the direct photon part is responsible for the main features of the experimentally relevant spin asymmetry, defined in Eq. (3.6), and its sensitivity to the polarized gluon density at fixed-target experiments like COMPASS and HERMES.

With one additional particle in the final state, the “unphysical” hat-components in the $(n-4)$ -dimensional subspace, introduced within dimensional regularization in Eq. (2.25), cannot be disregarded, as it was the case for $2 \rightarrow 2$ processes. In Sec. 3.4.2 we will show that the phase space combined with a factor, e.g., \hat{p}_d^2

will be proportional to ε , giving a finite contribution in combination with a $1/\varepsilon$ pole. For a proper computation of the three-particle phase space we choose the c.m.s. of the two incoming partons, and parameterize the momenta in such a way that only final state partons have components in the $(n-4)$ dimensions. Due to momentum conservation, \hat{p}_c can be eliminated, and we get

$$\hat{p}_d + \hat{p}_e = 0. \quad (3.51)$$

With $p_d^2 = 0 = \hat{p}_d^2 + \hat{\hat{p}}_d^2$, the following relations for the $(n-4)$ -components hold true

$$\begin{aligned} \hat{p}_d^2 &= -\hat{\hat{p}}_d^2 \\ \hat{p}_e^2 &= -\hat{\hat{p}}_d^2 \\ \hat{p}_d \cdot \hat{p}_e &= \hat{\hat{p}}_d^2. \end{aligned} \quad (3.52)$$

Now, the next Subsection is dedicated to the evaluation of the three-particle phase space without hat-momenta, whereas in Subsec. 3.4.2 we include an additional factor $\hat{\hat{p}}_d^2$.

3.4.1 Three-body Phase Space without Hat-Momenta

In the derivation of the phase space in the absence of hat-momenta we closely follow [80, 90]. In analogy to the two-particle phase space defined in Eq. (3.25) we start with the definition of the phase space with three particles in the final state

$$\begin{aligned} dPS_3 &= \int \frac{d^n p_c}{(2\pi)^{n-1}} \frac{d^n p_d}{(2\pi)^{n-1}} \frac{d^n p_e}{(2\pi)^{n-1}} (2\pi)^n \\ &\times \delta^{(n)}(p_a + p_b - p_c - p_d - p_e) \delta(p_c^2) \delta(p_d^2) \delta(p_e^2). \end{aligned} \quad (3.53)$$

To proceed, we split up the full $2 \rightarrow 3$ phase space into a $2 \rightarrow 2$ scattering, followed by a $1 \rightarrow 2$ decay into the partons d and e . This is done by defining $p_{de} \equiv p_d + p_e$ and inserting an integration over the invariant mass s_{23} of the pair (d, e) , defined in Eq. (3.47):

$$1 = \int ds_{23} \delta(s_{23} - p_{de}^2). \quad (3.54)$$

This yields for the three-particle phase space

$$\begin{aligned} dPS_3 &= \frac{1}{(2\pi)^{2n-3}} \int d^n p_c d^n p_{de} ds_{23} \delta^{(n)}(p_a + p_b - p_c - p_{de}) \\ &\times \delta(p_c^2) \delta(s_{23} - p_{de}^2) \times dPS_2, \end{aligned} \quad (3.55)$$

with

$$\begin{aligned} dPS_2 &\equiv \int d^n p_d d^n p_e \delta(p_d^2) \delta(p_e^2) \delta^{(n)}(p_d + p_e - p_{de}) \\ &= \int d^n p_d \delta(p_d^2) \delta((p_{de} - p_d)^2) \end{aligned} \quad (3.56)$$

being the splitting of a parton with momentum p_{de} in the two partons d and e with momenta p_d and p_e . We go to the c.m.s. of the pair (d, e) , where $p_{de} = (\sqrt{s_{23}}, \vec{0})$ and $p_d = (E_d, \vec{p}_d)$. In this frame the $1 \rightarrow 2$ phase space is

$$dPS_2 = \int d^n p_d \delta(p_d^2) \delta(s_{23} - 2\sqrt{s_{23}}E_d). \quad (3.57)$$

Using n -dimensional polar coordinates for p_d , we get for the differential

$$\begin{aligned} d^n p_d &= dE_d |\vec{p}_d|^{n-2} d|\vec{p}_d| d\phi \\ &\times \sin \theta_{n-3} d\theta_{n-3} \sin^2 \theta_{n-4} d\theta_{n-4} \dots \sin^{n-3} \theta_1 d\theta_1. \end{aligned} \quad (3.58)$$

Now, the integration over $(n-5)$ components can be performed [91]

$$\begin{aligned} \int_0^\pi \sin \theta_{n-3} d\theta_{n-3} \int_0^\pi \sin^2 \theta_{n-4} d\theta_{n-4} \dots \int_0^\pi \sin^{n-5} \theta_3 d\theta_3 = \\ \prod_{j=1}^{n-5} \int_0^\pi \sin^j \xi_j d\xi_j = \frac{\pi^{n/2-5/2}}{\Gamma(\frac{n}{2} - \frac{3}{2})}. \end{aligned} \quad (3.59)$$

Inserting Eqs. (3.58) and (3.59) in Eq. (3.57), and making use of the δ -functions, the $1 \rightarrow 2$ phase space reads

$$dPS_2 = (p_{de}^2)^{n/2-2} I_{\text{unp}}(\theta_i), \quad (3.60)$$

with

$$I_{\text{unp}}(\theta_i) \equiv \frac{\pi^{n/2-3/2}}{2^{n-2} \Gamma(\frac{n}{2} - \frac{3}{2})} \int_0^\pi \sin^{n-4} \theta_2 d\theta_2 \int_0^\pi \sin^{n-3} \theta_1 d\theta_1. \quad (3.61)$$

To proceed, we insert Eq. (3.60) in Eq. (3.55) and integrate over p_{de} and s_{23} with the help of the δ -functions. This yields for the complete three-particle phase space

$$dPS_3 = \frac{1}{(2\pi)^{2n-3}} \underbrace{\int d^n p_c \delta(p_c^2) [(p_a + p_b - p_c)^2]^{n/2-2}}_{I_{1,\text{unp}}} I_{\text{unp}}(\theta_i). \quad (3.62)$$

With the following parameterization for the n -momentum p_c

$$p_c = E_c(1, 0, \cos \alpha_2 \sin \alpha_1, \cos \alpha_1, \dots), \quad (3.63)$$

where the ellipsis denotes arbitrary spatial-components in the $(n-4)$ -dimensional subspace, we get

$$\begin{aligned}
I_{1,\text{unp}} &= \pi \int dE_c \int d|\vec{p}_c|^2 |\vec{p}_c|^{n-3} \left[\prod_{j=1}^{n-4} \int_0^\pi \sin^j \alpha_{n-2-j} d\alpha_{n-2-j} \right] \\
&\times \int_0^\pi \sin^{n-3} \alpha_1 d\alpha_1 \delta(E_c^2 - |\vec{p}_c|^2) [s+t+u]^{n/2-2} \\
&= \frac{\pi^{n/2-1}}{\Gamma(\frac{n}{2}-1)} \int dE_c^{n-3} \int_{-1}^1 \sin^{n-4} \alpha_1 d(\cos \alpha_1) [s+t+u]^{n/2-2}. \quad (3.64)
\end{aligned}$$

We now go to the c.m.s. of the two incoming partons a and b , defined by

$$p_a = \frac{\sqrt{s}}{2}(1, 0, 0, 1, \vec{0}), \quad p_b = \frac{\sqrt{s}}{2}(1, 0, 0, -1, \vec{0}). \quad (3.65)$$

The Mandelstam variables t and u in Eq. (3.9) can be expressed as

$$\begin{aligned}
t &= (p_c - p_a)^2 = -\sqrt{s}E_c(1 - \cos \alpha_1), \\
u &= (p_c - p_b)^2 = -\sqrt{s}E_c(1 + \cos \alpha_1). \quad (3.66)
\end{aligned}$$

With the definition of the auxiliary variables v and w , see Eq. (3.33) in Sec. 3.2, we find for the integration variables in Eq. (3.64)

$$\begin{aligned}
E_c &= \frac{\sqrt{s}}{2}(1 - v + vw), \\
\cos \alpha_1 &= -\frac{1 - v - vw}{1 - v + vw}. \quad (3.67)
\end{aligned}$$

Substituting in Eq. (3.64) the integration variables from $(E_c, \cos \alpha_1)$ to (v, w) , the Jacobian yields

$$\mathcal{J} = \det \begin{pmatrix} \frac{\partial \cos \alpha_1}{\partial v} & \frac{\partial E_c}{\partial v} \\ \frac{\partial \cos \alpha_1}{\partial w} & \frac{\partial E_c}{\partial w} \end{pmatrix} = \frac{\sqrt{s}v}{1 - v + vw}. \quad (3.68)$$

Finally, with $n = 4 - 2\varepsilon$ the full three-particle phase space reads

$$\begin{aligned}
dPS_3 &= \frac{1}{(2\pi)^{5-4\varepsilon}} \frac{\pi^{3/2-2\varepsilon}}{2^{3-2\varepsilon}\Gamma(1-\varepsilon)\Gamma(\frac{1}{2}-\varepsilon)} s^{1-2\varepsilon} \\
&\times \int dv \int dw (1-v)^{-\varepsilon} (1-w)^{-\varepsilon} v^{1-2\varepsilon} w^{-\varepsilon} \\
&\times \int_0^\pi \sin^{-2\varepsilon} \theta_2 d\theta_2 \int_0^\pi \sin^{1-2\varepsilon} \theta_1 d\theta_1. \quad (3.69)
\end{aligned}$$

This result is in agreement with Eq. (B.7) in [92], and is applicable for studies of single-inclusive hadron or jet production at NLO, see Refs. [93, 94].

However, Eq. (3.69) is not appropriate for an analysis for two observed hadrons in the final state coming from two partons in the fragmentation process. To proceed, we need to introduce a variable z and an auxiliary space-like vector m [80], defined via

$$z \equiv m \cdot p_d, \quad m \equiv \frac{p_c s + p_b t + p_a u}{tu}. \quad (3.70)$$

With the help of light-cone coordinates it is easy to show that

$$z = -\frac{\vec{p}_{T,c} \cdot \vec{p}_{T,d}}{p_{T,c}^2}, \quad (3.71)$$

in the c.m.s. of the two incoming partons. $\vec{p}_{T,c}$ and $\vec{p}_{T,d}$ denote the transverse momenta of the two partons, which fragment collinearly in the two observed hadrons relative to the beam axis. This expression was already introduced in Eq. (3.34). As already mentioned at the beginning of this Section, some certain singular regions (collinear hadrons, hadron H_2 parallel to the beam axis) have to be avoided by restricting $z > 0$.

To continue, the phase space is further evaluated in the rest frame of p_d and p_e , where we choose p_a , p_b , and p_c in such a way that they have non-vanishing components only in two spatial directions

$$\begin{aligned} p_a &= \frac{sv}{2\sqrt{s_{23}}}(1, 0, \sin \psi, \cos \psi, \dots), \\ p_b &= \frac{s(1-vw)}{2\sqrt{s_{23}}}(1, 0, -\sin \psi, \cos \psi, \dots), \\ p_c &= \frac{s(1-v+vw)}{2\sqrt{s_{23}}}(1, 0, \sin \psi', \cos \psi', \dots), \\ p_d &= \frac{\sqrt{s_{23}}}{2}(1, p_x, \cos \theta_2 \sin \theta_1, \cos \theta_1, \hat{p}_d), \\ p_e &= \frac{\sqrt{s_{23}}}{2}(1, -p_x, -\cos \theta_2 \sin \theta_1, -\cos \theta_1, -\hat{p}_d). \end{aligned} \quad (3.72)$$

Here, the ellipsis in the parameterization of p_a , p_b , and p_c denotes zeros in the $(n-4)$ -dimensional components. \hat{p}_d denotes the $(n-4)$ -dimensional components for parton d , and p_x is arbitrary. With the definition of the variables v and w ,

see Eq. (3.33) in Sec. 3.2, we find

$$\begin{aligned}
\cos \psi &= \sqrt{\frac{w(1-v)}{1-vw}}, \\
\sin \psi &= \sqrt{\frac{1-w}{1-vw}}, \\
\cos \psi' &= \frac{1+v-vw}{1-v+vw} \cos \psi, \\
\sin \psi' &= -\frac{1-v-vw}{1-v+vw} \sin \psi,
\end{aligned} \tag{3.73}$$

and for s_{23} , see Eqs. (3.47) and (3.72),

$$s_{23} = (p_d + p_e)^2 = s + t + u = sv(1-w). \tag{3.74}$$

Using the parameterization in Eq. (3.72), we find

$$m = \left[\frac{s}{tu} \right]^{1/2} \left(\sqrt{\frac{w(1-v)}{1-w}}, 0, 0, \sqrt{\frac{1-vw}{1-w}}, \hat{0} \right). \tag{3.75}$$

Introducing the identity

$$1 = \int dz \delta(z - m \cdot p_d), \tag{3.76}$$

and inserting it into the three-particle phase space, Eq. (3.69), yields

$$\begin{aligned}
dPS_3 &= \frac{1}{(2\pi)^{5-4\varepsilon}} \frac{\pi^{3/2-2\varepsilon}}{2^{3-2\varepsilon} \Gamma(1-\varepsilon) \Gamma(\frac{1}{2}-\varepsilon)} s^{1-2\varepsilon} \\
&\times \int dv \int dw (1-v)^{-\varepsilon} (1-w)^{-\varepsilon} v^{1-2\varepsilon} w^{-\varepsilon} \\
&\times \int d\theta_2 \sin^{-2\varepsilon} \theta_2 \int d\theta_1 \sin^{1-2\varepsilon} \theta_1 \int dz \delta(z - m \cdot p_d).
\end{aligned} \tag{3.77}$$

The integration over the angle θ_1 is trivial, since $z = \frac{1}{2}(1 - \frac{\cos \theta_1}{\cos \psi})$, which also gives us an upper and lower bound for the variable z :

$$z_{\max/\min} = \frac{1}{2} \left(1 \pm \frac{1}{\cos \psi} \right). \tag{3.78}$$

After evaluation of the θ_1 -integration, one gets for the three-body phase space

$$\begin{aligned}
 dPS_3 &= \frac{1}{(2\pi)^{5-4\varepsilon}} \frac{\pi^{3/2-2\varepsilon}}{2^{3-2\varepsilon}\Gamma(1-\varepsilon)\Gamma(\frac{1}{2}-\varepsilon)} s^{1-2\varepsilon} \\
 &\times \int dv \int dw (1-v)^{-\varepsilon} (1-w)^{-\varepsilon} v^{1-2\varepsilon} w^{-\varepsilon} 2 \cos \psi \\
 &\times \underbrace{\left(\frac{1-w+4w(1-v)z(1-z)}{1-vw} \right)^{-\varepsilon}}_{\equiv g(z)} \int dz \int d\theta_2 \sin^{-2\varepsilon} \theta_2. \quad (3.79)
 \end{aligned}$$

With the use of the identity [95]

$$\Gamma(2x) = \frac{2^{2x-1}}{\sqrt{\pi}} \Gamma(x) \Gamma\left(x + \frac{1}{2}\right), \quad (3.80)$$

one ends up with the following expression for the phase space differential in the variables v , w and z

$$\begin{aligned}
 \frac{dPS_3}{dv dw dz} &= \frac{s}{(4\pi)^4 \Gamma(1-2\varepsilon)} \left(\frac{4\pi}{s} \right)^{2\varepsilon} (1-v)^{-\varepsilon} (1-w)^{-\varepsilon} v^{1-2\varepsilon} w^{-\varepsilon} \\
 &\times 2 \cos \psi g(z)^{-\varepsilon} \int_0^\pi d\theta_2 \sin^{-2\varepsilon} \theta_2. \quad (3.81)
 \end{aligned}$$

This result can also be found in [80, 90, 96], and serves as starting point for any further calculation. The majority of terms in the matrix elements squared for real processes can be integrated with Eq. (3.81), except the terms containing a factor \hat{p}_d^2 , which will be treated in Subsec. 3.4.2.

Once one has the [unpolarized] matrix elements in terms of the set of Mandelstams in Eq. (3.47), the θ_2 -integration has to be performed. For a proper treatment of all singularities arising in virtual and real contributions, one has to introduce distributions in terms of δ -functions and so-called “plus-distributions” in the variables w and z , defined in Subsec. 3.4.3. This greatly complicates the analytical phase space calculations, and is much more involved, as it is the case for single-inclusive phase space calculations, where only distributions in w are present.

3.4.2 Three-body Phase Space including Hat-Momenta

Here, we demonstrate how to perform the phase space integrations in the presence of an additional four-component part \hat{p}_d^2 , showing up in some terms of polarized

matrix elements squared, i.e., we compute

$$\begin{aligned} d\widehat{PS}_3 &= \int \frac{d^n p_c}{(2\pi)^{n-1}} \frac{d^n p_d}{(2\pi)^{n-1}} \frac{d^n p_e}{(2\pi)^{n-1}} (2\pi)^n \\ &\times \delta^{(n)}(p_a + p_b - p_c - p_d - p_e) \delta(p_c^2) \delta(p_d^2) \delta(p_e^2) \hat{p}_d^2. \end{aligned} \quad (3.82)$$

Like before, we decompose the phase space into a $2 \rightarrow 2$ scattering followed by a $1 \rightarrow 2$ decay, and follow closely the calculation in the previous Subsection, the difference being the extra factor \hat{p}_d^2 in Eq. (3.57). To proceed, we choose the following parameterization for \hat{p}_d

$$\hat{p}_d = p_d^0(1, \cos \theta_3 \sin \theta_2 \sin \theta_1, \cos \theta_2 \sin \theta_1, \cos \theta_1), \quad (3.83)$$

and easily obtain

$$\hat{p}_d^2 = (p_d^0)^2 \sin^2 \theta_1 \sin^2 \theta_2 \sin^2 \theta_3. \quad (3.84)$$

Hence the usual angular integration measure is modified

$$\prod_{l=1}^{n-2} \sin^{n-l-2} \theta_l d\theta_l \rightsquigarrow \prod_{l=1}^3 \sin^{n-l} \theta_l d\theta_l \times \prod_{l=4}^{n-2} \sin^{n-l-2} \theta_l d\theta_l. \quad (3.85)$$

After integrating the components for $l = 3, \dots, n-2$ with the help of the δ -functions, and after parameterizing p_d in polar coordinates, $d\widehat{PS}_2$ has the form

$$d\widehat{PS}_2 = (p_{de}^2)^{n/2-1} \underbrace{\frac{\pi^{n/2-3/2} \Gamma(\frac{n}{2}-1)}{2^n \Gamma(\frac{n}{2}-2) \Gamma(\frac{n}{2}-\frac{1}{2})} \int_0^\pi \sin^{n-2} \theta_2 d\theta_2 \int_0^\pi \sin^{n-1} \theta_1 d\theta_1}_{I_{\text{pol}}(\theta_i)}. \quad (3.86)$$

The full three-body phase space including an additional factor \hat{p}_d reads

$$d\widehat{PS}_3 = \frac{1}{(2\pi)^{2n-3}} \int d^n p_c \delta(p_c^2) \left[(p_a + p_b - p_c)^2 \right]^{n/2-1} I_{\text{pol}}(\theta_i). \quad (3.87)$$

The next steps are similar to the phase space calculation without hat-momenta, Eqs. (3.63)-(3.68). Rewritten in terms of v , w , and ε , $d\widehat{PS}_3$ has the form

$$\begin{aligned} d\widehat{PS}_3 &= \frac{1}{(2\pi)^{5-4\varepsilon}} \frac{\pi^{3/2-2\varepsilon}}{2^{5-2\varepsilon} \Gamma(\frac{3}{2}-\varepsilon) \Gamma(-\varepsilon)} s^{2-2\varepsilon} \\ &\times \int dv \int dw (1-v)^{-\varepsilon} (1-w)^{1-\varepsilon} v^{2-2\varepsilon} w^{-\varepsilon} \\ &\times \int_0^\pi \sin^{3-2\varepsilon} \theta_1 d\theta_1 \int_0^\pi \sin^{2-2\varepsilon} \theta_2 d\theta_2. \end{aligned} \quad (3.88)$$

With the parameterization of momenta in Eq. (3.72), and after introducing again the variable z via the identity of Eq. (3.76), we obtain

$$\begin{aligned} \frac{d\widehat{PS}_3}{dv dw dz} &= \frac{s^2(-\varepsilon)}{2(4\pi)^4 \Gamma(2-2\varepsilon)} \left(\frac{4\pi}{s} \right)^{2\varepsilon} (1-v)^{-\varepsilon} (1-w)^{1-\varepsilon} v^{2-2\varepsilon} w^{-\varepsilon} \\ &\times 2 \cos \psi g(z)^{1-\varepsilon} \int \sin^{2-2\varepsilon} \theta_2 d\theta_2. \end{aligned} \quad (3.89)$$

Besides some obvious misprints, Eq. (3.89) is in agreement with Eq. (B42) in Appendix B of [97].

Since the phase space is proportional to ε and exhibits an additional factor $(1-w)$, we shall stress that there are no additional poles arising from contributions proportional to \hat{p}_d^2 . However, in combination with a $1/\varepsilon$ singularity from subsequent integrations, we get finite contributions to the polarized two-hadron photoproduction cross section. Thus, simply disregarding hat-momenta would yield wrong results.

Next, we turn to the actual phase space integration of the $2 \rightarrow 3$ matrix elements.

3.4.3 Phase Space Integration

The partonic cross sections $ab \rightarrow cde$ relevant for di-hadron photoproduction, differential in v , w , and z , are obtained by integrating the $2 \rightarrow 3$ matrix elements squared over the entire phase space of the unobserved parton e . As explained in detail for the LO case, one has to attach the flux factor and average or sum over the color and spin degrees of freedom, depending on whether one deals with initial state or final state partons. The unpolarized and polarized cross sections then take the form

$$\begin{aligned} \frac{d\hat{\sigma}_{ab \rightarrow cdX}^{real}}{dv dw dz} &= \frac{1}{2s} \frac{dPS_3}{dv dw dz} \overline{\sum} |\mathcal{M}_r|_{ab \rightarrow cde}^2, \\ \frac{d\Delta\hat{\sigma}_{ab \rightarrow cdX}^{real}}{dv dw dz} &= \frac{1}{2s} \frac{dPS_3}{dv dw dz} \overline{\sum} \Delta |\mathcal{M}_r|_{ab \rightarrow cde}^2, \end{aligned} \quad (3.90)$$

respectively. The [polarized] $2 \rightarrow 3$ matrix elements squared $[\Delta]|\mathcal{M}_r|_{ab \rightarrow cde}^2$ can be expressed in terms of the ten Mandelstam variables, defined in Eq. (3.47), and terms proportional to \hat{p}_d^2 .

In order to perform the integrations over the angle θ_2 in Eqs. (3.81) or (3.89), we have to make the dependence on θ_2 explicit in the $[\Delta]|\mathcal{M}_r|_{ab \rightarrow cde}^2$. To this end,

we use the parameterization of the momenta in Eqs. (3.72) and find that

$$\begin{aligned}
t_2 &= -\frac{sv}{2}(1 - \cos \psi \cos \theta_1 - \sin \psi \sin \theta_1 \cos \theta_2), \\
u_2 &= -\frac{s(1-vw)}{2}(1 - \cos \psi \cos \theta_1 + \sin \psi \sin \theta_1 \cos \theta_2), \\
t_3 &= -\frac{sv}{2}(1 + \cos \psi \cos \theta_1 + \sin \psi \sin \theta_1 \cos \theta_2), \\
u_3 &= -\frac{s(1-vw)}{2}(1 + \cos \psi \cos \theta_1 - \sin \psi \sin \theta_1 \cos \theta_2), \\
s_{12} &= \frac{s(1-v+vw)}{2}(1 - \cos \psi' \cos \theta_1 - \sin \psi' \sin \theta_1 \cos \theta_2), \\
s_{13} &= \frac{s(1-v+vw)}{2}(1 + \cos \psi' \cos \theta_1 + \sin \psi' \sin \theta_1 \cos \theta_2). \quad (3.91)
\end{aligned}$$

The other Mandelstam variables s , t , u , and s_{23} are harmless, since they do not have any dependence on the angle θ_2 . After having rewritten the matrix elements in this way, the integration over θ_2 needs to be done with special care, since poles in z and w may arise. They need a special treatment and require the introduction of plus-distributions. We give here a general description of how to integrate the different combinations of Mandelstam variables. For a detailed discussion we refer to Appendix B, where we collect the explicit formulas for the integration of all relevant combinations of Mandelstam variables appearing in the direct processes at NLO accuracy, listed in Eq. (3.49).

The first step is the decomposition of complex structures of Mandelstam variables into a set of calculable basic integrals. The problem is, that only combinations of Mandelstam variables can be integrated analytically, where at most two depend on θ_2 . We employ extensive partial fractioning, together with the relations among the ten Mandelstam variables given in Eqs. (3.48). To illustrate this procedure consider the term $1/(t_2 u_2 s_{13})$. As it stands, it cannot be integrated analytically. This combination can be rewritten as

$$\frac{1}{t_2 u_2 s_{13}} = \frac{1}{s} \left[\frac{1}{t_2 u_2} - \frac{1}{t_2 s_{13}} - \frac{1}{u_2 s_{13}} \right]. \quad (3.92)$$

Hence, a term with a too complicated dependence on θ_2 in the denominator has been turned into three simpler terms, all integrable. Making an extensive use of this procedure one ends up with a relatively small amount of master integrals, discussed in detail in Appendix B.

In the following we give a general outline of the calculation of these integrals. We first note, that any Mandelstam variable in Eq. (3.91) can be expressed as

$$X_i = X_{i0}(a_i + b_i \cos \theta_2). \quad (3.93)$$

The prefactor X_{i0} only depends on v and w . The a_i , b_i , and X_{i0} have no dependence on the integration angle θ_2 . The relevant combinations, covering all eventualities for direct photoproduction, are

$$X_i^k, X_i X_j, \frac{1}{X_i}, \frac{X_i^k}{X_j}, \frac{1}{X_i X_j}, \quad (3.94)$$

where k is an integer and takes at most the value $k = 3$. These combinations in turn are all expressible in terms of two master integrals. However, the explicit form of the coefficients a_i and b_i determines the final result: the singularity structure in terms of poles in $1/\varepsilon$ and $1/\varepsilon^2$ accompanied by Dirac δ -functions in w and z , and plus-distributions in w and z .

The most general and simplest integral, where the combinations of Mandelstam variables exhibit no explicit dependence on θ_2 , has the form

$$I_0 \equiv \int_0^\pi \sin^{-2\varepsilon} \theta_2 d\theta_2. \quad (3.95)$$

Using Eq. (3.80), we immediately find

$$I_0 = \sqrt{\pi} \frac{\Gamma(\frac{1}{2} - \varepsilon)}{\Gamma(1 - \varepsilon)} = \pi 2^{2\varepsilon} \frac{\Gamma(1 - 2\varepsilon)}{\Gamma^2(1 - \varepsilon)}. \quad (3.96)$$

The next simplest integral with just one θ_2 -depending Mandelstam variable in the denominator takes the form

$$I_1(X_i) \equiv X_{i0} \int_0^\pi \frac{\sin^{-2\varepsilon} \theta_2 d\theta_2}{X_i} = \int_0^\pi \frac{\sin^{-2\varepsilon} \theta_2 d\theta_2}{a_i + b_i \cos \theta_2}. \quad (3.97)$$

With the use of Ref. [95] we obtain

$$\begin{aligned} I_1(X_i) &= \sqrt{\pi} \frac{\Gamma(\frac{1}{2} - \varepsilon)}{\Gamma(1 - \varepsilon)} \frac{1}{a_i - b_i} {}_2F_1 \left[1, \frac{1}{2} - \varepsilon; 1 - 2\varepsilon; \frac{2b_i}{b_i - a_i} \right] \\ &= \frac{\pi}{\sqrt{a_i^2 - b_i^2}} \left[\frac{4a_i^2}{a_i^2 - b_i^2} \right]^\varepsilon \frac{\Gamma(1 - 2\varepsilon)}{\Gamma^2(1 - \varepsilon)} \\ &\times {}_2F_1 \left[\frac{1}{2} - \varepsilon, -\varepsilon; 1 - \varepsilon; \frac{b_i^2}{a_i^2} \right], \end{aligned} \quad (3.98)$$

with ${}_2F_1(a, b; c; z)$ being the hyper-geometric function. The explicit form of the integrals $I_1(X_i)$ and the types of singularities occurring in the calculation, depend on the prefactors a_i and b_i . All combinations of Mandelstams variables can in general be decomposed into these two integrals, as will be shown below. However, one has to take care, if singularities arise. A derivation of all formulas for the

combinations of Mandelstam variables, we encounter in the integration of the matrix elements, can be found in Appendix B.

If there is no dependence on the angle θ_2 in the denominator of the integrand, the integrals over θ_2 of all Mandelstam combinations can be written solely in terms of I_0

$$\begin{aligned}
X_i^0 &\rightarrow I_0, \\
X_i &\rightarrow X_{i0}a_i I_0, \\
X_i^2 &\rightarrow X_{i0}^2 \left[a_i^2 + \frac{b_i^2}{2(1-\varepsilon)} \right] I_0, \\
X_i X_j &\rightarrow X_{i0} X_{j0} \left[a_i a_j + \frac{b_i b_j}{2(1-\varepsilon)} \right] I_0, \\
X_i^3 &\rightarrow X_{i0}^3 \left[a_i^3 + \frac{3a_i b_i^2}{2(1-\varepsilon)} \right] I_0.
\end{aligned} \tag{3.99}$$

The other case is, when there is at least one Mandelstam variable in the denominator. As mentioned above, these Mandelstam combinations can be rewritten in terms of $I_1(X_i)$:

$$\begin{aligned}
\frac{1}{X_i} &\rightarrow \frac{1}{X_{i0}} I_1(X_i), \\
\frac{X_i}{X_j} &\rightarrow \frac{X_{i0}}{X_{j0}} \left[\frac{a_i b_j - a_j b_i}{b_j} I_1(X_j) + \pi \frac{b_i}{b_j} \right], \\
\frac{X_i^2}{X_j} &\rightarrow \frac{X_{i0}^2}{X_{j0}} \left\{ \left[\frac{a_i b_j - a_j b_i}{b_j} \right]^2 I_1(X_j) + \pi \left[\frac{2a_i b_i b_j - a_j b_i^2}{b_j^2} \right] \right\}, \\
\frac{X_i^3}{X_j} &\rightarrow \frac{X_{i0}^3}{X_{j0}} \left\{ \left[\frac{a_i b_j - a_j b_i}{b_j} \right]^3 I_1(X_j), \right. \\
&\quad \left. + \pi \left[\frac{6a_i b_i b_j (a_i b_j - b_i a_j) + b_i^3 (b_j^2 + 2a_j^2)}{2b_j^3} \right] \right\}, \\
\frac{1}{X_i X_j} &\rightarrow \frac{1}{X_{i0} X_{j0}} \frac{1}{a_j b_i - a_i b_j} \left[b_i I_1(X_i) - b_j I_1(X_j) \right].
\end{aligned} \tag{3.100}$$

The latter decomposition is not possible, if the term $(a_j b_i - a_i b_j)$ can be zero. For example, if the integrand is $1/(t_3 u_3)$, this term contains a factor $(1 + \cos \psi \cos \theta_1)$

and reaches zero for $w = 1$. This calls for yet another special treatment, and the explicit formulas are also given in Appendix B.

In the case of hat-momenta in the phase space integration the exponent of the sine-function in Eq. (3.97) is modified from (-2ε) to $(2 - 2\varepsilon)$, and we need to compute two additional integrals:

$$\begin{aligned} \int_0^\pi \frac{\sin^{2-2\varepsilon} \theta_2 d\theta_2}{a_i + b_i \cos \theta_2} &= \frac{\Gamma^2(\frac{3}{2} - \varepsilon)}{2^{-2+2\varepsilon} \Gamma(3 - 2\varepsilon)} \frac{1}{a_i} {}_2F_1\left(\frac{1}{2}, 1; 2 - \varepsilon; \frac{b_i^2}{a_i^2}\right), \\ \int_0^\pi \frac{\sin^{2-2\varepsilon} \theta_2 d\theta_2}{(a_i + b_i \cos \theta_2)^2} &= \frac{\Gamma^2(\frac{3}{2} - \varepsilon)}{2^{-2+2\varepsilon} \Gamma(3 - 2\varepsilon)} \frac{1}{a_i^{1-2\varepsilon}} \frac{1}{(a_i^2 - b_i^2)^{\varepsilon+1/2}} \\ &\quad \times {}_2F_1\left(1 - \varepsilon, \frac{1}{2} - \varepsilon; 2 - \varepsilon; \frac{b_i^2}{a_i^2}\right). \end{aligned} \quad (3.101)$$

The first integral vanishes in combination with the factor $(-\varepsilon)$ stemming from the phase space $d\widehat{PS}_3$, unlike the second integral, where the factor $1/(a_i^2 - b_i^2)^{\varepsilon+1/2}$ can yield terms proportional to $1/\varepsilon$. Here, we get non-zero contributions when combined with the factor $(-\varepsilon)$ from the phase space in Eq. (3.89).

As mentioned already, distributions in w and z occur in the calculation. For example, terms containing $(1 - w)^{-1-\varepsilon}$ develop a pole as $w \rightarrow 1$. This can be handled by the identity

$$\frac{1}{(1 - w)^{1+\varepsilon}} = -\frac{1}{\varepsilon} \delta(1 - w) + \frac{1}{(1 - w)_+} - \varepsilon \left[\frac{\ln(1 - w)}{1 - w} \right]_+ + \mathcal{O}(\varepsilon^2), \quad (3.102)$$

with $1/(1 - w)_+$ as the plus-distribution, defined via an arbitrary test function $f(w)$ by

$$\int_0^1 dw \frac{f(w)}{(1 - w)_+} \equiv \int_0^1 dw \frac{f(w) - f(1)}{1 - w}, \quad (3.103)$$

and similarly for $[\ln(1 - w)/(1 - w)]_+$. Equation (3.102) can be easily verified by integrating both sides with a test function according to Eq. (3.103). Furthermore, we get distributions in z . As $z > 1$ is possible, the plus-distribution must be generalized to any range of integration. We split it into the ranges $[0; 1]$ and $[1; z_{\max}]$. In addition to the “normal” plus-distribution, such as Eq. (3.103), this leads to an alternative definition via a test function $f(z)$

$$\int_1^{z_{\max}} dz \frac{f(z)}{(z - 1)_+} \equiv \int_1^{z_{\max}} dz \frac{f(z) - f(1)}{z - 1}. \quad (3.104)$$

Another modification has to be made, if the pole appears at $z = z_1 \equiv 1/(1 - v + vw)$ with $w \neq 1$ and hence $z_1 \neq 1$. In this case we make the following definitions

of plus-distributions

$$\begin{aligned} \int_0^{z_1} dz \frac{f(z)}{(z_1 - z)_+} &\equiv \int_0^{z_1} dz \frac{f(z_1) - f(z)}{z_1 - z}, \\ \int_{z_1}^{z_{\max}} dz \frac{f(z)}{(z - z_1)_+} &\equiv \int_{z_1}^{z_{\max}} dz \frac{f(z) - f(z_1)}{z - z_1}. \end{aligned} \quad (3.105)$$

The singularities appear in poles $1/\varepsilon$ and $1/\varepsilon^2$. For the explicit pole structure of all Mandelstam combinations, we refer to Appendix B.

3.5 Counter Terms, the Cancellation of Singularities, and Final Results

After renormalizing the virtual contributions stemming from vertex corrections and self-energies, they are free of any UV divergencies. In the next step, adding them to the real contributions with one additional particle in the final state at the partonic level, all infrared $1/\varepsilon$ singularities and coinciding IR and collinear $1/\varepsilon^2$ poles cancel for each process in the sum of all contributing diagrams [44, 45, 46]. The remaining collinear singularities, appearing as $1/\varepsilon$, are handled by the factorization procedure, as discussed in Sec. 2.3. They arise when the momentum p_i of an unobserved parton becomes parallel to any of the other parton momenta. After adding the appropriate counter terms for the collinear divergencies the sum of all contributions is free of any poles in ε and the limit $\varepsilon \rightarrow 0$ can safely be performed to obtain the final results.

In the real corrections, Eq. (3.45), the third, not observed parton, say parton e , can in principle become collinear to any leg of any other parton in the hard process. However, in the direct case gluons, of course, can not become collinear to the incoming photon, because there is no vertex including both photons and gluons.

We remove collinear singularities by factorizing them from the hard cross section at the partonic level to the soft functions like parton distribution and fragmentation functions, depending on whether the collinear poles stem from initial or final state parton legs. This subtraction is performed at a scale μ_f for initial state singularities and μ'_f for final state singularities and thus gives rise to “dressed” functions $[\Delta]f_i^{N,l}(x, \mu_f)$ and $D_i^H(z, \mu'_f)$. Together with the collinear singularities one has the possibility to shift also finite pieces from the hard to the soft parts. This is due to the freedom in choosing a factorization scheme. If no photon is involved in the splitting process, we use the $\overline{\text{MS}}$ scheme like for the renormalization procedure introduced in Sec. 2.2. In this scheme we subtract finite terms proportional to γ_E and $\ln 4\pi$ together with $1/\varepsilon$ poles, see, e.g.,

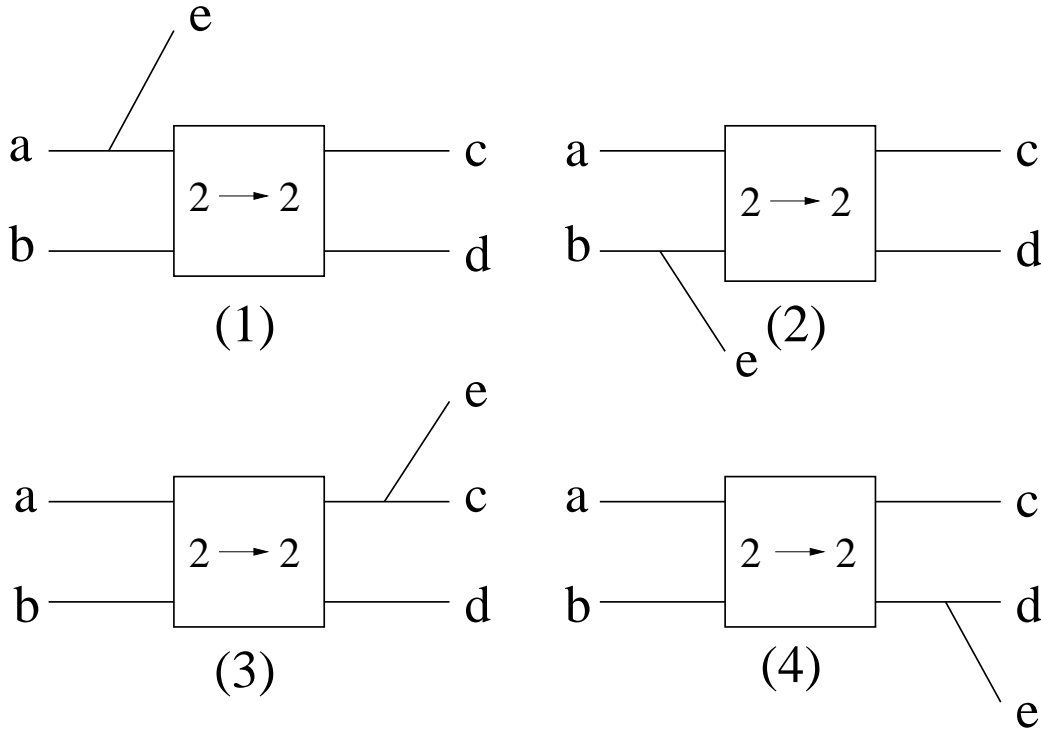


Figure 3.8: The four different possibilities for collinear singularities.

Eq. (2.42). In the literature, parton distribution and fragmentation functions are usually given in the $\overline{\text{MS}}$ scheme. However, care has to be taken in the case, if a photon is involved in the factorization process. Here, we slightly deviate from the $\overline{\text{MS}}$ scheme and use the so called DIS_γ scheme, discussed in Sec. 2.3, as photon distribution functions are often given in this scheme. For the transformation from $\overline{\text{MS}}$ to DIS_γ we refer to the end of this Section.

In principle, at NLO collinear emissions can occur from any external leg, initial and final state, of a $2 \rightarrow 2$ LO process. Although for the direct processes, considered in this work, collinear configurations on all four legs are not possible, we give here the most general expression, including all possibilities. Assuming that parton e is not observed and can become collinear to any other parton leg, we have four different possibilities, shown schematically in Fig. 3.8.

In practice, the factorization is performed by adding appropriate counter terms to every partonic cross section in order to remove the collinear poles. These counter terms always have the simple structure of a convolution of a n -dimensional LO $2 \rightarrow 2$ partonic cross section, with a divergent “transition function”, contain-

ing a four-dimensional LO splitting function. In the $\overline{\text{MS}}$ scheme we have

$$[\Delta]H_{ij}(x, Q^2) = \left(-\frac{1}{\varepsilon} + \gamma_E - \ln 4\pi \right) [\Delta]P_{ij}(x) \left(\frac{s}{\mu^2} \right)^\varepsilon + [\Delta]f_{ij}(z). \quad (3.106)$$

The $[\Delta]P_{ij}(z)$ denote the usual [polarized] four-dimensional LO one-loop splitting functions [54]:

$$\begin{aligned} \Delta P_{qg}(z) &= \frac{1}{2} [z^2 - (1-z)^2], \\ \Delta P_{gq}(z) &= C_F \left[\frac{1 - (1-z)^2}{z} \right], \\ \Delta P_{qq}(z) &= C_F \left[\frac{2}{(1-z)_+} - 1 - z + \frac{3}{2} \delta(1-z) \right], \\ \Delta P_{gg}(z) &= 2C_A \left[\frac{1}{(1-z)_+} - 2z + 1 \right] + \left[\frac{11}{6} C_A - \frac{N_f}{3} \right] \delta(1-z). \end{aligned} \quad (3.107)$$

The unpolarized counterparts can be found, e.g., in [31]. The functions $[\Delta]f_{ij}(z)$ in Eq. (3.106) reflect the freedom in choosing a factorization prescription. In the $\overline{\text{MS}}$ scheme these functions all vanish, except for the polarized qq -case. In the framework of the HVBM regularization procedure [43, 47] the definition of γ_5 results in helicity non-conservation at the quark-gluon vertex in n dimensions [63, 64, 98, 99, 100]. This gives rise to a deviation of the spin-dependent n -dimensional quark-to-quark splitting function in LO from the corresponding unpolarized counterpart

$$\Delta P_{qq}(z) - P_{qq}(z) = 4C_F \varepsilon (1-z). \quad (3.108)$$

If one demands helicity conservation the P_{qq} and ΔP_{qq} must coincide. As is well known, the literal $\overline{\text{MS}}$ factorization prescription would lead to inconsistencies in the renormalization of the axial current, and the cancellation of collinear singularities is not guaranteed beyond NLO [101]. We therefore slightly deviate from the normal $\overline{\text{MS}}$ prescription in the spin-dependent case and restore helicity conservation by choosing [63, 64, 100]

$$\Delta f_{qq}(z) = -4C_F(1-z). \quad (3.109)$$

All other $\Delta f_{ij}(z)$ are set to zero.

Depending on which leg undergoes the collinear splitting, the kinematics of the counter term deviates from the LO case, where $s + t + u = 0$. Taking this into account, the appropriate spin-dependent counter term cross section reads in the

four different cases as depicted in Fig. 3.8:

$$\begin{aligned}
\frac{1}{sv} \frac{d\Delta\hat{\sigma}_{ab\rightarrow cdX}^{fact}}{dv dw dz} = & -\frac{\alpha_s}{2\pi} \left[\frac{1}{sv} \Delta H_{ia}(w, \mu_f^2) \frac{d\Delta\hat{\sigma}_{ib\rightarrow cd}^{(0)}}{dv}(ws, v, \varepsilon) \delta(1-z) \right. \\
& + \frac{1}{s(1-vw)} \Delta H_{ib}\left(\frac{1-v}{1-vw}, \mu_f^2\right) \\
& \times \frac{d\Delta\hat{\sigma}_{ai\rightarrow cd}^{(0)}}{dv}\left(\frac{1-v}{1-vw}s, vw, \varepsilon\right) \delta(1-z) \\
& + \frac{1}{s(1-v+vw)} H_{ci}\left(1-v+vw, \mu_f'^2\right) \\
& \times \frac{d\Delta\hat{\sigma}_{ab\rightarrow id}^{(0)}}{dv}\left(s, \frac{vw}{1-v+vw}, \varepsilon\right) \delta(z_1-z) \\
& + \frac{1}{sv} H_{di}(z, \mu_f'^2) \frac{d\Delta\hat{\sigma}_{ab\rightarrow ci}^{(0)}}{dv}(s, v, \varepsilon) \\
& \left. \times \theta(1-z) \delta(1-w) \right], \tag{3.110}
\end{aligned}$$

with $z_1 = 1/(1-v+vw)$. The $d\Delta\hat{\sigma}_{jk\rightarrow lm}^{(0)}/dv$ are the LO polarized n -dimensional $2 \rightarrow 2$ cross sections for the process $jk \rightarrow lm$ and can be found in the HVBM scheme in [98]. As mentioned above, the cross sections are evaluated at some shifted kinematics, denoted by $(\zeta s, \xi)$, since the collinear parton j takes away a certain fraction of the available momentum. Note that the unpolarized $H_{ij}(x, \mu_f')$ contribute to the factorization of final state singularities, since we do not consider the production of polarized hadrons. Needless to say that an equation similar to Eq. (3.110) holds in the unpolarized case.

A special treatment is required, if photons are involved in the factorization process. The collinear singularities, stemming from $\gamma \rightarrow q\bar{q}$ splittings present in the direct part, are absorbed into the pointlike part of the photon densities and thus into the resolved piece of the photoproduction cross section. No cancellation of such divergencies is possible within the direct part alone, as the photon interacts here as a pointlike particle. Consequently, only the sum of direct and resolved contribution

$$d\Delta\sigma = d\Delta\sigma^{\text{dir}} + d\Delta\sigma^{\text{res}} \tag{3.111}$$

is a physically meaningful quantity and independent of conventions at NLO and beyond. In practice, the subtraction of collinear poles stemming from $\gamma \rightarrow q\bar{q}$ splitting is done in analogy to Eq. (3.106)

$$[\Delta]H_{q\gamma}(x, Q^2) = \left(-\frac{1}{\varepsilon} + \gamma_E - \ln 4\pi\right) [\Delta]P_{q\gamma}(x) \left(\frac{s}{\mu^2}\right)^\varepsilon + [\Delta]f_{q\gamma}(x), \tag{3.112}$$

where $[\Delta]f_{q\gamma}(z)$ again denotes the freedom in subtracting finite pieces together with the $1/\varepsilon$ poles. The [polarized] four-dimensional LO photon-to-quark splitting functions have the following form [70]

$$\begin{aligned} P_{q\gamma}(z) &= C_A \left[z^2 + (1-z)^2 \right], \\ \Delta P_{q\gamma}(z) &= C_A \left[z^2 - (1-z)^2 \right]. \end{aligned} \quad (3.113)$$

In the $\overline{\text{MS}}$ scheme the functions $[\Delta]f_{q\gamma}(x)$ vanish. However, it is common to express the [polarized] photon distribution functions $[\Delta]f_\gamma(x, \mu)$, defined in Eq. (2.56), in the DIS_γ scheme, which is related to the $\overline{\text{MS}}$ scheme via [52]

$$[\Delta]f_\gamma^{\overline{\text{MS}}}(x, \mu) = [\Delta]f_\gamma^{\text{DIS}_\gamma}(x, \mu) + \delta[\Delta]f_\gamma(x), \quad (3.114)$$

with $f = q, \bar{q}, g$, and where

$$\begin{aligned} \delta q_\gamma(x) &= \delta \bar{q}_\gamma(x) \\ &= -C_A e_q^2 \frac{\alpha_{em}}{2\pi} \left[(1-2x+2x^2) \ln \frac{1-x}{x} - 1 + 8x(1-x) \right], \\ \delta g_\gamma(x) &= 0, \\ \delta \Delta q_\gamma(x) &= \delta \Delta \bar{q}_\gamma(x) \\ &= -C_A e_q^2 \frac{\alpha_{em}}{2\pi} \left[(2x-1) \left(\ln \frac{1-x}{x} - 1 \right) + 2(1-x) \right], \\ \delta \Delta g_\gamma(x) &= 0. \end{aligned} \quad (3.115)$$

Alternatively, the hard partonic cross section in the $\overline{\text{MS}}$ scheme can be rewritten in the DIS_γ scheme by demanding that the sum of direct and resolved contributions to the partonic cross section remains invariant,

$$d\Delta\sigma = d\Delta\sigma^{\overline{\text{MS}}} = d\Delta\sigma^{\text{DIS}_\gamma}. \quad (3.116)$$

Hence, the appropriate scheme transformation is schematically given by

$$d\Delta\hat{\sigma}_{\gamma b \rightarrow cdX}^{\text{DIS}_\gamma} = d\Delta\hat{\sigma}_{\gamma b \rightarrow cdX}^{\overline{\text{MS}}} + \sum_a \delta\Delta a_\gamma \otimes d\Delta\hat{\sigma}_{ab \rightarrow cd}^{(0)}, \quad (3.117)$$

with $d\Delta\hat{\sigma}_{ab \rightarrow cd}^{(0)}$ the polarized LO partonic cross section for the process $ab \rightarrow cd$. Here, we disregard contributions $\delta\Delta f_\gamma \otimes d\Delta\hat{\sigma}^{(1)}$, which are formally of NNLO accuracy. Needless to say, Eqs. (3.116) and (3.117) hold also true for the unpolarized case by simply replacing the polarized quantities by their unpolarized counterparts.

Adding all contributions, virtual and real corrections, as well as the counter terms just discussed, we end up with the complete NLO cross section differential in v , w , and z

$$\frac{d\Delta\hat{\sigma}_{ab\rightarrow cdX}^{(1)}}{dv dw dz} = \frac{d\Delta\hat{\sigma}_{ab\rightarrow cd}^{virt}}{dv dw dz} + \frac{d\Delta\hat{\sigma}_{ab\rightarrow cdX}^{real}}{dv dw dz} + \frac{d\Delta\hat{\sigma}_{ab\rightarrow cdX}^{fact}}{dv dw dz}, \quad (3.118)$$

which is now finite in the limit $\varepsilon \rightarrow 0$, but depends explicitly on the renormalization scale μ_r and the factorization scales μ_f and μ'_f , which are omitted in Eq. (3.118).

We note that the polarized partonic cross section in Eq. (3.118) can be generically written in terms of all possible combinations of distributions

$$\begin{aligned} \frac{d\Delta\hat{\sigma}_{ab\rightarrow cdX}^{(1)}}{dv dw dz} &= \Delta K_1(v, w)\delta(1-z) + \Delta K_2(v, w)\delta(z_1-z) \\ &+ \Delta K_3(v, w)\frac{\theta(1-z)}{(1-z)_+} + \Delta K_4(v, w)\frac{\theta(z-1)}{(z-1)_+} \\ &+ \Delta K_5(v, w)\frac{\theta(z_1-z)}{(z_1-z)_+} + \Delta K_6(v, w)\frac{\theta(z-z_1)}{(z-z_1)_+} \\ &+ \Delta K_7(v, w)\left[\frac{\ln(1-z)}{1-z}\right]_+ + \Delta K_8(v, w, z). \end{aligned} \quad (3.119)$$

The functions $\Delta K_i(v, w, z)$, $i = 1, \dots, 8$ are regular in z and contain, in general, distributions in w . They can be decomposed further as

$$\begin{aligned} \Delta K_i(v, w) &= \Delta k_1(v)\delta(1-w) + \Delta k_2(v)\frac{1}{(1-w)_+} \\ &+ \Delta k_3(v)\left[\frac{\ln(1-w)}{1-w}\right]_+ + \Delta k_4(v, w). \end{aligned} \quad (3.120)$$

This decomposition holds also true for the unpolarized case. However, not all combinations give real plus-distributions in the end. For example, the product of $1/(z-1)_+$ and $1/(1-w)_+$ gives

$$\frac{\theta(z-1)}{(z-1)_+}\frac{1}{(1-w)_+} = \frac{\theta(z-1)}{(z-1)_+}\frac{1}{1-w}, \quad (3.121)$$

since in the region $z > 1$ the variable w is limited to $w < 1$ due to Eq. (3.78). In addition, in the case $w = 1$ the upper integration limit of z becomes $z_{\max} = 1$, and the distributions at $z = z_1$ coincide with the distributions at $z = 1$.

As already mentioned before, z has to be limited in the range $z > 0$ to avoid certain singular configurations as, e.g., two collinear hadrons. When comparing

with data, no experimental cuts on z can be made, since, strictly speaking, this is a partonic quantity. Here, we have to introduce the hadronic counterpart of z

$$z_H \equiv -\frac{\vec{P}_{T,1} \cdot \vec{P}_{T,2}}{P_{T,1}^2} = \frac{z_2}{z_1}, \quad (3.122)$$

with $P_{T,i}$ being the transverse momentum of hadron H_i , and z_i the momentum fraction of parton i carried by the produced hadron H_i . As a consequence, the lower bound on z is a function of the z_i . Analogously, the lower integration limit of the w integration also takes values $w_{\min} \neq 0$. Since the plus-distributions are defined so far in the interval 0 to 1, we need to generalize them to accommodate arbitrary lower limits. We define

$$\int_{z_{\min}}^1 dz f(z) [g(z)]_{z_{\min}} \equiv \int_{z_{\min}}^1 dz [f(z) - f(1)] g(z), \quad (3.123)$$

with a function $g(z)$ containing the singular structure in z . We can now re-express the usual plus-distributions by the new ones

$$\begin{aligned} \frac{1}{(1-z)_+} &= \frac{1}{(1-z)_{z_{\min}}} + \delta(1-z) \ln(1-z_{\min}) \\ \left(\frac{\ln(1-z)}{1-z} \right)_+ &= \left(\frac{\ln(1-z)}{1-z} \right)_{z_{\min}} + \frac{1}{2} \ln^2(1-z_{\min}) \delta(1-z). \end{aligned} \quad (3.124)$$

The same expressions of course hold true for the variable w , and for distributions including z_1 with simply replacing 1 by z_1 .

This completes the discussion of the analytic calculation of the cross section for the photoproduction of two hadrons.

4 Phenomenological Applications with the Analytic Approach

We now turn to the numerical studies of our results obtained in the previous Chapter, focusing on the relevance of NLO corrections and theoretical uncertainties due to the choice of scales. The main results presented here have been published in Ref. [23, 34]. In addition, we give the contributions of the individual subprocesses to the full cross section, and also show predictions for the double-spin asymmetry $A_{LL}^{H_1 H_2}$ defined in Eq. (3.6). This quantity turns out to be very sensitive to the chosen spin-dependent gluon distribution, and has more relevance for experiments than cross sections. This is, because in asymmetries acceptance corrections due to detector efficiencies and other experimental uncertainties partly cancel in the ratio of polarized and unpolarized cross sections. Thus, measuring $A_{LL}^{H_1 H_2}$ in experiment is a viable method for accessing the polarized parton distributions of the nucleon. We note, however, that a cross section measurement is essential to test the applicability of pQCD, which is not at all guaranteed at moderate c.m.s. energies.

This Chapter is dedicated to results obtained with the analytic approach, i.e., with the methods to perform the phase space integrations described in the previous Chapter. Here, we compute the NLO QCD corrections to the “direct” part of the spin-dependent cross section for two-hadron photoproduction,

$$l(P_l, \lambda_l) N(P_N, \lambda_N) \rightarrow l'(P_{l'}) H_1(P_1) H_2(P_2) X, \quad (4.1)$$

i.e., where the exchanged photon is at low virtuality and interacts as an elementary particle with one of the partons of the nucleon N . The P_i in (4.1) are the four-momenta of the observed leptons and hadrons, X contains all the additional hadronic activity not observed in experiment, and the λ_i denote the helicities of the interacting lepton l and nucleon N . Both hadrons H_1 and H_2 are required to be at high transverse momentum to ensure that the factorization procedure is applicable for this process.

We observe a hadron H_1 with transverse momentum $P_{T,1}$, which is scattered at an angle θ_1 relative to the incoming lepton beam. It is common to use its pseudorapidity

$$\eta_1 = -\ln \tan \left[\frac{\theta_1}{2} \right], \quad (4.2)$$

instead of the scattering angle θ_1 , as this quantity is additive under Lorentz boosts. For fixed-target experiments like COMPASS and HERMES, the transformation from the laboratory frame, where the nucleon is at rest, to the c.m.s. is given by

$$\eta_{cms} = \eta_{lab} - \frac{1}{2} \ln \left[\frac{2E_l}{M_N} \right], \quad (4.3)$$

with E_l being the energy of the incoming lepton beam and M_N the mass of the nucleon at rest. In the case of massless particles the pseudorapidity η_1 coincides with the rapidity y_1 defined by

$$y_1 = \frac{1}{2} \ln \left[\frac{E + p_z}{E - p_z} \right], \quad (4.4)$$

where E is the energy of the observed hadron and p_z the z -component of its momentum defined by the incident lepton beam direction.

Since we want to make use of the largely analytical methods developed in the previous Chapter, we are limited to observing the hadron H_2 in the hemisphere opposite to hadron H_1 . The transverse momentum vector $\vec{P}_{T,2}$ of hadron H_2 is constrained by z_H defined in Eq. (3.122), but otherwise unspecified kinematics, in particular the rapidity of the hadron H_2 is beyond our control. The fixed-target experiments like COMPASS and HERMES are not equipped with a 4π -detector covering all solid angles, but allow particle detection and identification only in a certain range of rapidity. Thus, hadron H_2 may end up outside the acceptance of the detector.

The factorized expression for the NLO spin-dependent cross section is a convolution of the non-perturbative parton distribution and fragmentation functions and the hard scattering of the partons and reads

$$\frac{d\Delta\sigma^{H_1H_2}}{dP_{T,1}dy_1dz_H} \equiv \frac{1}{2} \left[\frac{d\sigma_{++}^{H_1H_2}}{dP_{T,1}dy_1dz_H} - \frac{d\sigma_{+-}^{H_1H_2}}{dP_{T,1}dy_1dz_H} \right] \quad (4.5)$$

$$\begin{aligned} &= \frac{2P_{T,1}}{S} \sum_{i,j,k} \int_{1-V+VW}^1 \frac{dz_1}{z_1} \int_{\frac{VW}{z_1}}^{1-\frac{1-V}{z_1}} \frac{dv}{v(1-v)} \int_{\frac{VW}{vz_1}}^1 \frac{dw}{w} \\ &\times \int_{z_{\min}}^{z_{\max}} \frac{dz}{z} \Delta f_{\gamma}^l(x_l, \mu_f) \Delta f_i^N(x_N, \mu_f) \frac{\alpha_s(\mu_r) \alpha_{em}}{s} \\ &\times \left[\frac{d\Delta\hat{\sigma}_{\gamma \rightarrow jk}^{(0)}(v)}{dv} \delta(1-w) \delta(1-z) + \frac{\alpha_s(\mu_r)}{2\pi} \right. \\ &\times \left. \frac{d\Delta\hat{\sigma}_{\gamma \rightarrow jkX}^{(1)}}{dv dw dz}(s, v, w, \mu_f, \mu'_f, \mu_r, z) \right] \\ &\times D_j^{H_1}(z_1, \mu'_f) D_k^{H_2}(z_2, \mu'_f). \end{aligned} \quad (4.6)$$

The subscripts "++" and "+−" in (4.5) denote the settings of the helicities of the incoming lepton and nucleon. We have introduced the standard hadronic invariants

$$S = (P_l + P_N)^2, \quad T = (P_l - P_1)^2, \quad U = (P_N - P_1)^2, \quad (4.7)$$

$$V = 1 + \frac{T}{S}, \quad W = -\frac{U}{S + T}, \quad (4.8)$$

with four-momenta specified in Eq. (4.1). The partonic counterparts s , t , u , v , and w are defined in Eqs. (3.9) and (3.33).

Neglecting the masses of all particles one finds the following relations among the hadronic and partonic variables

$$s = x_l x_N S, \quad t = \frac{x_l}{z_1} T, \quad u = \frac{x_N}{z_1} U, \quad (4.9)$$

$$x_l = \frac{VW}{vwz_1}, \quad x_N = \frac{1 - V}{(1 - v)z_1}, \quad (4.10)$$

with x_l [x_N] being the fraction of the longitudinal momentum of the lepton [nucleon] taken by the quasi-real photon [parton i]. In addition, V and W in Eq. (4.8) are determined by the observed hadron H_1 and the lepton-nucleon c.m.s. energy squared S :

$$V = 1 - \frac{P_{T,1}}{\sqrt{S}} e^{-y_1}, \quad W = \frac{P_{T,1}^2}{SV(1 - V)}. \quad (4.11)$$

Note that the cross section on the left hand side of Eq. (4.6) is differential in the hadronic variable z_H , whereas the right side includes an integral over the partonic counterpart z , defined in Eq. (3.70). $z_{1,2}$ are the momentum share that the hadrons $H_{1,2}$ inherit from its parent partons j, k in the hadronization process. The latter is modeled by non-perturbative functions $D_{j,k}^{H_{1,2}}(z_{1,2}, \mu'_f)$ describing the collinear fragmentation of the partons j and k into the observed hadrons H_1 and H_2 , respectively. The $\Delta f_i^N(x_N, \mu_f)$ in Eq. (4.6) are the spin-dependent parton distribution functions, defined in Sec. 2.3 via Eq. (2.52).

As we only focus on the direct photon case in this Chapter, $\Delta f_\gamma^l(x_l, \mu_f)$ in Eq. (4.6) coincides with the spin-dependent Weizsäcker-Williams equivalent photon spectrum, see Eq. (2.57). It describes the collinear emission of a photon with low virtuality Q , less than some upper limit Q_{\max} determined by the experimental conditions. The non-logarithmic pieces in Eq. (2.57) result in a small but non-negligible contribution in case of muons.

The sum in Eq. (4.6) runs over all possible partonic channels $\gamma i \rightarrow jkX$, with i , j , and k being either an (anti)quark or a gluon. The $d\Delta\hat{\sigma}_{\gamma i \rightarrow jk}^{(0)}$ and $d\Delta\hat{\sigma}_{\gamma i \rightarrow jkX}^{(1)}$ denote the associated LO and NLO longitudinally polarized partonic hard-scattering

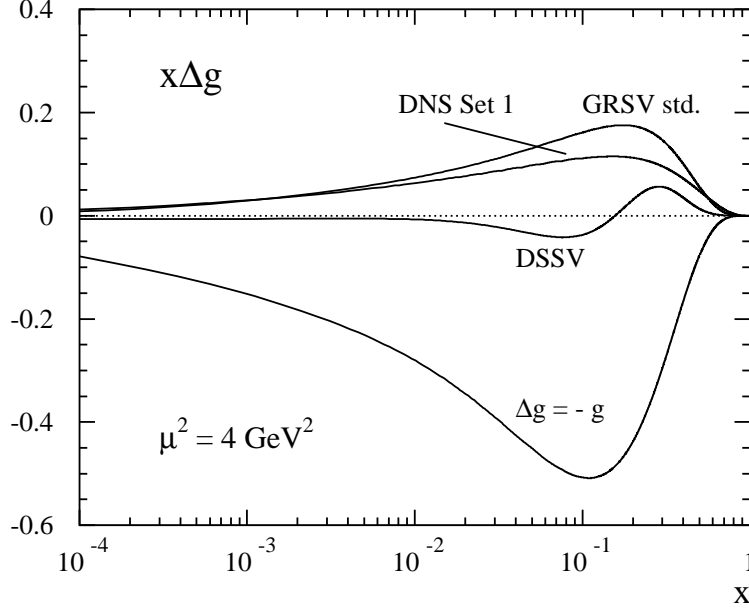


Figure 4.1: The polarized gluon distribution function $x\Delta g(x, \mu)$ as a function of x for different sets of parameterizations: GRSV std. [17], DNS Set 1 [62], DSSV [24], and an extreme set assuming $\Delta g = -g$ at the input scale of GRSV.

cross sections, respectively, given in Eqs. (3.37) and (3.118). They are defined in complete analogy to Eq. (4.5) and have been stripped of trivial factors involving the electromagnetic coupling α_{em} and the strong coupling $\alpha_s(\mu_r)$ evaluated at the renormalization scale μ_r . As indicated in Eq. (4.6) and discussed before, starting from the NLO level, the subprocess cross sections will explicitly depend on μ_r , as well as on the scales μ_f and μ'_f of the parton distribution and fragmentation functions owing to the factorization of initial and final state collinear singularities. Corresponding expressions for spin-averaged cross sections are straightforwardly obtained by replacing all polarized quantities by their unpolarized counterparts.

At LO the contributing subprocesses are the QCD Compton and photon-gluon fusion (PGF) processes, see Eqs. (3.14) and (3.15). At NLO the same $2 \rightarrow 2$ reactions have to be considered, now including virtual corrections. Additionally, processes with three partons in the final state contribute. They are listed for the direct case in Eq. (3.49). Since only two of the three final state partons fragment into the observed hadrons, it is indispensable to include all combinatorical possibilities by taking into account that any of the three partons can be the unobserved one.

In the computation of the LO and NLO unpolarized cross section we use the LO

and NLO CTEQ6 parton densities [56] and strong coupling α_s , respectively. In the polarized case we use the sets of DNS helicity dependent parton densities [62], the usual GRSV sets [17], as well as a new set by DSSV [24], described in detail in Sec. 2.3. This new set gives a rather small spin-dependent gluon distribution even when compared to fits with a moderate gluon polarization like DNS and GRSV. A small gluon polarization, either positive or negative, is indicated by all presently available data sensitive to $\Delta g(x, \mu_f)$ [20, 21, 28, 29]. We note that for a set with a positive gluon polarization, like the “standard” set of GRSV [17], and the sets of DNS [62], one encounters strong cancellations between the contributions from PGF and the QCD Compton process leading to sign changes in the polarized cross section. This makes it awkward to display the ratios of NLO to LO results we are interested in here. Hence we resort to the new set by DSSV, where the helicity-dependent gluon distribution is smaller and no sign changes appear for the NLO cross sections. Figure 4.1 shows the used spin-dependent gluon distributions as a function of the momentum fraction x of the proton taken by the gluon at a scale $\mu^2 = 4 \text{ GeV}^2$. Also shown is an extreme set from the GRSV analysis assuming a large and negative $\Delta g(x, \mu_f)$, now disfavored by data.

To model the hadronization of partons j and k into the observed hadrons H_1 and H_2 , we use the novel set of fragmentation functions of DSS [73]. This new set is based on a first global QCD analysis of inclusive hadron spectra in electron-positron annihilation, DIS multiplicities, and hadron-hadron scattering and known to describe hadronization fairly well also in the energy range relevant here [73]. Since COMPASS and HERMES do not identify different hadron species and measures only the sum of charged hadrons [20, 21], we use the corresponding LO and NLO sets of DSS [73] for all our calculations. We note that our studies for COMPASS kinematics have already been published [23, 34]. However, all results based on the recent DSSV global analysis are new and have not been shown before.

4.1 Results for COMPASS Kinematics

For our numerical studies in this Section we choose the kinematical setup of the COMPASS experiment [102], which scatters a beam of polarized muons with an energy of $E_\mu = 160 \text{ GeV}$ off deuteron in a polarized ^6LiD solid-state target, corresponding to a lepton-nucleon c.m.s. energy of $\sqrt{S} \simeq 18 \text{ GeV}$.

The results we show will be differential in the transverse momentum $P_{T,1}$ of hadron H_1 and integrated over the angular acceptance of the COMPASS experiment, i.e., covering scattering angles θ_1 of less than 180 mrad in the laboratory frame. Using Eqs. (4.2)-(4.4), this straightforwardly translates into a lower bound on the c.m.s. rapidity y_1 for hadron H_1 . Kinematics dictates the upper bound of

y_1 , depending on the transverse momentum of the hadron

$$y_1^{\max} = \cosh^{-1} \frac{\sqrt{S}}{2P_{T,1}}. \quad (4.12)$$

Recall that we cannot control the rapidity of hadron H_2 in our analytical calculation, which in turn implies that it may end up outside the acceptance of COMPASS. The range of the transverse momentum vector $\vec{P}_{T,2}$ of H_2 is restricted by demanding $z_H > 0.4$, with z_H as defined in Eq. (3.122). The momentum distribution of the quasi-real photons radiated off the muons is described by the Weizsäcker-Williams equivalent photon spectrum given in Eq. (2.57), with $m_l = m_\mu$ and $Q_{\max}^2 = 0.5 \text{ GeV}^2$. The momentum fraction x_l of the photon is restricted to be in the range $0.1 \leq x_l \leq 0.9$.

Figure 4.2 shows our results for the $P_{T,1}$ -differential cross section for the polarized and unpolarized photoproduction of a pair of charged hadrons at LO and NLO accuracy at COMPASS. We have set all renormalization and factorization scales in Eq. (4.6) equal to twice the transverse momentum of hadron H_1 . The sum of the transverse momenta of both hadrons might be a better motivated choice, but we do not have control on $P_{T,2}$ within the analytical calculation. The so-called “ K -factor”, defined as the ratio of NLO to LO unpolarized (polarized) cross sections

$$K \equiv \frac{d(\Delta)\sigma^{\text{NLO}}}{d(\Delta)\sigma^{\text{LO}}}, \quad (4.13)$$

is depicted in the lower panel of Fig. 4.2. The computed QCD corrections are such that the NLO results are below the LO estimates in the entire range of $P_{T,1}$ shown in Fig. 4.2. They appear to be more sizable in case of the polarized cross section. The observed difference of the unpolarized and polarized K -factors clearly indicates that NLO corrections are relevant also for studies of double-spin asymmetries, $A_{LL}^{H_1 H_2}$, see Eq. (3.6), as they do not cancel in the ratio. The contrary is often assumed in analyses of spin asymmetries.

We wish to make two remarks about the results shown in Fig. 4.2. Firstly, finding K -factors smaller than 1 is not a result of the NLO corrections to the hard-scattering partonic cross sections, but stems mostly from the difference between the LO and NLO parton distribution and fragmentation functions, in particular the latter. The LO and NLO sets of DSS show pronounced differences, mainly because the LO fragmentation functions try to make up for the often large NLO corrections in some of the fitted cross sections, see [73] for details, which are missing in a consistent LO analysis. The effect of the fragmentation functions is illustrated in Fig. 4.2 by the curves labeled “LO”. They refer to a calculation using LO matrix elements but NLO parton densities and fragmentation functions. This clearly demonstrates the inadequacy of LO results. At best they can serve as a rough estimate, but they are insufficient for any quantitative analysis. Very

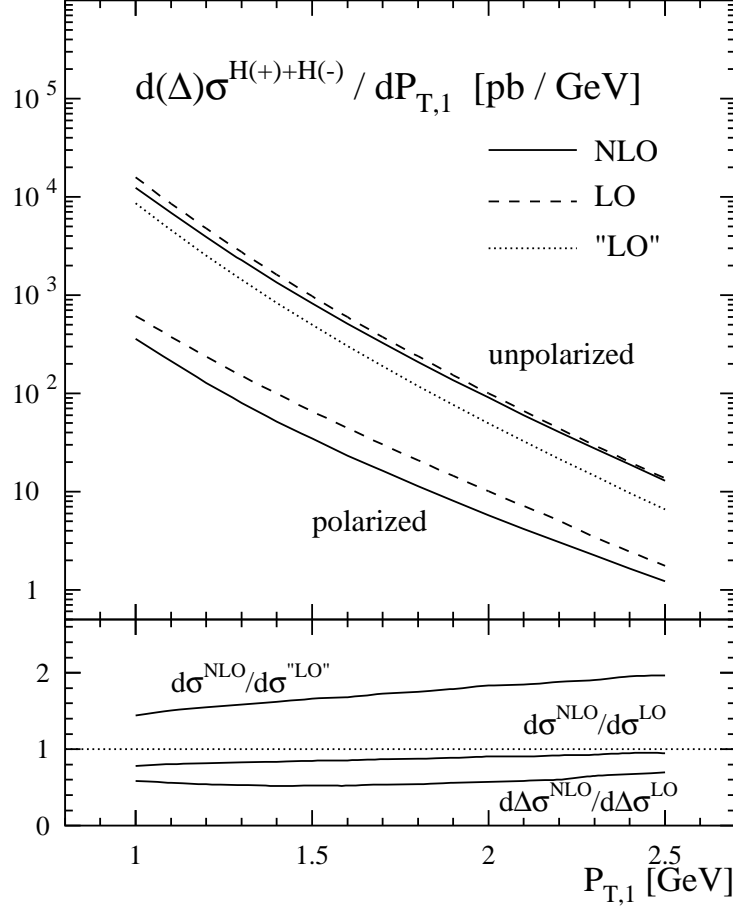


Figure 4.2: Unpolarized and polarized photoproduction cross section for a pair of charged hadrons, $\mu d \rightarrow (H_1^+ + H_1^-)(H_2^+ + H_2^-)X$, at LO (dashed) and NLO (solid) accuracy using COMPASS kinematics. The lower panel shows the ratios of NLO to LO cross sections (K-factor). The curve labeled “LO” refers to a LO calculation using NLO parton densities and fragmentation functions (see text).

similar observations can be made in the polarized case. Here, a “LO”-type calculation leads to K -factors ranging from 1.1 to 1.8. This is not shown in Fig. 4.2 for clarity.

Secondly, we note that the details and size of the NLO corrections in the polarized case depend significantly on the still largely unknown gluon polarization. As already mentioned, there can be strong cancellations between different subprocesses, leading to zeros in the polarized cross section. In their vicinity large

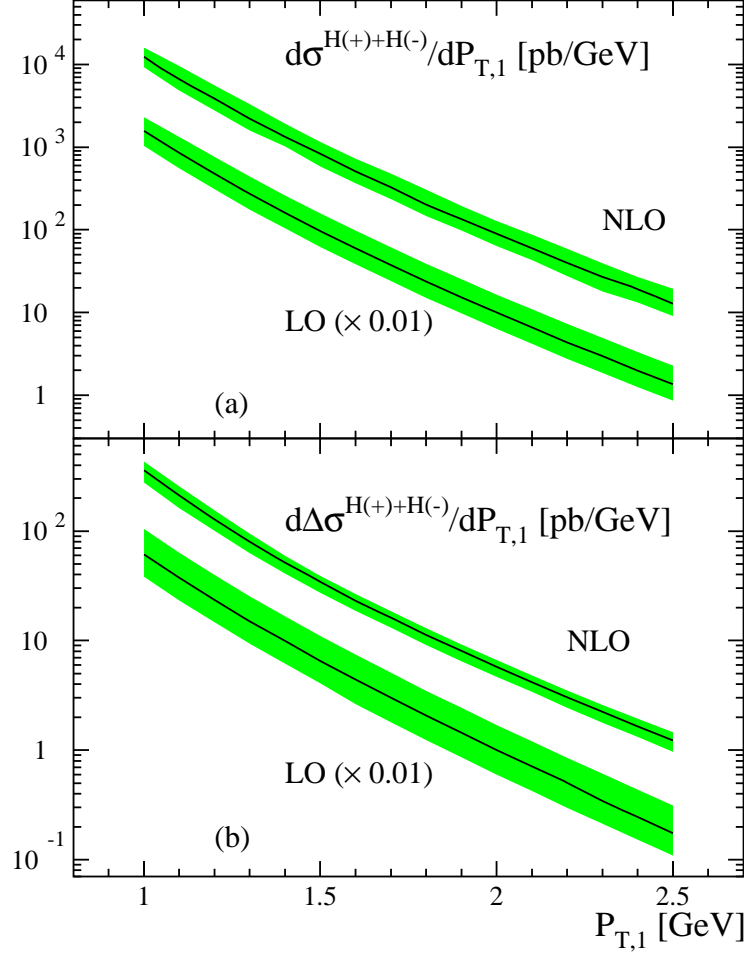


Figure 4.3: Scale dependence of the LO and NLO unpolarized (a) and polarized (b) cross sections for $\mu d \rightarrow (H_1^+ + H_1^-)(H_2^+ + H_2^-)X$ shown in Fig. 4.2. All scales are varied simultaneously in the range $\sqrt{2}P_{T,1} \leq \mu_r = \mu_f = \mu'_f \leq 2\sqrt{2}P_{T,1}$. Solid lines correspond to the choice where all scales are set to $2P_{T,1}$. All LO computations have been rescaled by a factor 0.01 to better distinguish them from the NLO results.

NLO corrections are in general inevitable.

As an estimate for the sensitivity of the computed cross sections to the actual choice of scales μ_f , μ'_f , and μ_r in Eq. (4.6), we vary them simultaneously in the range $\sqrt{2}P_{T,1} \leq \mu_r = \mu_f = \mu'_f \leq 2\sqrt{2}P_{T,1}$. We note that in principle all scales can be varied independently. The shaded bands in Figs. 4.3 (a) and (b)

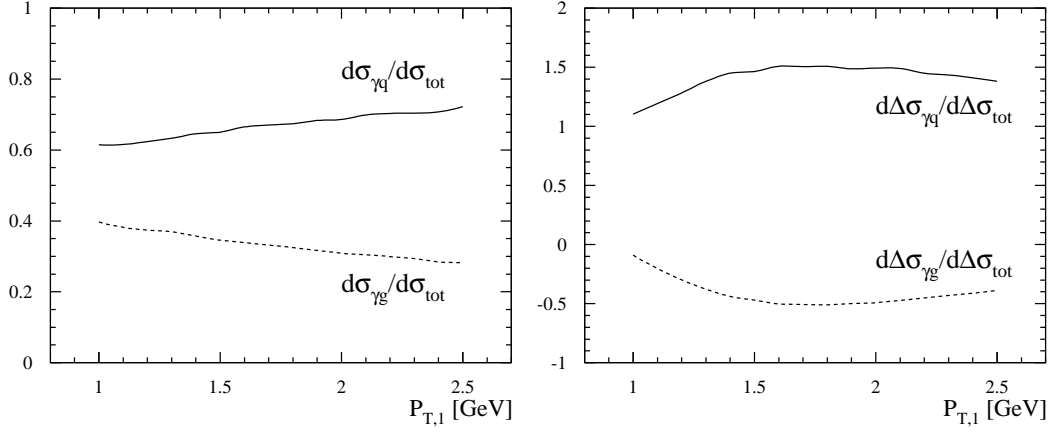


Figure 4.4: Relative contributions of the partonic channels $\gamma q \rightarrow cdX$ and $\gamma g \rightarrow cdX$, summed over all final states c, d , to the full unpolarized and polarized cross section at COMPASS.

indicate the resulting residual scale uncertainty of the unpolarized and polarized photoproduction cross sections, respectively. We find that the NLO results show somewhat reduced theoretical ambiguities, in particular, for the polarized cross section. However, similar remarks as above apply also here. Scale ambiguities in the polarized case depend on the details of the helicity-dependent parton densities and on possible cancellations among different subprocesses. One also has to keep in mind that the results only include the direct photon contribution to the photoproduction cross section. Predictions including the resolved contributions are addressed to Chapter 6, where we apply an alternative approach of a numerical phase space integration using the two cut-off phase space slicing method. Additionally, we shall stress here that constraining the transverse momentum $P_{T,2}$ of hadron H_2 by another value as $z_H^{\min} = 0.4$ does not lead to a reduction of scale dependence, but only gives a shift in the unpolarized and polarized cross sections. Going to smaller values for z_H^{\min} increases the cross sections, whereas a larger lower bound results in a reduction of the cross sections.

Next, we analyze the relevance of the different subprocesses, namely the partonic contributions $\gamma q \rightarrow cdX$ and the $\gamma g \rightarrow cdX$, where we sum over all final states c and d . Figure 4.4 shows the fractions of the different subprocesses to the full cross section, both the unpolarized (left panel) and polarized (right panel) case. Again, we constrain hadron H_2 by demanding $z_H > 0.4$ and set all scales equal to twice the transverse momentum of hadron H_1 . In the unpolarized case the γq -channel dominates, contributing between 60 and 80% to the direct pho-

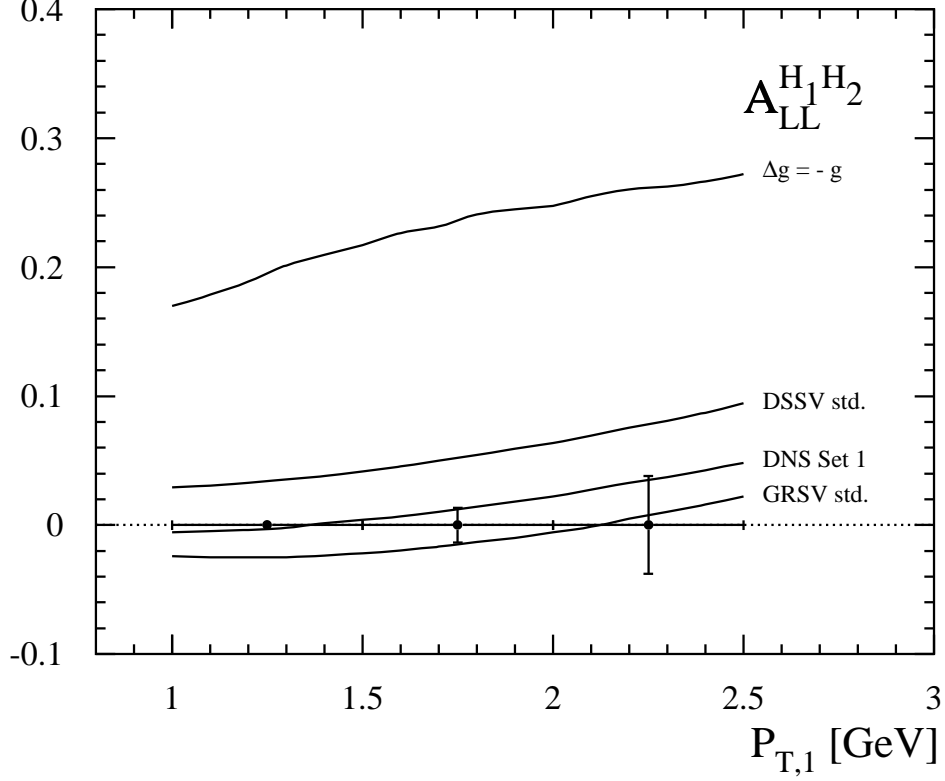


Figure 4.5: Double-spin asymmetry $A_{LL}^{H_1 H_2}$ at NLO accuracy for the direct part of di-hadron photoproduction at COMPASS for different sets of parton distributions. The error bars indicate the estimated statistical uncertainty for the COMPASS experiment at an integrated luminosity of 1 fb^{-1} .

toproduction cross section. For the corresponding studies in the polarized case we again employ the new set of polarized parton distribution functions by DSSV. For this particular set, the γq -channel dominates the full polarized cross section, and the PGF contributions enter with the opposite sign. This, of course, has to be taken with a pinch of salt due to the special choice of spin-dependent parton distributions. Using, for example, the sets of DNS or the standard GRSV set would lead to even larger cancellations between the two partonic channels and even to sign changes, making it difficult to display the results in a proper way. However, it tells us that the polarized photoproduction of hadron pairs is very sensitive to the used gluon scenario and in principle would allow for an extraction of $\Delta g(x, \mu)$. Figure 4.4 also shows that due to the huge cancellations of the γq - and γg -channels, the resolved contributions might be of relevance as well. Thus,

neglecting them can perhaps lead to misleading results for $\Delta g(z, \mu)$.

We now turn to the double-spin asymmetry $A_{LL}^{H_1 H_2}$ for the deuteron target used at COMPASS, as defined in Eq. (3.6), and depicted in Fig. 4.5 for different sets of polarized parton distributions. In our numerical studies we use Set 1 of DNS (obtained with Kretzer fragmentation functions) [73], the standard GRSV set [17], a maximal negative gluon polarization labeled as $\Delta g = -g$, as well as the new set by DSSV [24]. The respective gluon distributions have been shown in Fig. 4.1. Again, all scales are set equal, $\mu_r = \mu_f = \mu'_f = 2P_{T,1}$. Over the entire p_T -range the asymmetry obtained with the maximal negative gluon scenario exceeds all other results shown in Fig. 4.5, following the hierarchy: the more “negative” the $\Delta g(x, \mu)$, the more positive the double-spin asymmetry $A_{LL}^{H_1 H_2}$. This behavior can be traced back to the γg -channel, which gives large positive contributions to $d\Delta\sigma$ for negative $\Delta g(x, \mu)$, as the double-spin asymmetry at the partonic level is negative for the PGF process.

Figure 4.5 also shows the estimated statistical error for such a measurement as estimated by

$$\delta A_{LL}^{H_1 H_2} \simeq \frac{1}{\mathcal{P}_b \mathcal{P}_d \mathcal{F}_d \sqrt{\sigma_{bin} \mathcal{L}}}, \quad (4.14)$$

with $\mathcal{P}_b = 0.76$ being the beam polarization and $\mathcal{P}_d = 0.5$ the polarization of the deuteron target. The ^6LiD solid-state target has a dilution factor of $\mathcal{F}_d = 0.5$ [102], and σ_{bin} denotes the unpolarized cross section integrated over the $P_{T,1}$ -bin considered. We assume an integrated luminosity of $\mathcal{L} = 1 \text{ fb}^{-1}$. The error bars indicate that, in principle, one can distinguish between a small $\Delta g(x, \mu)$, and the extreme scenario of a maximal negative $\Delta g(x, \mu)$, but a precise determination seems to be possible only in the low $P_{T,1}$ -range, as the unpolarized cross section is larger and thus statistics is better in this region. COMPASS obtained a P_T -averaged double-spin asymmetry for photoproduction of hadron pairs of $A_{LL}^{H_1 H_2} \simeq 0.002 \pm 0.019(\text{stat.}) \pm 0.003(\text{syst.})$ [20], which is in agreement with our predictions for moderate sets of $\Delta g(x, \mu)$.

However, there are a few caveats in relating the measured $A_{LL}^{H_1 H_2}$ with a value for $\Delta g(x, \mu)$, which need to be addressed: First, one has to demonstrate the applicability of pQCD methods. For this purpose, an important “benchmark” would be the comparison of the relevant unpolarized cross sections with theoretical expectations, which are, e.g., given in Fig. 4.3. Unfortunately, such a kind of information is still lacking from COMPASS for the time being. Measuring the unpolarized cross section is essential, before making use of double-spin asymmetries in a reliable way. Let us stress that a possible discrepancy between experiment and theory at moderate c.m.s. energies would not necessarily imply that standard pQCD methods are beyond remedy. It would only call for further improvement by resumming large terms in the perturbative series, for instance threshold logarithms, to all orders in the strong coupling α_s . This is known to lead often to a

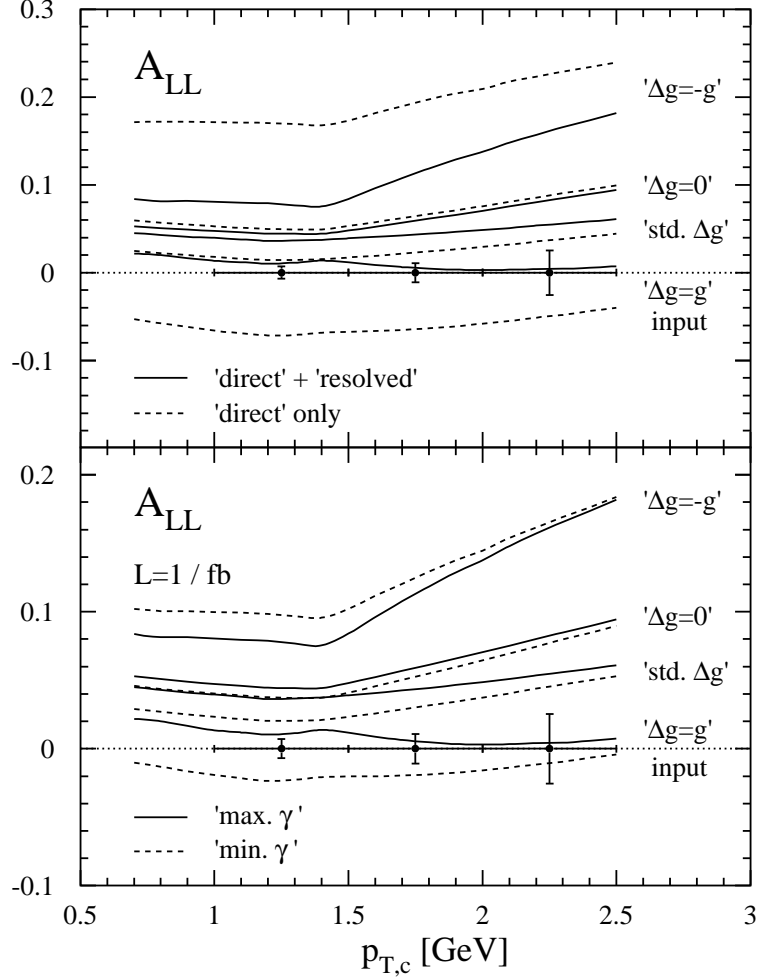


Figure 4.6: Double-spin asymmetry $A_{LL}^{H_1 H_2}$ as a function of $P_{T,1} = p_{T,c}$ at LO accuracy for different gluon polarizations. The upper panel shows the spin asymmetry with (solid lines) and without (dashed lines) including the resolved contribution. In the lower panel the dependence of $A_{LL}^{H_1 H_2}$ on the two extreme photon scenarios, “maximal” (solid lines) and “minimal” saturation (dashed lines), see Fig. 2.5, is shown. The “error bars” indicate the estimated statistical accuracy for such a measurement at COMPASS according to Eq. (4.14). The curve labeled ‘std. Δg ’ refers to the standard GRSV set, ‘ $\Delta g = g$ ’ [‘ $\Delta g = 0$ ’] corresponds to a maximal [vanishing] gluon polarization at the GRSV input scale. The Figure is taken from [23].

much improved agreement between data and pQCD calculations.

Second, we shall stress here that Fig. 4.5 only includes the direct part to the photoproduction cross section. The resolved part can become important, as it has been shown in our LO study [23]. The upper panel of Fig. 4.6 shows a comparison at LO accuracy of $A_{LL}^{H_1H_2}$ for the sum of direct and resolved contributions with $A_{LL}^{H_1H_2}$ computed for the direct part alone. Here, one can infer that, irrespective of the chosen Δg , the resolved part is non-negligible. It leads to a significant shift in the absolute value of the spin asymmetry, and neglecting it would clearly lead to wrong conclusions about Δg . Furthermore, in our analytic NLO studies we encounter hadrons which might end up outside the COMPASS detector acceptance, as explained above. We will address this issue and the importance of the resolved contributions in Chapter 5 and 6.

The studies in this Section are addressed to a deuteron target. Needless to say, this can also be done for a proton target, which has been used in the last run of the COMPASS experiment.

4.2 Results for HERMES Kinematics

In the recently completed HERMES experiment at DESY longitudinally polarized electrons and positrons with a beam energy of $E_e \simeq 27.5$ GeV were scattered off both a polarized deuterium and a polarized hydrogen gas target. The available c.m.s. energy of about $\sqrt{S} \simeq 7.5$ GeV is lower than at COMPASS, which even further limits the range of accessible transverse momenta. On average, the lepton beam polarization is $\mathcal{P}_e \simeq 0.53$. For the polarization of the gas target we take $\mathcal{P}_d \approx \mathcal{P}_p \simeq 0.85$, and, contrary to a solid-state target, there is no dilution from unpolarized target material, i.e., $\mathcal{F}_p = \mathcal{F}_d = 1$.

Here, we concentrate on phenomenological studies for a polarized deuterium target, which is the data sample with the highest statistics in the HERMES spin physics program. We demand hadron H_1 to be in the HERMES angular acceptance of $40 \text{ mrad} \leq \theta_1 \leq 220 \text{ mrad}$ and plot the results differential in its transverse momentum $P_{T,1}$. Again, hadron H_2 is constrained via the lower bound $z_H^{\min} = 0.4$, and no cut on its rapidity is made, implying that it may end up outside the HERMES detector acceptance. We choose a maximal photon virtuality of $Q_{\max}^2 = 0.1 \text{ GeV}^2$ in the Weizsäcker-Williams equivalent photon spectrum in Eq. (2.57) and restrict the momentum fraction x_l of the lepton taken by the quasi-real photon to the range $0.2 \leq x_l \leq 0.9$. The fractions of the parent parton's momenta carried by the produced hadrons are $z_{1,2} \geq 0.1$. Again, all scales in Eq. (4.6) are set equal to $\mu_r = \mu_f = \mu'_f = 2P_{T,1}$ unless stated otherwise, as we do not have control of $P_{T,2}$ within the formalism used here.

The upper panel of Fig. 4.7 shows the $P_{T,1}$ -differential unpolarized and polarized

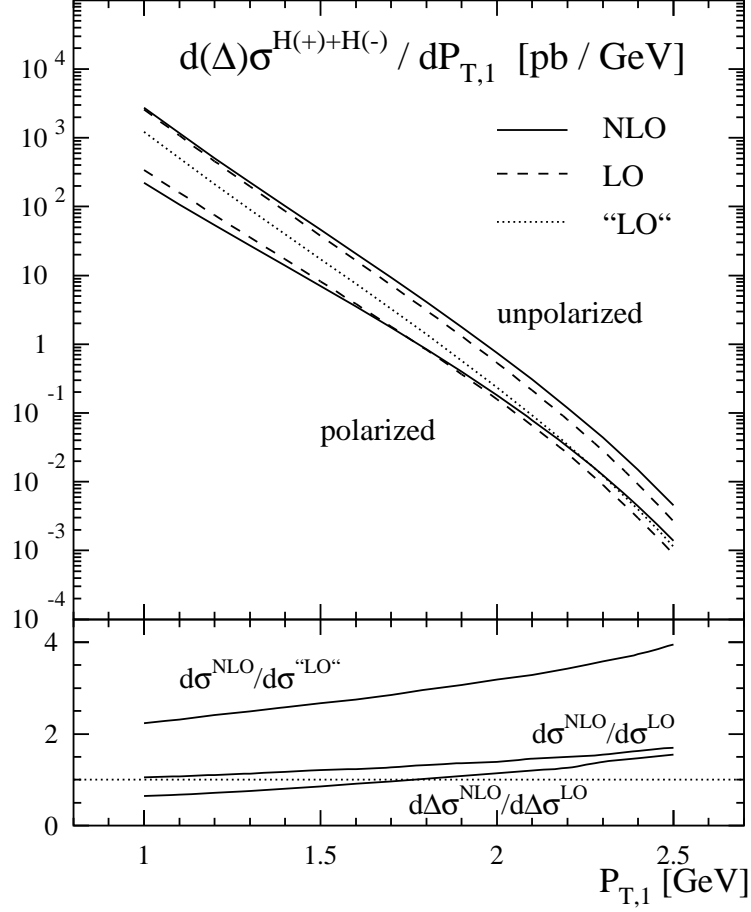


Figure 4.7: LO (dashed line) and NLO (solid line) unpolarized and polarized photoproduction cross section for a pair of charged hadrons, $ed \rightarrow (H_1^+ + H_1^-)(H_2^+ + H_2^-)X$ for HERMES kinematics. The K -factor is depicted in the lower panel. The “LO” curve refers to a LO-type calculation with NLO parton distributions and NLO fragmentation functions.

cross sections for HERMES kinematics at LO and NLO accuracy. The unpolarized and polarized K -factors, defined in Eq. (4.13), are depicted in the lower panel. As in Fig. 4.2, the curve labeled “LO” refers to a calculation using LO partonic cross sections and NLO parton distribution functions and NLO fragmentation functions.

Again, K -factors close to 1 are not a feature of the calculated NLO corrections, but stem from the sizable difference between LO and NLO parton distribution functions and fragmentation functions, as can be inferred from the curve labeled

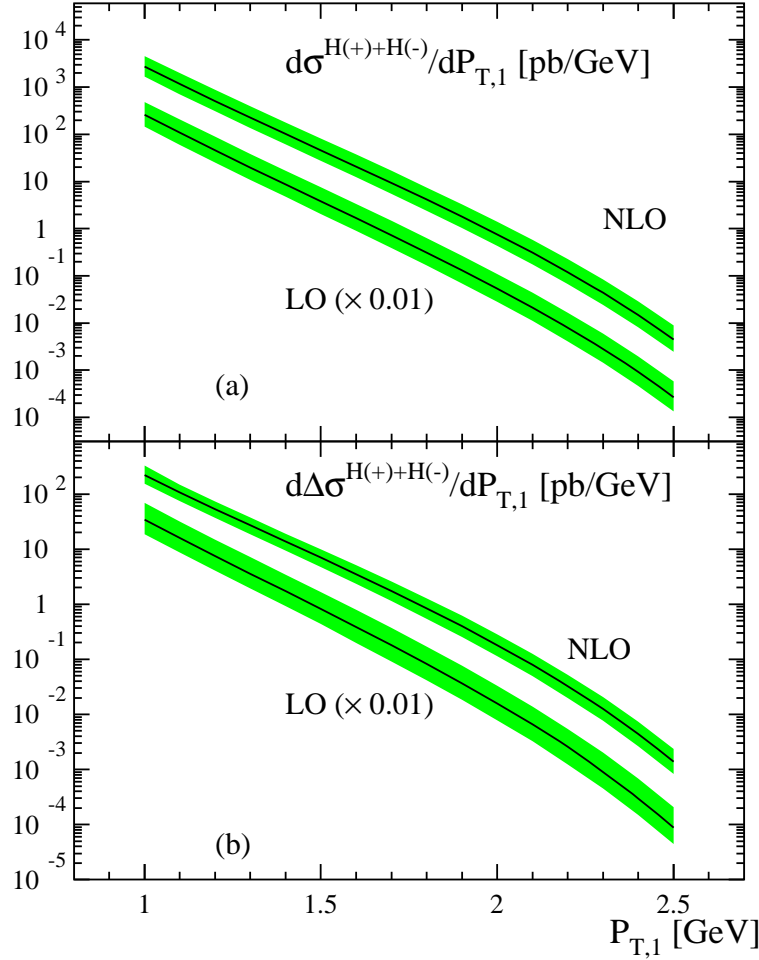


Figure 4.8: Scale dependence of the unpolarized and polarized di-hadron photoproduction cross section at HERMES kinematics. All scales are varied in the range $\sqrt{2}P_{T,1} \leq \mu_r = \mu_f = \mu'_f \leq 2\sqrt{2}P_{T,1}$.

“LO”. The effect is even more dramatic than before for COMPASS, see Fig 4.2, and the K -factor increases significantly in the whole $P_{T,1}$ -range considered. The calculation for the polarized case shows a similar pattern, but is not depicted in Fig. 4.7 for clarity. Again, for the polarized parton densities we have used the new DSSV set. As before, using other sets like GRSV “standard” or DNS leads to significant cancellations of the two partonic channels $\gamma q \rightarrow cdX$ and $\gamma g \rightarrow cdX$.

Next, to get a feeling for the theoretical error, which we make in the calculation due to the truncation of the perturbative series at a fixed order in the strong

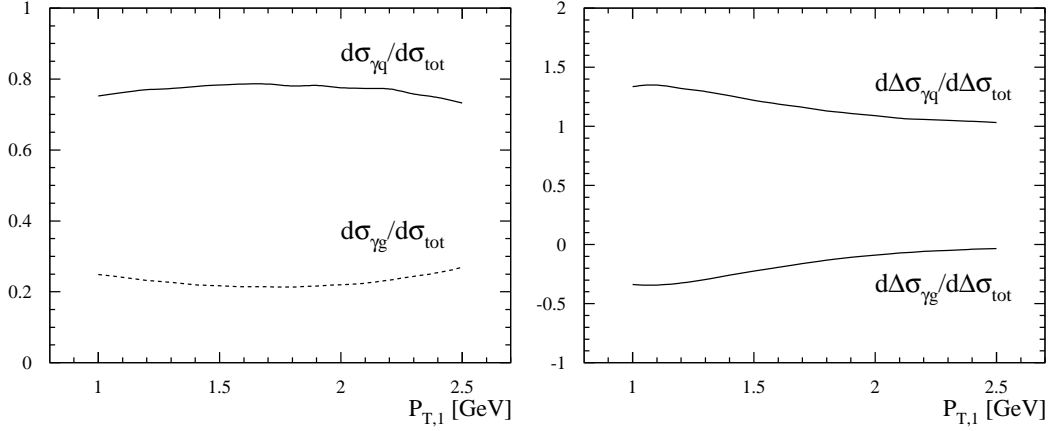


Figure 4.9: As in Fig. 4.4, but now for HERMES kinematics.

coupling constant α_s , we vary the scales in Eq. (4.6) in the range $\sqrt{2}P_{T,1} \leq \mu_r = \mu_f = \mu'_f \leq 2\sqrt{2}P_{T,1}$. This is depicted in Fig. 4.8 for the unpolarized and polarized cross section. Whereas for COMPASS kinematics the polarized NLO cross section exhibits a somewhat reduced scale dependence, see Fig. 4.3, no significant improvement is found for HERMES kinematics in both the spin-dependent and spin-independent case. Once again, this illustrates the delicacy of a perturbative calculation in a low-energy regime and calls for an unpolarized “reference” measurement to ensure the applicability of pQCD methods. As for COMPASS, no reduction of the scale dependence for different cuts in z_H can be found.

To estimate the sensitivity of the polarized cross section to the spin-dependent parton distributions of the proton, in particular $\Delta g(x, \mu)$, we analyze first the weights of the underlying subprocesses contributing to the di-hadron production at HERMES. Fig. 4.9 shows the unpolarized and polarized ratio of the γq - and γg -channel to the full photoproduction cross section. We find a similar pattern as discussed in connection with Fig. 4.4 above.

Next, we turn to a discussion of the double-spin asymmetry $A_{LL}^{H_1 H_2}$ at HERMES for a deuteron gas target. It is depicted in Fig. 4.10 using the same sets of polarized PDFs as before. The statistical accuracy for such a measurement is again estimated with Eq. (4.14), based on the actual integrated luminosity of $\mathcal{L} = 200 \text{ pb}^{-1}$ collected by HERMES and the parameters as specified above.

One can infer that $A_{LL}^{H_1 H_2}$ is very sensitive to the chosen $\Delta g(x, \mu)$. However, distinguishing different sets with a small gluon polarization like in GRSV, DNS, or DSSV appears to be very difficult with the given experimental accuracy. Statistical significant results can only be obtained in the $P_{T,1}$ -range from 1 to 1.5 GeV.

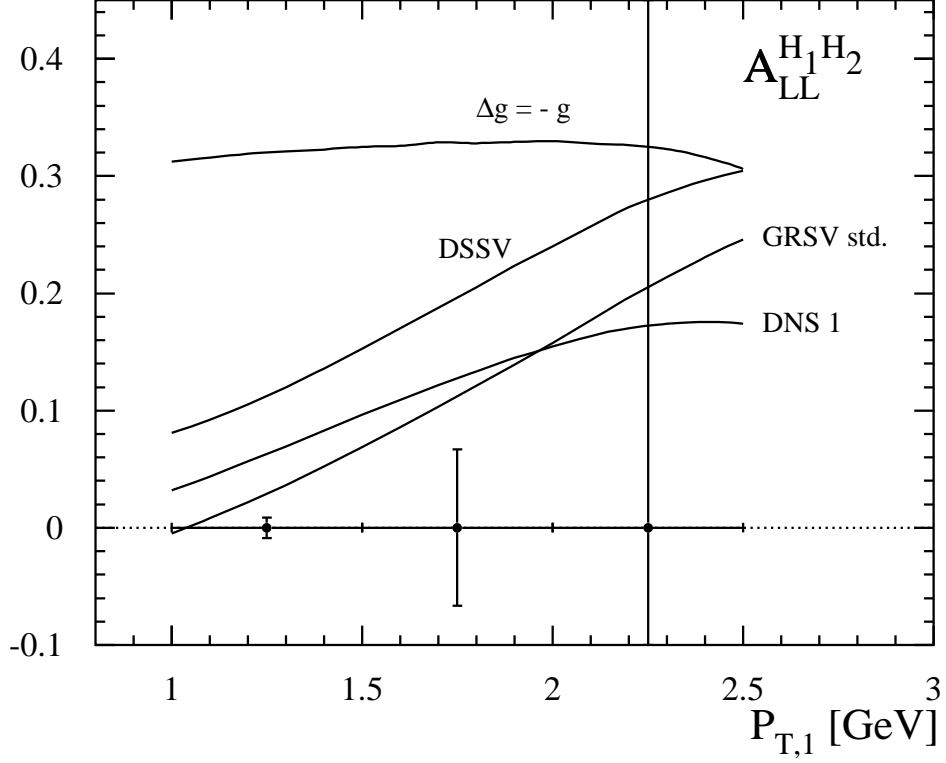


Figure 4.10: As in Fig. 4.5, but now for HERMES kinematics.

Of course, one has to check if the pQCD framework is valid in this region. All caveats mentioned at the end of Sec. 4.1 also apply here.

To close this Section, we note that final HERMES results for $A_{LL}^{H_1H_2}$ and cross sections are in preparation [21].

5 The Monte Carlo Approach

In contrast to the analytic calculation presented in Chapter 3, we give here an alternative method, based on Monte-Carlo (MC) integration techniques. In the analytic approach, the phase space integration over unobserved partons is done exactly, requiring the introduction of the variable z , defined in Eq. (3.70), with the cut $z > 0$. Only the convolution of the hard partonic cross sections with the parton distribution and fragmentation functions is performed with numerical methods. The advantage of this method is that the numerics is fast and reliable. However, we have limited control of the kinematics of hadron H_2 , most notably its rapidity y_2 . This implies that it may end up outside the acceptance of the detectors, making it difficult to compare the theoretical predictions with experimental data. Moreover, the transverse momentum $P_{T,2}$ can only be restricted via a lower bound on z_H , defined in Eq. (3.122). As already mentioned in Chapter 3, the resolved contributions were omitted in the analytic approach, as the computation is very cumbersome.

For these reasons, we pursue here an alternative approach using MC integration techniques already at the partonic level by performing the phase space integration over unobserved partons largely numerically. Singular regions of the phase space are isolated and integrations are performed analytically. Furthermore, histograms for several observables can be evaluated simultaneously, and it is straightforward to implement cuts on the four-momenta of the partons and hadrons, which greatly facilitates the comparison of theoretical predictions with experimental data.

To this end, we use the two cut-off phase space slicing method introduced in Refs. [32, 103]. It provides a relatively simple, transparent, and robust method to isolate the soft (infrared) and collinear singularities. Two cut-off parameters δ_c and δ_s are introduced to separate the regions of phase space containing collinear and soft divergencies from the non-singular regions. This is a well known technique and has been applied to various processes before, e.g., direct jet photoproduction [104], hadronic photon-jet production [105], and di-hadron production in hadronic collisions [106]. In this Chapter we give the relevant steps to perform such a MC calculation for the spin-dependent photoproduction of hadron pairs. For a detailed discussion of this method together with other examples we refer to [32].

We start with the decomposition of the three-body phase space dPS_3 , Eq. (3.53), relevant for the calculation of the polarized partonic $2 \rightarrow 3$ real

emission cross sections $d\Delta\hat{\sigma}^{real}$ at NLO, into a soft (S) and a hard (H) region to be specified below,

$$\begin{aligned} d\Delta\hat{\sigma}_{ab\rightarrow cde}^{real} &= \frac{1}{2s} \int \overline{\sum} \Delta |\mathcal{M}_r|_{ab\rightarrow cde}^2 dPS_3 \\ &= \frac{1}{2s} \int_S \overline{\sum} \Delta |\mathcal{M}_r|_{ab\rightarrow cde}^2 dPS_3 + \frac{1}{2s} \int_H \overline{\sum} \Delta |\mathcal{M}_r|_{ab\rightarrow cde}^2 dPS_3 \\ &= d\Delta\hat{\sigma}_{ab\rightarrow cde}^S + d\Delta\hat{\sigma}_{ab\rightarrow cde}^H, \end{aligned} \quad (5.1)$$

with $1/(2s)$ the flux factor, and $\overline{\sum} \Delta |\mathcal{M}_r|_{ab\rightarrow cde}^2$ the appropriate matrix element for the subprocesses $ab \rightarrow cde$ under consideration, including spin and color factors for averaging and summing over initial and final states, respectively.

This partitioning of phase space introduces a cut-off parameter δ_s . The integration of the soft region S is done analytically in $n = 4 - 2\varepsilon$ space-time dimensions using dimensional regularization. To make this tractable, we apply the eikonal double pole approximation to the matrix element $\Delta |\mathcal{M}_r|_{ab\rightarrow cde}^2$. For a detailed discussion see Sec. 5.1. The result then exhibits single and double poles in $1/\varepsilon$ and single and double logarithms in the soft cut-off parameter δ_s . In principle there are also terms of the order δ_s . However, they can be neglected as we choose δ_s to be small enough.

Collinear singularities are made explicit by a further decomposition of the hard region H into a collinear (HC) and non-collinear ($H\bar{C}$) region

$$\begin{aligned} d\Delta\hat{\sigma}_{ab\rightarrow cde}^H &= d\Delta\hat{\sigma}_{ab\rightarrow cde}^{HC} + d\Delta\hat{\sigma}_{ab\rightarrow cde}^{H\bar{C}} \\ &= \frac{1}{2s} \int_{HC} \overline{\sum} \Delta |\mathcal{M}_r|_{ab\rightarrow cde}^2 dPS_3 \\ &\quad + \frac{1}{2s} \int_{H\bar{C}} \overline{\sum} \Delta |\mathcal{M}_r|_{ab\rightarrow cde}^2 dPS_3, \end{aligned} \quad (5.2)$$

which introduces a second cut-off parameter δ_c . The integration of the collinear region is done analytically in n dimensions, giving rise to single and double poles in $1/\varepsilon$, and single logarithms in δ_c and δ_s . Due to the simpler collinear kinematics, we can apply here the leading pole approximation to the $2 \rightarrow 3$ real emission matrix elements as discussed in Sec. 5.2.

The computation of the virtual $2 \rightarrow 2$ matrix elements follows exactly the procedure outlined in Sec. 3.2. Therefore, we can adopt all the results obtained there. Adding the soft and collinear parts, together with the renormalized, UV finite, one-loop corrections, and factorization counter terms, all poles in $1/\varepsilon^2$ and $1/\varepsilon$ cancel. Thus, the overall result is finite and the limit $\varepsilon \rightarrow 0$ can be taken. However, due to the separation of the three-particle phase space into soft, collinear, and hard regions, there is still an explicit dependence on single and double logarithms of the cut-off parameters δ_s and δ_c .

The remaining integration of the $2 \rightarrow 3$ matrix element over the hard, non-collinear region $H\overline{C}$ is done in four dimensions with solely numerical methods and depends on the cut-off parameters δ_s and δ_c as well through the lower boundaries of the integration. In combination with the soft and collinear regions, the dependence of the cross sections on δ_s and δ_c cancels for suitably defined infrared-safe observables. We start with the calculation of the soft contributions in Sec. 5.1 and App. C, and discuss the integration of the collinear regions in Sec. 5.2 next. Needless to say, the relevant formulas for the unpolarized case are obtained by simply replacing the polarized quantities by the unpolarized counterparts.

5.1 Soft Regions

In this Section we discuss the calculation of the soft part $d\Delta\hat{\sigma}_{ab \rightarrow cde}^S$, separated off the three-particle phase space in Eq. (5.1). Soft divergencies appear in the $2 \rightarrow 3$ matrix elements squared, when an additional unobserved gluon is emitted with vanishing energy. In this case, some approximations can be made leading to a simplification of the phase space and the matrix elements squared for real processes. We adopt the definitions of four-momenta and Mandelstam variables from Chapter 3, see Eqs. (3.45) and (3.47).

With the assumption that the soft gluon in the NLO subprocess $ab \rightarrow cde$ is associated with particle e and four-momentum p_e , the soft and the hard regions are defined via its energy E_e in the c.m.s. frame of the incoming partons a and b and a cut-off parameter δ_s :

$$\begin{aligned} \text{soft} : 0 \leq E_e \leq \delta_s \frac{\sqrt{s}}{2}, \\ \text{hard} : E_e > \delta_s \frac{\sqrt{s}}{2}, \end{aligned} \quad (5.3)$$

with

$$E_e = \frac{s - s_{12}}{2\sqrt{s}}. \quad (5.4)$$

In the three-particle phase space, defined in Eq. (3.53), we can explicitly set $p_e^\mu = 0$ in the Dirac delta-function guaranteeing momentum conservation to obtain for the soft phase space

$$dPS_3 \Big|_{\text{soft}} = dPS_2 \frac{d^{n-1}p_e}{2E_e(2\pi)^{n-1}}, \quad (5.5)$$

with dPS_2 being the usual two particle phase space for partons c and d as defined in Eq. (3.25). We proceed in the c.m.s. frame of the two incoming partons a and b with the following parameterization for the n -momentum of the soft gluon e

$$p_e = E_e(1, \sin \theta_1 \sin \theta_2, \sin \theta_1 \cos \theta_2, \cos \theta_1, \dots). \quad (5.6)$$

The ellipsis denotes the $(n - 4)$ space-time dimensions not further specified in this parameterization. After a trivial integration of the $(n - 4)$ -components of p_e , the differential in Eq. (5.5) takes the form

$$\begin{aligned} d^{n-1}p_e &= d|\vec{p}_e||\vec{p}_e|^{n-2}d\Omega_{n-2} \\ &= dE_e E_e^{n-2} \sin^{n-3}\theta_1 d\theta_1 \sin^{n-4}\theta_2 d\theta_2 \frac{2\pi^{n/2-3/2}}{\Gamma(n/2-3/2)}. \end{aligned} \quad (5.7)$$

Using now Eq. (3.80) and $n = 4 - 2\varepsilon$ the final result for the three particle phase space in the soft approximation can be expressed as

$$dPS_3\Big|_{\text{soft}} = dPS_2 \left[\left(\frac{4\pi}{s} \right)^\varepsilon \frac{\Gamma(1-\varepsilon)}{\Gamma(1-2\varepsilon)} \frac{1}{2(2\pi)^2} \right] dS, \quad (5.8)$$

where

$$dS = \frac{1}{\pi} \left(\frac{4}{s} \right)^{-\varepsilon} \int_0^{\delta_s \frac{\sqrt{s}}{2}} dE_e E_e^{1-2\varepsilon} \sin^{1-2\varepsilon}\theta_1 d\theta_1 \sin^{-2\varepsilon}\theta_2 d\theta_2. \quad (5.9)$$

For the calculation of the matrix elements involving a soft gluon, the eikonal double pole approximation is applied to the full $2 \rightarrow 3$ matrix element squared, computed in Chapter 3, by setting the momentum of the soft gluon to zero. In practice, this is done by carefully taking the limit of the Mandelstam variables, involving the soft gluon momentum p_e , to zero and by expressing the others by $2 \rightarrow 2$ kinematics, i.e.,

$$\begin{aligned} s_{12} &\rightarrow s & t_2 &\rightarrow u & u_2 &\rightarrow t \\ s_{13} &\rightarrow \xi s_{13} & t_3 &\rightarrow \xi t_3 & u_3 &\rightarrow \xi u_3 \\ s_{23} &\rightarrow \xi s_{23} & & & & \end{aligned}, \quad (5.10)$$

with a small dimensionless parameter ξ . After this replacement is done in the matrix elements squared, only the leading terms proportional to $1/\xi^2$, i.e., the double poles, are kept. All others, containing factors ξ , ξ^2 , or $1/\xi$ are set to zero. The next step is the integration of the soft matrix elements over dS , see Eq. (5.9). All relevant integrals and the soft matrix elements squared in case of direct photoproduction processes can be found in Appendix C. For the soft contributions to the resolved photon processes, listed in Eq. (3.50), we refer to [106].

Altogether, the hadronic cross section in the soft limit has the following generic

form

$$\begin{aligned}
d\Delta\sigma^S &= (4\pi\alpha_s)^2 \sum_{a,b,c,d} \int dx_l dx_N dz_1 dz_2 \Delta f_a^l(x_l, \mu_f) \Delta f_b^N(x_N, \mu_f) \\
&\times D_c^{H_1}(z_1, \mu_f') D_d^{H_2}(z_2, \mu_f') \frac{\alpha_s}{2\pi} \left(\frac{4\pi\mu_d^2}{s} \right)^\varepsilon \frac{\Gamma(1-\varepsilon)}{\Gamma(1-2\varepsilon)} \\
&\times \frac{1}{2s} \left[\frac{\mathcal{A}_2^s}{\varepsilon^2} + \frac{\mathcal{A}_1^s}{\varepsilon} + \mathcal{A}_0^s \right] dPS_2,
\end{aligned} \tag{5.11}$$

where we have factored out an overall $(\mu_d^\varepsilon g_s)^2$ from the $2 \rightarrow 3$ matrix element. The $\mathcal{A}_i^s = \mathcal{A}_i^s(ab \rightarrow cd)$ are process-dependent quantities containing single and double logarithms of δ_s and di-logarithms of Mandelstam variables. Again, we refer to App. C for the explicit form of these quantities in the case of direct photo-production, namely the photon-gluon fusion and the QCD Compton processes.

5.2 Collinear Regions

In this Section we present the evaluation of the hard, collinear part $d\Delta\sigma^{HC}$ of the cross section, separated from the soft part in Eq. (5.1) and the hard, non-collinear part in Eq. (5.2). Similar to the soft limit discussed in the previous Section, the phase space simplifies also, if two partons become collinear. Again, the integration is done analytically in $n = 4 - 2\varepsilon$ dimensions leading to single poles in $1/\varepsilon$ and accompanying logarithms of the soft and collinear cut-offs δ_s and δ_c . As discussed in detail in Sec. 2.3, these collinear poles have to be absorbed in the bare parton distribution or fragmentation functions, depending on whether the collinearity is associated with an initial or final state parton leg. Although the concept is the same for both cases, we distinguish in the following between collinear configurations in the initial and in the final state, since some details are different.

5.2.1 Final State Collinearities

To be specific, let us assume that in the NLO $2 \rightarrow 3$ subprocess $ab \rightarrow cde$ the two partons d and e become collinear. The hard collinear region HC in Eq. (5.2) is defined through the condition

$$0 \leq s_{23} \leq \delta_c s, \tag{5.12}$$

introducing another small cut-off parameter δ_c . Using $p_{d'} = p_d + p_e$, the three-particle phase space can be written as

$$dPS_3 \Big|_{coll} = dPS_2 \Big|_{cd'} \frac{d^{n-1}p_e}{2p_e^0(2\pi)^{n-1}} \frac{p_{d'}^0}{p_d^0}, \tag{5.13}$$

with $dPS_2|_{cd'}$ being the two-body phase space for particles c and d' . Now, in the collinear limit, where partons d and e have vanishing relative transverse momentum and longitudinal momentum fraction z and $(1 - z)$ of p'_d , respectively, we obtain [32]

$$\frac{d^{n-1}p_e}{2p_e^0(2\pi)^{n-1}} \frac{p_{d'}^0}{p_d^0} = \frac{(4\pi)^\varepsilon}{16\pi^2\Gamma(1-\varepsilon)} dz ds_{23} [s_{23}z(1-z)]^{-\varepsilon}. \quad (5.14)$$

By virtue of the factorization theorem the $2 \rightarrow 3$ matrix element squared at NLO accuracy factors in the collinear limit in a product of a LO splitting function and a LO matrix element for the process $ab \rightarrow cd'$

$$\overline{\sum} \Delta |\mathcal{M}_{ab \rightarrow cde}|^2 \simeq \overline{\sum} \Delta |\mathcal{M}_{ab \rightarrow cd'}|^2 P_{dd'}^{(u)}(z, \varepsilon) g_s^2 \mu_d^{2\varepsilon} \frac{2}{s_{23}}, \quad (5.15)$$

with $P_{ij}^{(u)}(z, \varepsilon) = P_{ij}^{(4)}(z) + \varepsilon P_{ij}^{(\varepsilon)}(z)$ being the unregulated splitting function in $n = 4 - 2\varepsilon$ dimensions for $z < 1$. They can be found, e.g., in [32]. Note that in Eq. (5.15) the unpolarized splitting function is used, as we consider unpolarized final state partons. This can be interpreted as the collinear splitting of parton d' into the partons d and e .

We then get for the polarized partonic cross section with a collinear configuration in the final state

$$\begin{aligned} d\Delta \hat{\sigma}_{ab \rightarrow cde}^{HC} &= d\Delta \hat{\sigma}_{ab \rightarrow cd'}^{(0)} \left[\frac{\alpha_s}{2\pi} \frac{\Gamma(1-\varepsilon)}{\Gamma(1-2\varepsilon)} \left(\frac{4\pi\mu_d^2}{s} \right)^\varepsilon \right] \left(-\frac{1}{\varepsilon} \right) \delta_c^{-\varepsilon} \\ &\times \int dz [z(1-z)]^{-\varepsilon} P_{dd'}^{(u)}(z, \varepsilon), \end{aligned} \quad (5.16)$$

where $d\Delta \hat{\sigma}_{ab \rightarrow cd'}^{(0)}$ is the appropriate LO partonic cross section for the process $ab \rightarrow cd'$. The integration limits of z are set by the “hard condition” in Eq. (5.3). Depending on the type of process and hence on the splitting functions in Eq. (5.16), the integration limits take different values

$q \rightarrow qg$	$g \rightarrow gg$	$g \rightarrow q\bar{q}$
$0 \leq z \leq 1 - \delta_s$	$\delta_s \leq z \leq 1 - \delta_s$	$0 \leq z \leq 1$

(5.17)

Here, the first of the two final state partons subsequently fragments into one of the observed hadrons. The cut-off parameter δ_s comes into play, if an unobserved gluon can become soft, i.e., for $q \rightarrow qg$ and $g \rightarrow gg$ in (5.17). As we are interested in the production of hadrons not partons, it is necessary to introduce fragmentation functions $D_i^H(z)$. At LO accuracy, this is done by

$$d\Delta \sigma_{ab \rightarrow cH}^{(0)} = d\Delta \hat{\sigma}_{ab \rightarrow cd}^{(0)} D_d^H(z) dz. \quad (5.18)$$

The collinear part of the hard cross section in Eq. (5.2) reads then

$$d\Delta\sigma_{ab\rightarrow cHe}^{HC} = d\Delta\hat{\sigma}_{ab\rightarrow cd'}^{(0)} \left[\frac{\alpha_s}{2\pi} \frac{\Gamma(1-\varepsilon)}{\Gamma(1-2\varepsilon)} \left(\frac{4\pi\mu_d^2}{s} \right)^\varepsilon \right] \left(-\frac{1}{\varepsilon} \right) \delta_c^{-\varepsilon} \\ \times \int dy [y(1-y)]^{-\varepsilon} P_{dd'}^{(u)}(y, \varepsilon) D_d^H(x) dx \delta(xy - z) dz, \quad (5.19)$$

if we assume that parton d fragments in the observed hadron H . The δ -function ensures that H carries a momentum fraction z of the parent parton momentum. Note that we restrict ourselves in Eq. (5.19) to one-hadron production to simplify matters. Of course, for two-hadron production, which we are interested in, parton c also needs to fragment. In addition, c can also be collinear to parton e , and a similar procedure as discussed here needs to be applied. Furthermore, in Eq. (5.19) there is an implied sum over all possible partons d' contributing to the considered process.

As discussed in Sec. 2.3, the collinear singularity has to be factorized and absorbed into the bare fragmentation function, giving rise to a “dressed” function depending on an arbitrary factorization scale μ_f' . The subtraction has the following form in the $\overline{\text{MS}}$ scheme

$$D_i^H(z, \mu_f') = D_i^H(z) - \frac{1}{\varepsilon} \left[\frac{\alpha_s}{2\pi} \frac{\Gamma(1-\varepsilon)}{\Gamma(1-2\varepsilon)} \left(\frac{4\pi\mu_d^2}{\mu_f'^2} \right)^\varepsilon \right] \int_z^1 \frac{dy}{y} D_{i'}^H(z/y) P_{i'i}(y), \quad (5.20)$$

with an implied sum over the index i' and an arbitrary mass scale μ_d introduced in dimensional regularization, see Eq. (2.23). The integration extends from z to 1, in contrast to Eq. (5.19). The splitting function in Eq. (5.20) is now regulated at $z = 1$, see [32] and Eq. (3.107) for the polarized case. Rewriting the bare fragmentation functions in Eq. (5.18) and in Eq. (5.19) in terms of the scale dependent quantity according to Eq. (5.20) and adding up the LO and hard collinear expressions, gives a cancellation between the two singular expressions. However, there are residual terms due to the mismatch in the limits for the y -integration. In the LO expression we have $z \leq y \leq 1$, in the hard collinear expression the integration limits are given in (5.17). We get as final result

$$d\Delta\sigma_{ab\rightarrow cH}^{coll} = d\Delta\sigma_{ab\rightarrow cd'}^{(0)} \left[\frac{\alpha_s}{2\pi} \frac{\Gamma(1-\varepsilon)}{\Gamma(1-2\varepsilon)} \left(\frac{4\pi\mu_d^2}{s} \right)^\varepsilon \right] \left\{ \tilde{D}_{d'}^H(z, \mu_f') \right. \\ \left. + \left[\frac{\mathcal{A}_1^{sc}(d' \rightarrow de)}{\varepsilon} + \mathcal{A}_0^{sc}(d' \rightarrow de) \right] D_d^H(z, \mu_f') \right\} dz, \quad (5.21)$$

where we have omitted terms, which are $\mathcal{O}(\alpha_s^2)$. Here, the soft collinear factors \mathcal{A}_i^{sc} appear due to the different integration limits in the fragmentation and subtraction

pieces, see Eq. (5.17), and are given by

$$\begin{aligned}
\mathcal{A}_1^{sc}(q \rightarrow qg) &= C_F(2 \ln \delta_s + 3/2) \\
\mathcal{A}_1^{sc}(g \rightarrow gg) &= 2C_A \ln \delta_s + (11C_A - 2n_f)/6 \\
\mathcal{A}_1^{sc}(g \rightarrow q\bar{q}) &= 0 \\
\mathcal{A}_0^{sc} &= \mathcal{A}_1^{sc} \ln \left(\frac{s}{\mu_f'^2} \right).
\end{aligned} \tag{5.22}$$

The “modified” fragmentation functions $\tilde{D}_i^H(z, \mu_f)$ in Eq. (5.21) are given by

$$\tilde{D}_i^H(z, \mu_f) = \sum_{i'} \int_z^{1-\delta_s \delta_{ii'}} \frac{dy}{y} D_{i'}^H(z/y, \mu_f') \tilde{P}_{i'i}^{fact}(y), \tag{5.23}$$

with

$$\tilde{P}_{i'i}^{fact}(y) = P_{i'i}^{(4)}(y) \ln \left[\frac{y(1-y)\delta_{cs}}{\mu_f'^2} \right] - P_{i'i}^{(\varepsilon)}(y). \tag{5.24}$$

$P_{ij}^{(4)}(z)$ and $P_{ij}^{(\varepsilon)}(z)$ are the $n = 4$ and $\mathcal{O}(\varepsilon)$ pieces of the unregulated splitting functions $P_{ij}^{(u)}(z, \varepsilon)$ and can be found in [32]. The $\tilde{D}_i^H(z, \mu_f)$ functions contain a dependence on logarithms of δ_s via the integration limits, which give contributions only if $i' = i$.

5.2.2 Initial State Collinearities

As mentioned before, the computation of the initial state singularities follows closely the steps outlined in the previous Subsection. Here, the singularities are absorbed in the bare parton distribution functions, which gives a finite remainder as it is the case for final state collinearities in Eq. (5.21). Since some details of the calculation differ, we briefly derive the relevant formalism, following again closely Ref. [32]. We first concentrate on the details for a collinear configuration in a NLO $2 \rightarrow 3$ subprocess $ab \rightarrow cde$ involving parton b stemming from a nucleon N . Afterwards, we provide the relevant formulas for the direct photon processes $\gamma b \rightarrow cde$. Subtraction terms involving photonic parton densities in a resolved contribution closely resemble those for hadronic parton densities and need not to be discussed here.

Let us consider the collinear emission of parton e off the initial state parton b in a NLO process $ab \rightarrow cde$ with c and d being “observed”. With $u_3 = (p_b - p_e)^2$, the collinear region is defined by

$$0 < -u_3 < \delta_{cs}. \tag{5.25}$$

In this region we can make the approximation $p_b - p_e \simeq yp_b$ and find for the three particle phase space

$$\begin{aligned} dPS_3|_{coll} &= \left[\frac{d^{n-1}p_c}{2p_c^0(2\pi)^{n-1}} \frac{d^{n-1}p_d}{2p_d^0(2\pi)^{n-1}} (2\pi)^n \delta(p_a + yp_b - p_c - p_d) \right] \\ &\times \frac{d^{n-1}p_e}{2p_e^0(2\pi)^{n-1}}. \end{aligned} \quad (5.26)$$

Rewriting the p_e -depending part in terms of y , u_3 , and $n = 4 - 2\varepsilon$ gives

$$\frac{d^{n-1}p_e}{2p_e^0(2\pi)^{n-1}} = \frac{(4\pi)^\varepsilon}{16\pi^2\Gamma(1-\varepsilon)} dy du_3 [-(1-y)u_3]^{-\varepsilon}. \quad (5.27)$$

The integration over u_3 can be performed with the limits determined by Eq. (5.25), and yields

$$\int_0^{\delta_c s} (-du_3)(-u_3)^{-1-\varepsilon} = -\frac{1}{\varepsilon}(\delta_c s)^{-\varepsilon}. \quad (5.28)$$

Similar to Eq. (5.15), the $2 \rightarrow 3$ matrix elements squared can be simplified in the collinear limit

$$\overline{\sum} \Delta |\mathcal{M}_{ab \rightarrow cde}|^2 \simeq \overline{\sum} \Delta |\mathcal{M}_{ab' \rightarrow cd}|^2 \Delta P_{b'b}^{(u)}(y, \varepsilon) g_s^2 \mu_d^{2\varepsilon} \frac{-2}{yu_3}, \quad (5.29)$$

with $\Delta P_{b'b}^{(u)}(y, \varepsilon)$ the unregulated polarized splitting functions. We now take into account that parton b stems from a longitudinally polarized nucleon N and hence introduce the bare polarized parton distribution function Δf_b^N . Combining Eqs. (5.26)-(5.29) we find for the hard collinear cross section

$$\begin{aligned} d\Delta\sigma_{aN \rightarrow cde}^{HC} &= \Delta f_b^N(x/y) d\Delta\hat{\sigma}_{ab' \rightarrow cd}^{(0)}(s, t, t_2) \\ &\times \left[\frac{\alpha_s}{2\pi} \frac{\Gamma(1-\varepsilon)}{\Gamma(1-2\varepsilon)} \left(\frac{4\pi\mu_d^2}{s} \right)^\varepsilon \right] \left(-\frac{1}{\varepsilon} \right) \delta_c^{-\varepsilon} \\ &\times \int \Delta P_{b'b}^{(u)}(y, \varepsilon) \frac{dy}{y} \left[\frac{1-y}{y} \right]^{-\varepsilon}. \end{aligned} \quad (5.30)$$

For simplicity we ignore here the fragmentation of partons c and d into the observed hadron pair. The introduction of a scale dependent parton distribution function in the $\overline{\text{MS}}$ scheme

$$\Delta f_b^N(x, \mu_f) = \Delta f_b^N(x) - \frac{1}{\varepsilon} \left[\frac{\alpha_s}{2\pi} \frac{\Gamma(1-\varepsilon)}{\Gamma(1-2\varepsilon)} \left(\frac{4\pi\mu_d^2}{\mu_f^2} \right)^\varepsilon \right] \int_x^1 \frac{dy}{y} \Delta f_{b'}^N(x/y) \Delta P_{bb'}(y) \quad (5.31)$$

yields the final result for the hard collinear cross section

$$d\Delta\sigma_{aN\rightarrow cde}^{coll} = d\Delta\hat{\sigma}_{ab'\rightarrow cd}^{(0)} \left[\frac{\alpha_s}{2\pi} \frac{\Gamma(1-\varepsilon)}{\Gamma(1-2\varepsilon)} \left(\frac{4\pi\mu_d^2}{s} \right)^\varepsilon \right] \left\{ \Delta\tilde{f}_{b'}^N(x, \mu_f) + \left[\frac{\mathcal{A}_1^{sc}(b \rightarrow b'e)}{\varepsilon} + \mathcal{A}_0^{sc}(b \rightarrow b'e) \right] \Delta f_b^N(x, \mu_f) \right\} dx. \quad (5.32)$$

Here, the factors \mathcal{A}_i^{sc} , defined in Eq. (5.22), depend on the initial-state factorization scale μ_f . The $\Delta\tilde{f}_{b'}^N(x, \mu_f)$ are defined analogously to Eq. (5.23) via

$$\Delta\tilde{f}_b^N(x, \mu_f) = \sum_{b'} \int_x^{1-\delta_s\delta_{bb'}} \frac{dy}{y} \Delta f_{b'}^N(x/y, \mu_f) \Delta\tilde{P}_{bb'}(y), \quad (5.33)$$

with

$$\Delta\tilde{P}_{ij}(y) = \Delta P_{ij}^{(4)}(y) \ln \left(\delta_c \frac{1-y}{y} \frac{s}{\mu_f^2} \right) - \Delta P_{ij}^{(\varepsilon)}(y), \quad (5.34)$$

and again reflect the “mismatch” of the different integration limits. The $\Delta P_{ij}^{(4)}(y)$ are the $n = 4$ parts of the unregulated splitting functions for $y < 1$, defined in Eq. (3.107), and the $\Delta P_{ij}^{(\varepsilon)}$ the $\mathcal{O}(\varepsilon)$ parts

$$\begin{aligned} \Delta P_{qq}^{(\varepsilon)}(y) &= -C_F(1-y), \\ \Delta P_{gq}^{(\varepsilon)}(y) &= 2C_F(1-y), \\ \Delta P_{gg}^{(\varepsilon)}(y) &= 4C_A(1-y), \\ \Delta P_{qg}^{(\varepsilon)}(y) &= -(1-y). \end{aligned} \quad (5.35)$$

Next, we discuss briefly the peculiarities if the incoming quasi-real photon splits collinear into a $q\bar{q}$ -pair, followed by a hard scattering of the (anti-)quark with a parton of the nucleon. In the absence of gluons collinear to the photon, there are no soft singularities. In this case, Eq. (5.32) can be simplified to

$$d\Delta\sigma_{\gamma b \rightarrow cde}^{coll} = d\Delta\hat{\sigma}_{qb \rightarrow cd}^{(0)} \left[\frac{\alpha_s}{2\pi} \frac{\Gamma(1-\varepsilon)}{\Gamma(1-2\varepsilon)} \left(\frac{4\pi\mu_d^2}{s} \right)^\varepsilon \right] \Delta\tilde{f}_q^\gamma(x, \mu_f), \quad (5.36)$$

with

$$\begin{aligned} \Delta\tilde{f}_q^\gamma(x, \mu_f) &= \int_x^1 \frac{dy}{y} \Delta f_\gamma^\gamma\left(\frac{x}{y}, \mu_f\right) \Delta\tilde{P}_{q\gamma}(y) \\ &= \int_x^1 \frac{dy}{y} \delta\left(1 - \frac{x}{y}\right) \Delta\tilde{P}_{q\gamma}(y) = \Delta\tilde{P}_{q\gamma}(x). \end{aligned} \quad (5.37)$$

The $n = 4$ and $\mathcal{O}(\varepsilon)$ parts of the $q\gamma$ splitting functions are given by

$$\begin{aligned}\Delta P_{q\gamma}^{(4)}(y) &= C_A(2y - 1) \\ \Delta P_{q\gamma}^{(\varepsilon)}(y) &= -2C_A(1 - y) .\end{aligned}\tag{5.38}$$

Now, in the MC approach all possible soft and collinear configurations have to be treated with the “building blocks” given in the previous two Sections.

6 Phenomenological Applications of the Monte-Carlo Method

This Chapter is dedicated to detailed phenomenological studies of the photoproduction of hadron pairs at high transverse momenta including now both direct and resolved contributions. We use here the concept of the two cut-off phase space slicing method [32] introduced in Chapter 5 and phase space integrations are performed largely numerically. This enables us to organize our calculations such that they resemble the experimental conditions of COMPASS and HERMES as closely as possible. As in Chapter 4, where we discussed the results obtained within our analytic approach, we give the relevant unpolarized and polarized cross sections differential in the transverse momentum $P_{T,1}$ of hadron H_1 , as well as K -factors and double-spin asymmetries $A_{LL}^{H_1 H_2}$ for different sets of spin-dependent parton distributions. We also study the cross sections differential in kinematic variables like the angle in the transverse plane between the two produced hadrons and the momentum fractions x_N and x_l probed in the nucleon and lepton. As parton distribution functions for circularly polarized photons have not been measured yet, we will also focus on the dependence of the polarized cross sections on two extreme models introduced in Sec. 2.3.

At LO, the contributing processes are the QCD Compton process, Eq. (3.14), and the photon gluon fusion, Eq. (3.15), in addition to the resolved contributions as given in Eq. (3.16). At NLO, we have the same processes as in LO, now including virtual corrections together with the real processes having an additional particle in the final state, see Eq. (3.49) for the direct case, and Eq. (3.50) for the resolved case. Needless to say, for all NLO $2 \rightarrow 3$ processes we have to take into account all different combinatorical possibilities as only two of the three final state partons fragment into the observed hadron pair.

For the unpolarized parton distributions we again employ the CTEQ6 [56] and GRV [69] sets for the nucleon and photon, respectively. In the polarized case, the helicity-dependent DSSV distributions [24] are used for nucleons, if not stated otherwise. The two extreme sets for the polarized photonic distribution functions [71] we use in the calculation are shown in Fig. 2.5 of Sec. 2.3. As not stated otherwise, we choose the “maximal saturation” scenario in all our calculations. For the fragmentation functions, the sets of DSS [73] are employed.

In Sec. 6.1 we first scrutinize the numerical stability of our MC code by compar-

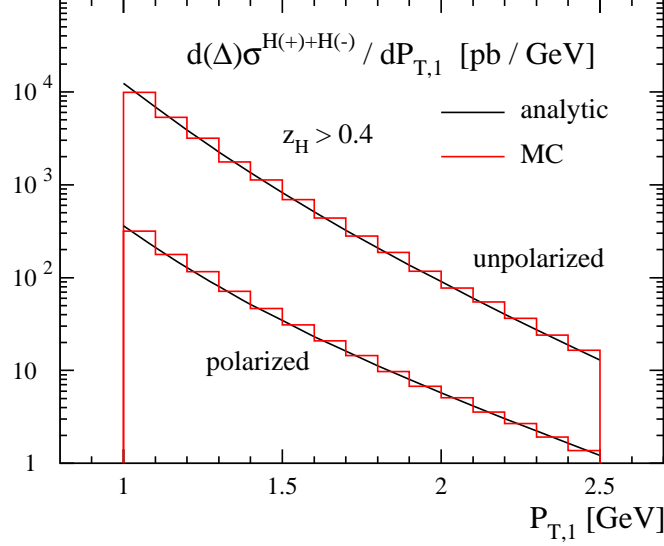


Figure 6.1: The direct photon contribution to the unpolarized and polarized photoproduction cross section at COMPASS applying the cut $z_H > 0.4$. The results are obtained within the analytic calculation (lines) and the MC approach (histograms).

ing it to the predictions obtained within the analytic calculation. Furthermore, we study the dependence of the results on the soft and collinear cut-off parameters δ_s and δ_c , respectively, and show, in what regions the calculation is stable. In Sec. 6.2 we turn to phenomenological studies using COMPASS kinematics, whereas Sec. 6.3 is dedicated to results for the HERMES experimental setup.

6.1 Testing the Stability of the MC Code

Figure 6.1 shows a comparison of the direct photon contribution to the unpolarized and polarized photoproduction cross section, obtained within the analytic and MC approach. We restrict hadron H_1 to be in the COMPASS detector acceptance ($\theta_1^{\max} = 180 \text{ mrad}$), and constrain the transverse momentum of hadron H_2 by demanding $z_H > 0.4$. No cut on the rapidity of hadron H_2 is made. As in Chapter 4, all scales are set equal to twice the transverse momentum of hadron H_1 . There is a good agreement between the two methods over three orders in magnitude, which validates the correctness of our results, as both calculations have been performed independently using different methods.

Next, we study how the two-body, comprising LO, virtual, collinear, and soft

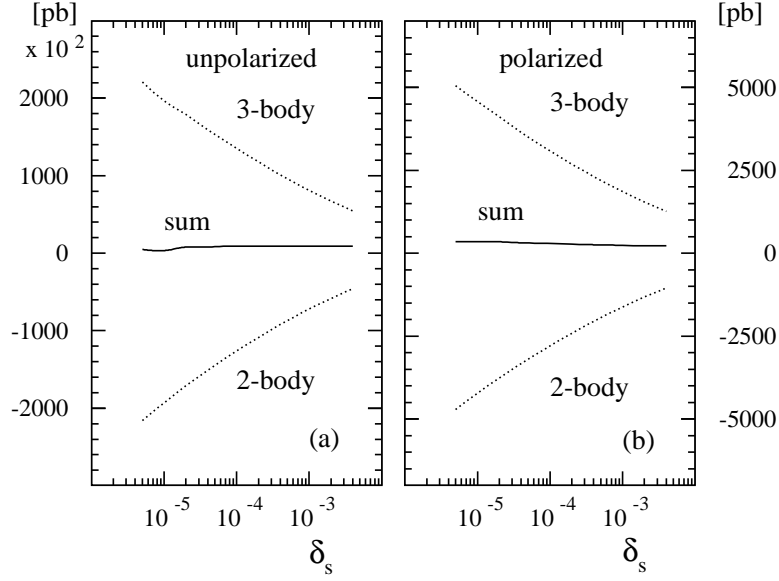


Figure 6.2: The full unpolarized (a) and polarized (b) NLO photoproduction cross section at COMPASS and the individual two-body and three-body contributions (see text) together with their sum as a function of the soft cut-off parameter δ_s . The collinear cut-off parameter is set to $\delta_c = \delta_s/50$ [32].

parts, and the three-body contribution depend on the soft and collinear cut-off parameters δ_s and δ_c , respectively, and to what extent this dependence cancels in the sum. Figure 6.2 shows the results for the unpolarized and polarized cross section of di-hadron photoproduction at COMPASS as a function of δ_s . The collinear cut-off parameter is chosen to be $\delta_c = \delta_s/50$, as it has been shown that this choice yields good results and possible correction terms proportional to $\text{Li}_2(\delta_c/\delta_s)$ are negligible [32]. In Fig. 6.2, we have integrated over the rapidity and transverse momenta of both hadrons with cuts on the angles in the laboratory frame, $\theta_{1,2} < 180 \text{ mrad}$, and their transverse momenta, $P_{T,1,2} > 0.7 \text{ GeV}$. In the unpolarized case, the three-body contribution develops numerical instabilities if $\delta_s \lesssim 10^{-5}$, resulting in an inaccurate result for the total cross section. This calls for a choice for δ_s in the range $10^{-5} \lesssim \delta_s \lesssim 10^{-2}$. If the cut-offs are chosen too large, the results become unreliable as we neglect all non-logarithm contributions in δ_s and δ_c . In the polarized case, the situation is different, as it involves much more delicate cancellations of the individual subprocesses. The full polarized cross section shows a dependence on the cut-off parameter δ_s in a wider range than in the unpolarized case. This dependence will be investigated more thoroughly in our further studies [35]. For the time being, we take $\delta_s = 10^{-3}$ in all our calculations, which guarantees numerically stable results.

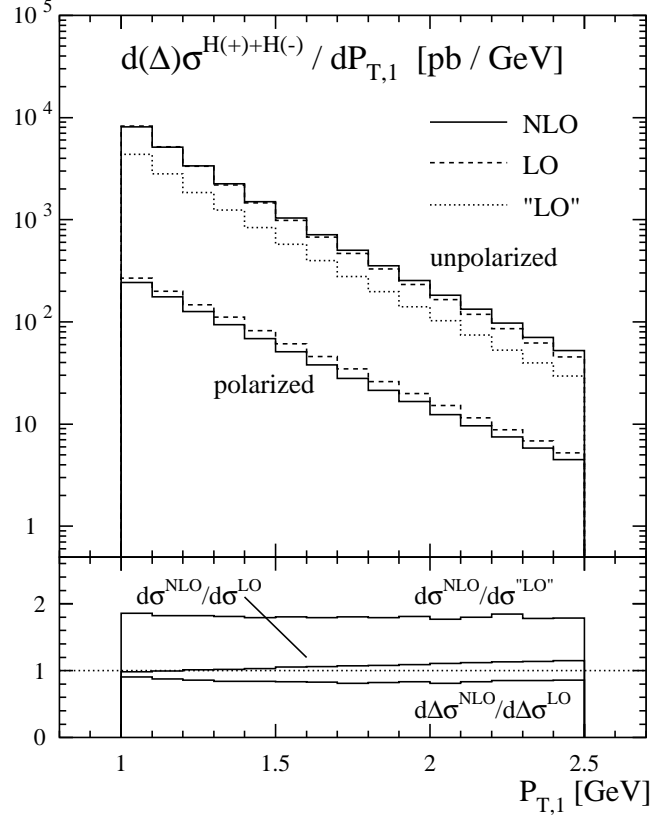


Figure 6.3: Unpolarized and polarized photoproduction cross section for a pair of charged hadrons, $\mu d \rightarrow (H_1^+ + H_1^-)(H_2^+ + H_2^-)X$, at LO (dashed) and NLO (solid) accuracy using COMPASS kinematics. Results are obtained with a MC code and include the direct and resolved parts. The lower panel shows the ratios of NLO to LO cross sections (K -factor). The curve labeled “LO” refers to a LO calculation using NLO parton densities and fragmentation functions (see text).

6.2 Results for COMPASS Kinematics

Within the MC approach, we have complete control of all kinematical variables and four-momenta of the hadrons and partons taking part in the hard scattering. This enables us to choose the cuts close to the experimental setup of COMPASS: The transverse momenta $P_{T,1}$ and $P_{T,2}$ of the hadrons H_1 and H_2 are required to be larger than 0.7 GeV . The angles of the hadrons relative to the beam axis are restricted to be smaller than 180 mrad , which translates into a minimal bound on the (pseudo)rapidity according to Eqs. (4.2) and (4.4). We again choose the

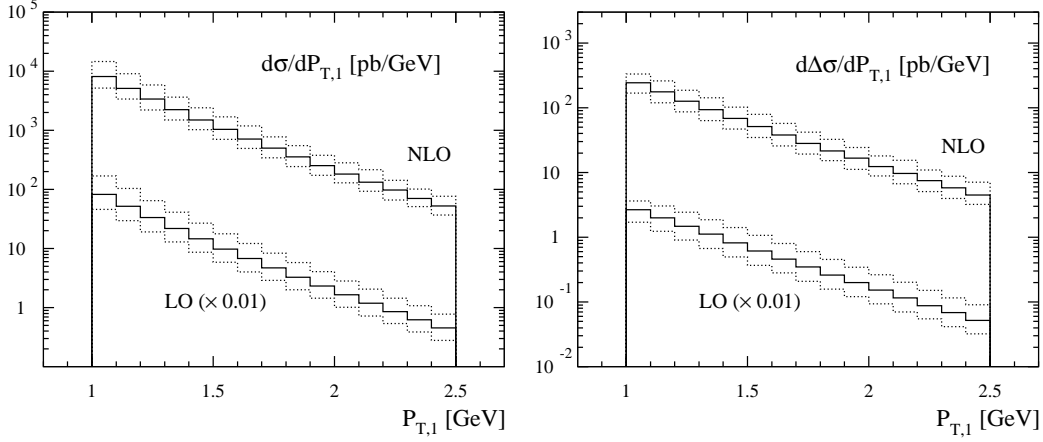


Figure 6.4: Unpolarized and polarized photoproduction cross section at COMPASS. All scales are set equal and varied in the range $1/\sqrt{2}(P_{T,1} + P_{T,2}) \leq \mu \leq \sqrt{2}(P_{T,1} + P_{T,2})$ (dotted lines). The solid lines correspond to the default choice, where $\mu = P_{T,1} + P_{T,2}$. All LO computations have been rescaled by a factor 0.01 to better distinguish them from the NLO results.

fraction y of the muon's momentum taken by the quasi-real photon to be in the range $0.1 < y < 0.9$. The maximal virtuality of the photon in the Weizsäcker-Williams equivalent photon spectrum, see Eq. (2.57), is chosen to be $Q_{\text{max}}^2 = 0.5 \text{ GeV}^2$. The momentum fractions z_1 and z_2 of the two final state partons fragmenting into the observed hadrons are bounded by $z_{1,2} > 0.1$. In addition, we make a cut on the invariant mass of the two hadrons: $M(H_1, H_2) > 1.5 \text{ GeV}$. This is to avoid configurations, where the two observed hadrons become collinear. If not stated otherwise, we have chosen the renormalization and factorization scales equal to the sum of the transverse momenta of the two hadrons H_1 and H_2 : $\mu_r = \mu_f = \mu'_f = P_{T,1} + P_{T,2}$.

In order to test the importance of NLO corrections, the upper panel of Fig. 6.3 shows our predictions for the unpolarized and polarized photoproduction cross section at LO and NLO accuracy and differential in the transverse momentum $P_{T,1}$ of hadron H_1 . The lower panel shows the resulting unpolarized and polarized K -factors as defined in Eq. (4.13). The NLO corrections to the cross sections seem to be small, with K -factors of around 1 both in the polarized and unpolarized case. The K -factor is often associated with a measure of the relevance of NLO corrections to hadronic processes. However, this proposition has to be taken with some care. To illustrate this, we performed a calculation using LO partonic cross sections and NLO parton distribution and fragmentation functions, as has been done also in our studies within the analytic approach in Chapter 4. This

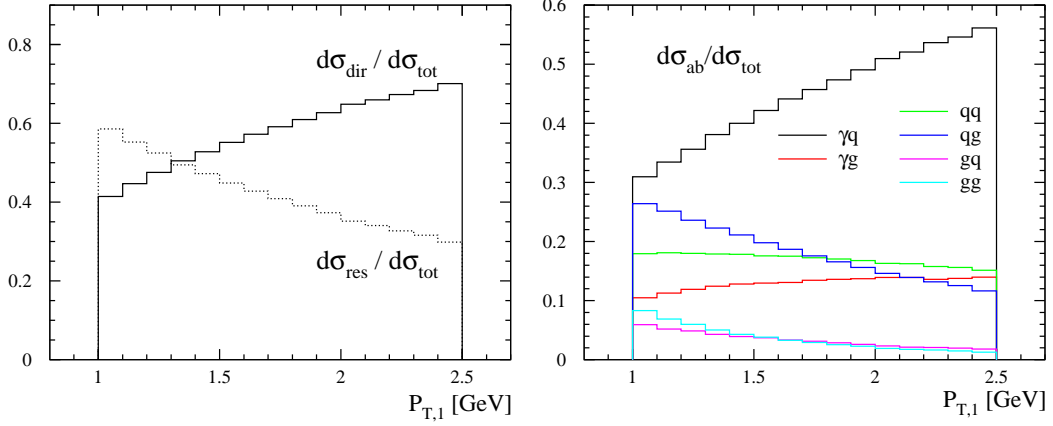


Figure 6.5: Relative contributions of the direct and resolved cross sections (left panel) and the contributing subprocesses $ab \rightarrow cdX$, summed over all final states c, d (right panel), to the full unpolarized photoproduction cross section at COMPASS.

“LO”-type calculation, also shown in Fig. 6.3, leads to a K -factor of roughly 2. Hence, all statements about the large difference in the LO and NLO fragmentation functions of DSS given in Sec. 4.1 also hold true, when all experimental cuts and both resolved and direct photon contributions are included.

In Fig. 6.4 we give the dependence of the unpolarized and polarized cross section at LO and NLO on the unphysical renormalization/factorization scales varied in the range $1/\sqrt{2}(P_{T,1}+P_{T,2}) \leq \mu \leq \sqrt{2}(P_{T,1}+P_{T,2})$. The LO curves are scaled by a factor 0.01. Going to NLO accuracy gives a somewhat reduced scale dependence for the unpolarized and polarized cross sections. As already stated in Chapter 4, a check of the applicability of pQCD at relatively low scales requires benchmark measurements of the unpolarized cross section.

Next, we discuss the relevance of the direct and resolved part to the full photoproduction cross section. The left panel of Fig. 6.5 shows their fractional contribution to the unpolarized cross section differential in the transverse momentum $P_{T,1}$. The resolved contribution dominates in the low $P_{T,1}$ -region, whereas the direct part takes over towards higher $P_{T,1}$ ’s. This behavior can be understood by a closer inspection of the relative weights of the individual subprocesses, shown in the right panel of Fig. 6.5. The cross section for the direct γq -channel dominates over the whole $P_{T,1}$ -range. However, due to the relatively small γg -contribution, the resolved processes, mainly qq and qg scattering, become more important in the low $P_{T,1}$ -region than the direct channels. This demonstrates the necessity to include resolved contributions in an extraction of $\Delta g(x, \mu)$ via double-spin

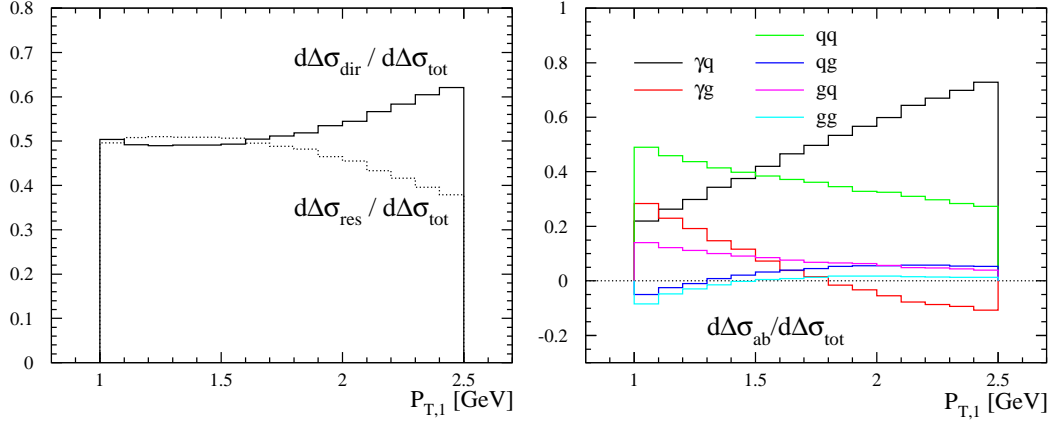


Figure 6.6: The same as in Fig. 6.5, but now for the polarized case.

asymmetries $A_{LL}^{H_1 H_2}$.

The left panel of Fig. 6.6 shows the direct and resolved photon contributions to the full photoproduction cross section in the polarized case. They balance each other in the low-to-mid $P_{T,1}$ -region. Only towards the high $P_{T,1}$ -region the direct part gains in size and becomes more important. To understand this better we again display the relative weights of the individual partonic channels to the full polarized cross section in the right panel of Fig. 6.6. This is also important in order to explore the sensitivity of the polarized hadronic cross section to the spin-dependent parton distributions of the proton, in particular $\Delta g(x, \mu)$, and of the resolved photon. In the low $P_{T,1}$ -region, the process where the photon resolves into a (anti)quark and subsequently scatters off a quark out of the nucleon, has the largest contribution. This is in striking contrast to the naive expectation that at moderate c.m.s. energies the direct part of the cross section dominates. Only towards higher $P_{T,1}$ the γq -channel exceeds all other processes in magnitude. The interesting processes sensitive to the helicity-dependent gluon distribution $\Delta g(x, \mu)$, i.e., the γg -, qg -, and gg -channels, are less important, mainly due to the relatively small polarized gluon distribution $\Delta g(x, \mu)$ in the DSSV parameterization, see Fig. 4.1.

For a reliable extraction of $\Delta g(x, \mu)$, it is imperative to precisely determine its Bjorken x -dependence. In the left panel of Fig. 6.7 we show the polarized cross section differential in the fraction x_N of the nucleon's momentum taken by the produced parton. We apply the cuts on kinematical variables as specified in the beginning of this Section and integrate both hadrons with a lower bound on $P_{T,1}$ and $P_{T,2}$ of 0.7 GeV. The distribution for x_N in the left panel of Fig. 6.7 peaks at a value of around 0.2. This underlines the importance of COMPASS data, which are complementary to RHIC proton-proton data, predominantly probing

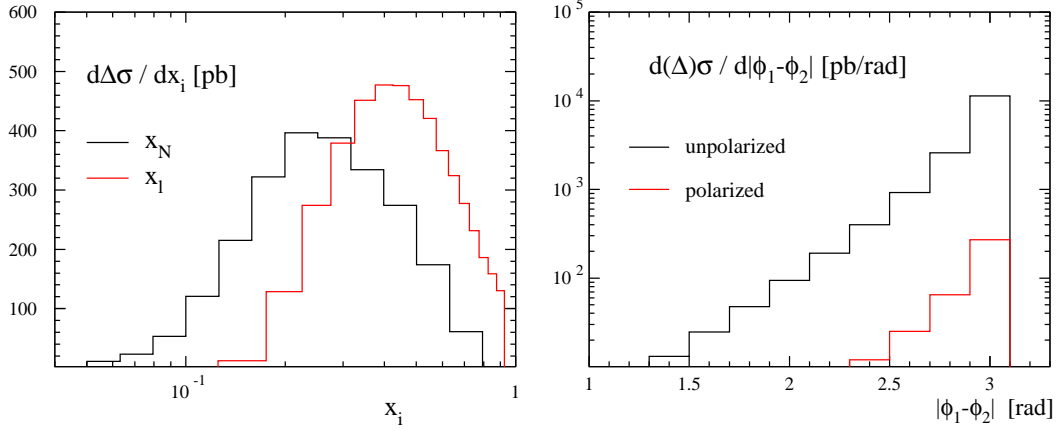


Figure 6.7: The left panel shows the polarized NLO photoproduction cross section at COMPASS as a function of the momentum fractions x_N [x_l] of the nucleon [lepton] taken by the partons. The right panel gives the polarized cross section differential in the difference of the two azimuthal angles $|\Phi_1 - \Phi_2|$ of the hadrons.

smaller momentum fractions x_N . Also shown is the fraction x_l of the muon’s momentum taken by the produced photon (direct case) or parton (resolved case). The distribution has its maximum at $x_l \simeq 0.4$. Differences in the “maximal” and “minimal” scenario of the polarized photon distribution function are due to the input for the hadronic, non-perturbative contribution and are important in the low-to-mid x_l region, see Fig. 2.5. Thus, for COMPASS energies these effects play a small but non-negligible role.

Next, it is interesting to investigate the angles Φ_1 and Φ_2 of the two produced hadrons in a plane perpendicular to the beam axis. The right panel of Fig. 6.7 shows the unpolarized and polarized cross section as a function of the difference of the two azimuthal angles $|\Phi_1 - \Phi_2|$. We note that it is most likely to find the two hadrons at an angle of π , i.e., back-to-back in the transverse plane. This stems mostly from LO contributions, virtual corrections, and soft and collinear parts, where the transverse momenta must balance each other due to momentum conservation leading to $|\Phi_1 - \Phi_2| = \pi$. Contributions at small angles $|\Phi_1 - \Phi_2| \simeq 0$ are avoided by the cut on the invariant mass of the two hadrons: $M(H_1, H_2) > 1.5 \text{ GeV}$.

Having studied the relevance of the individual subprocesses and the dependence of the cross sections on various kinematic variables and on the unphysical factorization and renormalization scales, we now turn the actual quantity of interest in di-hadron photoproduction: the double-spin asymmetry $A_{LL}^{H_1 H_2}$, defined

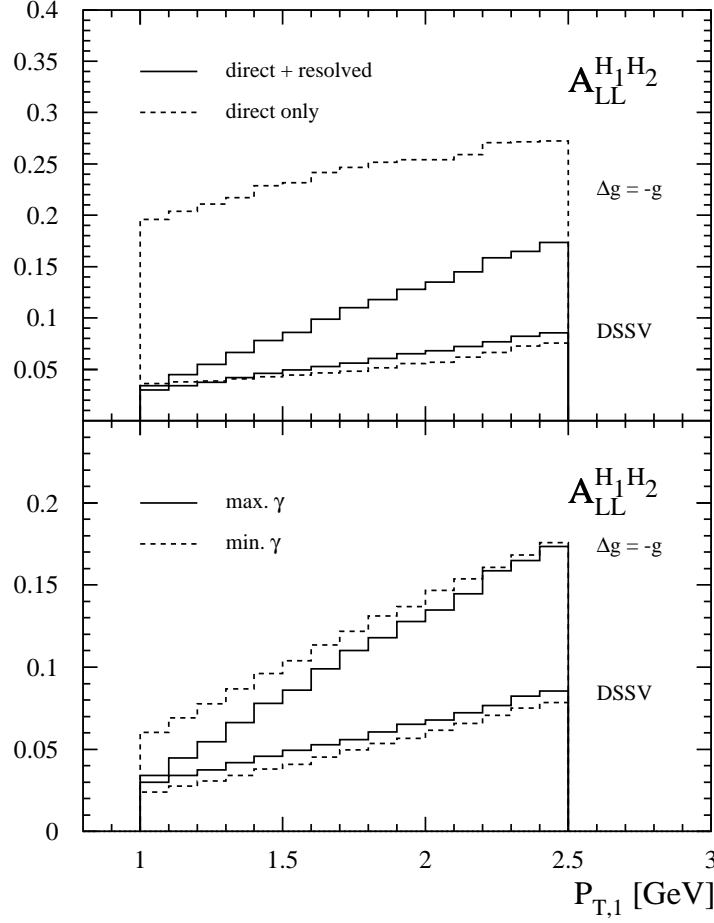


Figure 6.8: Double-spin asymmetry $A_{LL}^{H_1 H_2}$ at NLO for two sets of polarized parton densities at COMPASS. The upper panel shows the spin asymmetry with (solid lines) and without (dashed lines) including the resolved contribution. In the lower panel the dependence of $A_{LL}^{H_1 H_2}$ on the two extreme photon scenarios, “maximal” (solid lines) and “minimal” saturation (dashed lines), is shown.

in Eq. (3.6). In Fig. 6.8 we have plotted our expectations for $A_{LL}^{H_1 H_2}$ as a function of the transverse momentum $P_{T,1}$. Apart from the recent set of DSSV polarized parton densities with a small gluon polarization, we also use the set of GRSV based on a maximal negative $\Delta g(x, \mu)$ at the input scale. $A_{LL}^{H_1 H_2}$ turns out to be very sensitive to the assumed gluon polarization and thus can help to further our knowledge of it. Of course, one has to keep in mind the actual errors of 0.019 (stat.) and 0.003 (syst.) for such a measurement at COMPASS [20].

In the upper panel of Fig. 6.8 we study the influence of the resolved photon contribution on the double-spin asymmetry by comparing the results with (solid lines) and without (dashed lines) including the resolved contributions. One can immediately infer that the resolved part is non-negligible, resulting in a significant, $P_{T,1}$ -depending shift in the absolute value of the spin asymmetry. Neglecting it in the analysis would clearly lead to wrong conclusions about $\Delta g(x, \mu)$. This has also been demonstrated in our analytic LO study [23], see Fig. 4.6 in Sec. 4.1. Figure 6.8 also shows that the region $P_{T,1} > 1.5 \text{ GeV}$ is the most promising one to obtain information about the gluon polarization, as for smaller $P_{T,1}$ the asymmetries almost coincide.

The impact of the completely unknown, non-perturbative parton content of the circularly polarized photon on $A_{LL}^{H_1 H_2}$ is examined in the lower panel of Fig. 6.8 by making use of the two extreme models shown in Fig. 2.5 of Sec. 2.3. As can be seen, there is a fairly significant dependence on the models complicating the analysis of $A_{LL}^{H_1 H_2}$ in terms of $\Delta g(x, \mu)$. The reason is because one probes the partonic structure of the photon at momentum fractions x_l , where the details of the unknown hadronic input play some role, as has been demonstrated in the left panel of Fig. 6.7. Now, a viable strategy could be to analyze data in two regions for the angles $\theta_{1,2}$. In the lower region the dependence of $A_{LL}^{H_1 H_2}$ on the models for the circularly polarized photon plays a much less significant role. The higher region might then be used for studying the non-perturbative structure of the photon polarization.

6.3 Results for HERMES Kinematics

The results given in this Section are intended to resemble the kinematics of the HERMES experiment at DESY. All cuts and settings for kinematic variables are chosen similar to the cuts given in Sec. 4.2. However, we can now ensure to find both hadrons in the acceptance of the HERMES detector, i.e., the angles $\theta_{1,2}$ of the two hadrons relative to the incoming lepton beam are restricted to be in the range $40 \text{ mrad} \leq \theta_{1,2} \leq 220 \text{ mrad}$. Additionally we assume the transverse momenta of the two hadrons to have values larger than 1 GeV . If not stated otherwise, the renormalization and factorization scales are set equal to the sum of the two transverse momenta $\mu_r = \mu_f = \mu'_f = P_{T,1} + P_{T,2}$, as usual.

The upper panel of Fig. 6.9 shows the unpolarized and polarized photoproduction cross section for HERMES kinematics at LO (dashed lines) and NLO (solid lines) accuracy as a function of the transverse momentum of hadron H_1 . In addition, the lower panel gives the unpolarized and polarized K -factors. As for COMPASS kinematics, K -factors seem to be close to one, in particular, for the polarized case. Again, this has to be taken with some care, as a calculation with

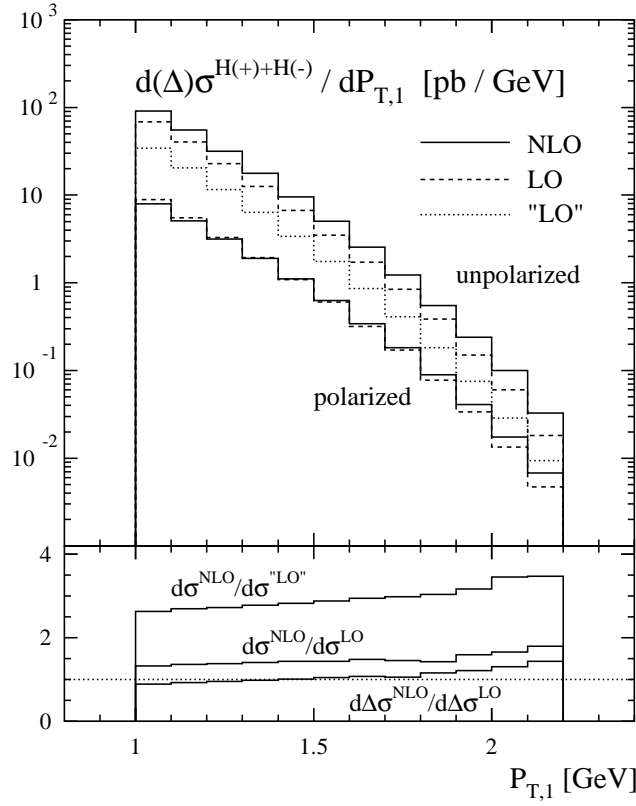


Figure 6.9: The same as in Fig. 6.3, but now for the process $ed \rightarrow (H_1^+ + H_1^-)(H_2^+ + H_2^-)X$ and HERMES kinematics.

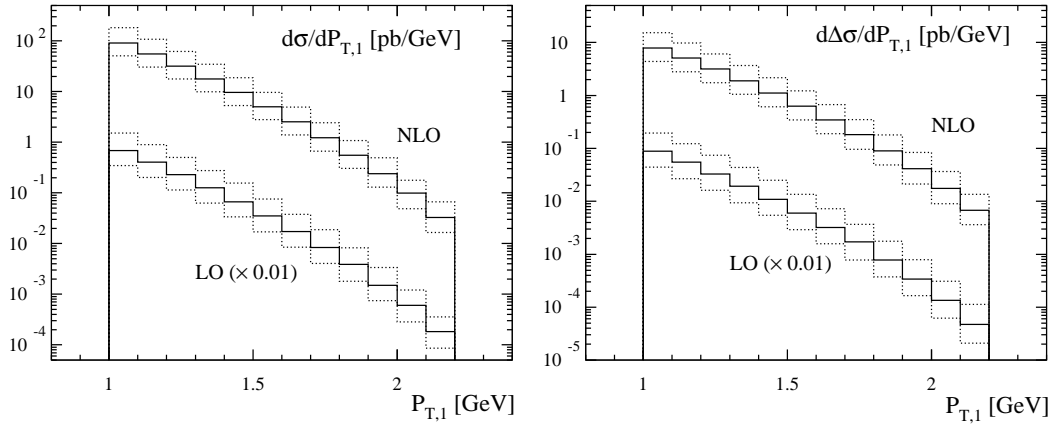


Figure 6.10: The same as in Fig. 6.4, but now for HERMES kinematics.

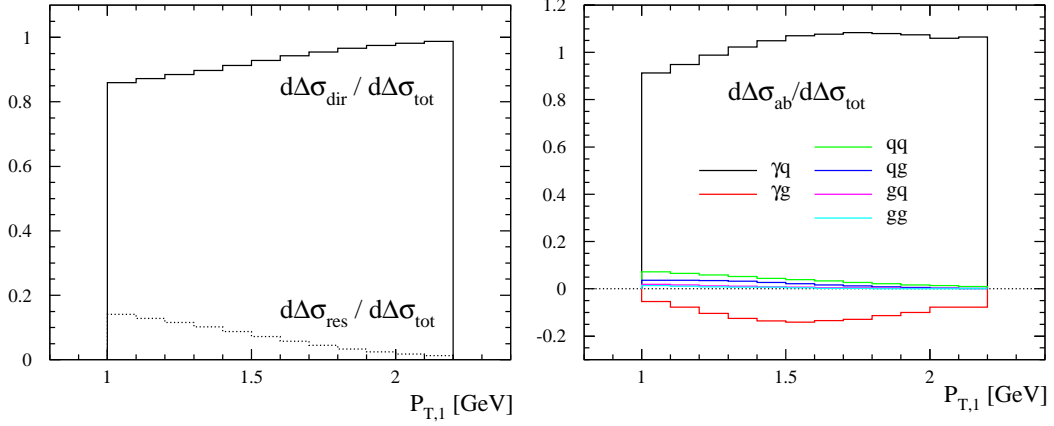


Figure 6.11: The same as in Fig. 6.6, but now for HERMES kinematics.

LO partonic cross sections and NLO parton distribution and fragmentation functions yields a K -factor in the unpolarized case of roughly 3. The lower panel of Fig. 6.9 also shows that NLO corrections do not cancel in double-spin asymmetry $A_{LL}^{H_1 H_2}$, as it is often naively assumed.

In Fig. 6.10 we give the dependence of both the unpolarized (left panel) and polarized (right panel) LO and NLO photoproduction cross section on the unphysical renormalization and factorization scales varied in the range $1/\sqrt{2}(P_{T,1} + P_{T,2}) \leq \mu \leq \sqrt{2}(P_{T,1} + P_{T,2})$. Not unexpectedly, due to the smaller c.m.s. energy of the HERMES experiment, the scale dependence is even larger than for COMPASS, see Fig. 6.4, and does not decrease, when NLO corrections are included. All remarks about potential problems with the applicability of perturbative methods at fixed-target energies and the need for unpolarized “benchmark” cross sections also apply here.

Next, we turn to the relevance of the direct and resolved photon contributions. The left panel of Fig. 6.11 shows their respective relative contributions to the full polarized photoproduction cross section. Here, the resolved contribution plays a much less significant role than at COMPASS kinematics due to the smaller c.m.s. energy at HERMES. The ratios of the individual subprocesses to the unpolarized cross section are given in the right panel of Fig. 6.11. The direct γq -channel dominates over the entire $P_{T,1}$ -range, whereas the γg -channel is small and negative. Similar results can be found in the unpolarized case, where the γq - and γg -channel contribute about 80% and 15%, respectively, to the full unpolarized photoproduction cross section.

In the left panel of Fig. 6.12 the polarized photoproduction cross section at HERMES is shown as function of the momentum fractions x_N and x_l of the nucleon and lepton taken by the parton/photon. The distribution for x_N peaks at

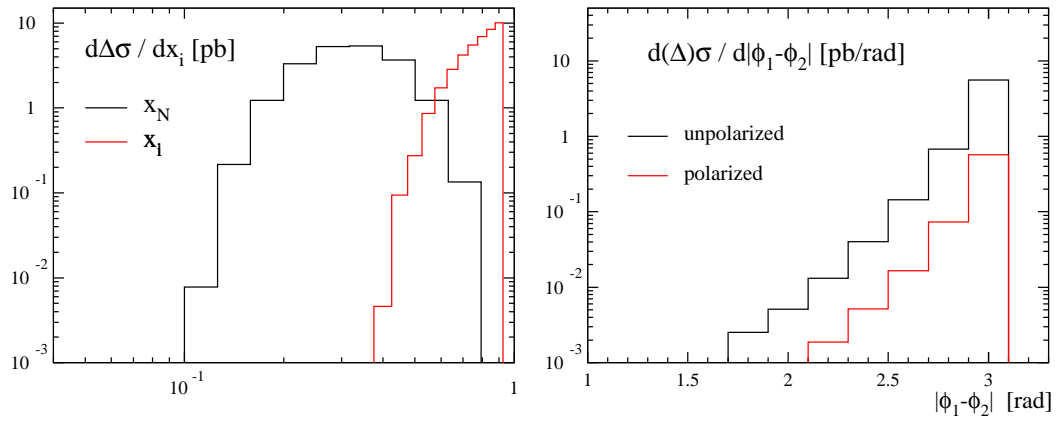


Figure 6.12: The same as in Fig. 6.7, but now for HERMES kinematics.

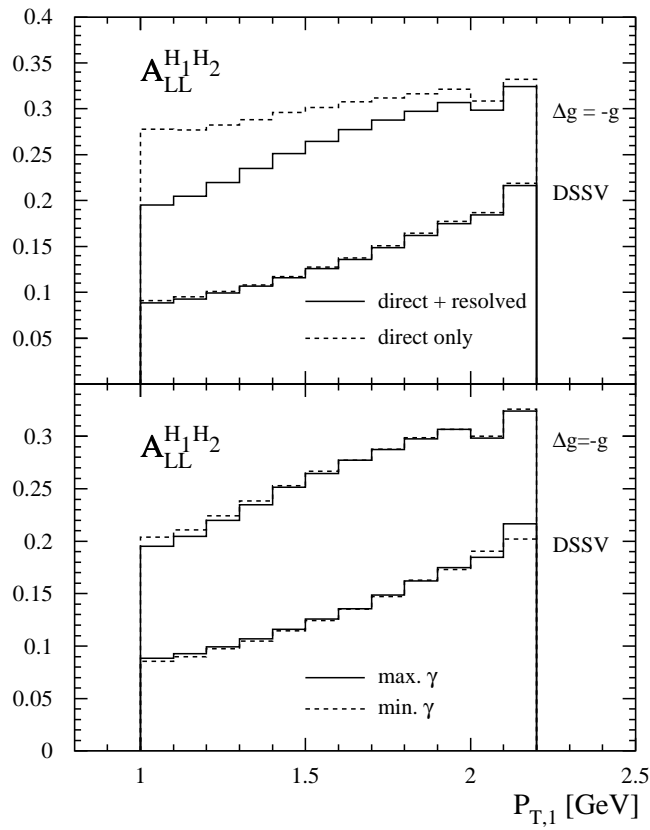


Figure 6.13: The same as in Fig. 6.8, but now for HERMES kinematics.

somewhat higher values of $x_N \simeq 0.3$ than for COMPASS, see Fig. 6.7, which is mainly due to the lower c.m.s. energy available at HERMES. The distribution for the momentum fraction x_l of the electron taken by the photon or parton, respectively, has its maximum in the high x_l -region, where differences between the “minimal” and “maximal” scenarios of the photonic parton distributions do not matter much as we will see below.

The right panel of Fig. 6.12 gives the unpolarized and polarized photoproduction cross section as a function of the difference of the two azimuthal angles $|\Phi_1 - \Phi_2|$. As for COMPASS, most contributions are close to π , which resembles back-to-back kinematics and stems from the LO, virtual, soft, and collinear contributions.

Next, we consider the corresponding double-spin asymmetry $A_{LL}^{H_1 H_2}$ in Fig. 6.13. As in Fig. 6.8 we study the relevance of the resolved photon contribution in the upper panel and the dependence on models for the non-perturbative partonic structure of circularly polarized photons in the lower panel of Fig. 6.13. Here, the resolved photon processes have a much less pronounced effect on the spin asymmetry than for COMPASS, see Fig. 6.8. Also, there is almost no difference between the results obtained with the two extreme models for the Δf_γ densities. This is because for the same transverse momentum $P_{T,1}$ the HERMES experiment is closer to the end of the phase space than COMPASS, since on average HERMES probes larger momentum fractions both in the nucleon and in the photon, see the left panel of Fig. 6.12, which explains our results.

To close this Section, we note that final results from the HERMES experiment for $A_{LL}^{H_1 H_2}$ will become available in the near future [21].

7 Summary and Conclusions

In this work, we provided for the first time the theoretical framework for the longitudinally polarized photoproduction of hadron pairs at next-to-leading order of perturbative QCD. This process is regarded as an important tool in the quest for a better understanding of the spin structure of the nucleon. The results presented in this Thesis can now be applied in quantitative analyses of di-hadron photoproduction data available from the COMPASS and HERMES experiments. For the first time, it will be possible now to include such data consistently in a NLO global QCD analysis of helicity dependent parton densities of the nucleon, in particular the elusive gluon polarization. Two-hadron production will also test our understanding and the applicability of factorization and perturbative QCD at relatively low scales.

We started with a short overview of the underlying theory, Quantum Chromodynamics, and gave an introduction to the renormalization and factorization procedures, both essential ingredients for any calculation in perturbative QCD beyond the leading order approximation.

Next, we turned to a detailed derivation of all relevant formulas for the longitudinally polarized photoproduction of two hadrons at high transverse momenta in a fully analytic approach. To make the calculation tractable, we introduced the variable z_H to avoid certain singular kinematic regions, which are beyond the realm of the standard factorization theorem. Nevertheless, the analytic approach turned out to be considerably more challenging than for one-hadron inclusive cross sections, and we had to limit ourselves to the direct photon contribution. In addition, it is difficult to match our results to the conditions in experiment. This is because some kinematic cuts, e.g., on the angular detector acceptance, can not be implemented in the calculation. However, to our knowledge a fully analytic computation of di-hadron photoproduction cross section at the next-to-leading order of pQCD has never been performed before, not even in the unpolarized case, which is interesting and important in its own right. Furthermore, the analytic results serve as an important benchmark for a more versatile, but numerically delicate Monte-Carlo integration technique, which we also pursued in this Thesis.

The results of the calculation were then implemented in a phenomenological analysis with the kinematic cuts as close as possible to the experimental setup. We demonstrated that the K -factors as a “measure” for the relevance of NLO

corrections depend more on the details of the non-perturbative parton distribution and fragmentation functions than on the hard partonic scattering. To get a better feeling for the typical theoretical ambiguities, we studied the dependence of our results on the unphysical factorization and renormalization scales introduced by theory. Although unpolarized cross sections show little or no improvement, the scale dependence of polarized cross sections, in particular for COMPASS, is somewhat reduced when the next-to-leading order corrections are included. This might be taken as some first indication that the perturbative series is well behaved at COMPASS energies. Future comparisons of, not yet available, cross section data with theory will ultimately decide this and may call for further refinements of the theoretical calculations like resummations of dominant contributions to all orders in the strong coupling. Contrary to naive expectations NLO corrections do not cancel in the experimentally relevant double-spin asymmetry, which was shown to be very sensitive to the chosen polarized gluon scenario, proving that di-hadron photoproduction can further our understanding of the spin structure of the nucleon.

To include also the resolved photon contribution to di-hadron production, which is required for a consistent factorization, we used an alternative, more versatile approach based on Monte-Carlo integration techniques. Within this method one has complete control of all kinematic variables and hence can implement all cuts required by the experimental setup. In practice, we chose the “two cut-off phase space slicing method”, which requires the introduction of two small cut-off parameters to separate off the divergent regions of phase space. Whereas these singular regions can be treated analytically, the remaining portion of the phase space was handled solely numerically. After showing how this method works in practice and outlining the relevant framework, we first tested the Monte-Carlo integration by comparing it to our analytical results. Both methods turned out to be in good agreement. Next, we studied the stability of the numerical integrations, i.e., we demonstrated the independence of our results on the small cut-off parameters, which involves delicate numerical cancellations.

After verifying our Monte-Carlo code, we presented detailed results for unpolarized and polarized cross sections and double-spin asymmetries for both COMPASS and HERMES kinematics as a function of the transverse momentum of one of the hadrons. In addition, we studied the dependence on other kinematic variables like the momentum fractions probed in the nucleon and lepton or the difference in the azimuthal angles of the two observed hadrons. We also demonstrated that the spin asymmetries are largely independent of the details of the non-perturbative hadronic structure of circularly polarized photons, which is completely unknown. The resolved contribution is important though, as it leads to a systematic shift of the spin asymmetries. Neglecting it would lead to wrong conclusions about, e.g., hadronic parton densities including the gluon polarization.

Detailed studies of spin-dependent processes will certainly provide a much better understanding of hadronic spin structure than we have today. The results of this Thesis will contribute to this effort. It will be now possible to include data for di-hadron photoproduction in future global NLO analyses of the spin content of the nucleon. We close with pointing out that the results provided here, in particular the versatile Monte-Carlo code, will prove to be valuable in studies for the planned first polarized lepton-proton collider. If the EIC project will be realized in the future, it will open up a new window for the exploration of the hadronic and photonic spin structure.

A Feynman Rules

In this Appendix we present the Feynman rules of QCD, necessary for the calculations of amplitudes $i\mathcal{M}$. Flavor and spinor indices are implicitly understood and not shown here.

The propagators for fermions, gluons, and ghosts are

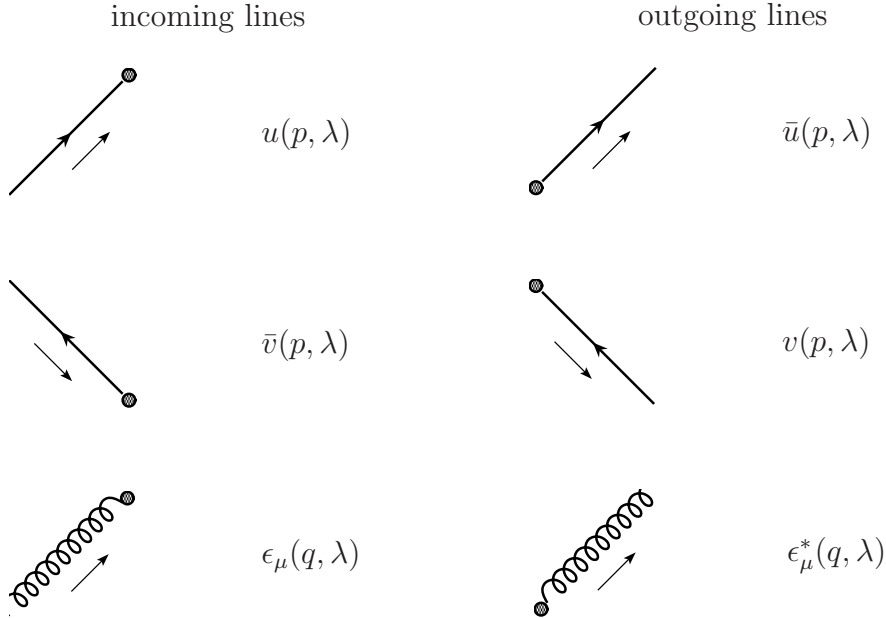
$$i \xrightarrow{p} j \qquad i\delta_{ij}\frac{1}{\not{p}-m+i\epsilon'} = i\delta_{ij}\frac{\not{p}+m}{p^2-m^2+i\epsilon}$$

$$\frac{-i\delta_{ab}}{p^2 + i\epsilon} \left(g^{\mu\nu} - (1 - \eta) \frac{p^\mu p^\nu}{p^2} \right)$$

$$a \overset{p}{\dashrightarrow} b \qquad \frac{-i\delta_{ab}}{p^2 + i\epsilon}$$

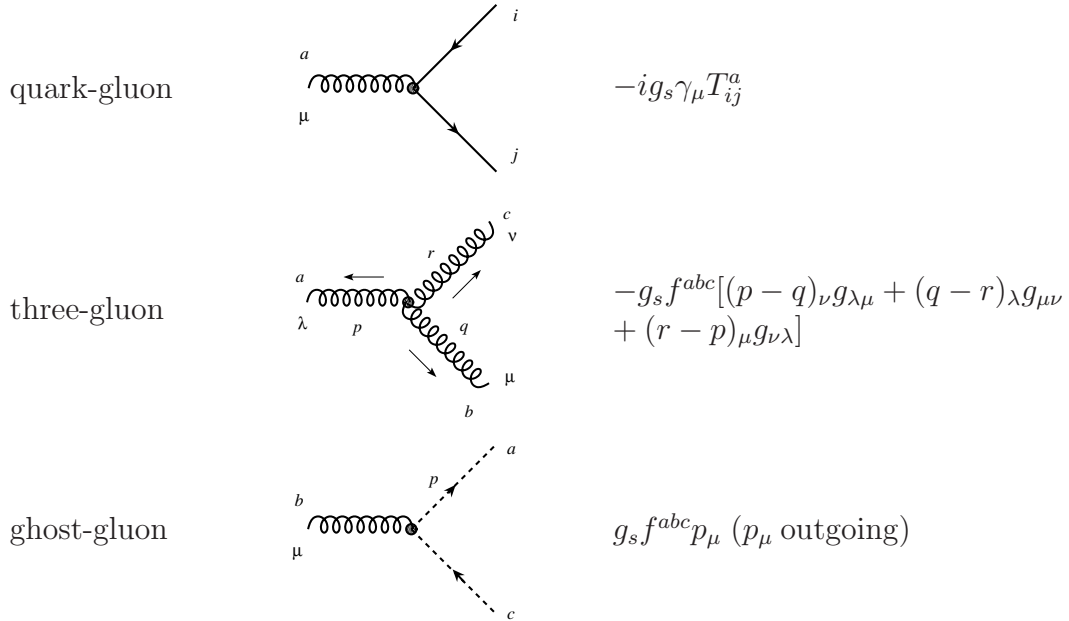
Here $i, j, (a, b)$ denote the color indices of the quarks (gluons or ghosts). Greek letters like μ, ν are Lorentz indices. p denotes the momentum of the respective particle, and \not{p} is a shortcut for $p_\mu \gamma^\mu$. The $i\epsilon$ prescription in the denominator of all propagators ensuring causality can be neglected in all our calculations. ϵ should not be confused with the ε in $n = 4 - 2\varepsilon$. The parameter η depends on the used gauge. As mentioned in Section 2.1, we use the Feynman gauge ($\eta = 1$) in all our calculations.

The external quark, antiquark, and gluon legs are represented by

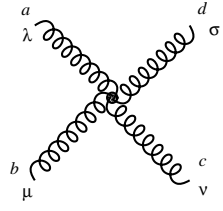


$u(p, \lambda)$ and $v(p, \lambda)$ denote the spinors of a quark and an antiquark with momentum p and helicity λ . $\epsilon_\mu(q, \lambda)$ is the polarization vector of a gluon with momentum q and helicity λ .

An important ingredient for calculations of Feynman diagrams are the vertices:



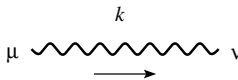
four-gluon



$$\begin{aligned}
& -ig_s^2 f^{abe} f^{cde} (g_{\lambda\nu} g_{\mu\sigma} - g_{\lambda\sigma} g_{\mu\nu}) \\
& -ig_s^2 f^{ace} f^{bde} (g_{\lambda\mu} g_{\nu\sigma} - g_{\lambda\sigma} g_{\mu\nu}) \\
& -ig_s^2 f^{ade} f^{cbe} (g_{\lambda\nu} g_{\mu\sigma} - g_{\lambda\mu} g_{\sigma\nu})
\end{aligned}$$

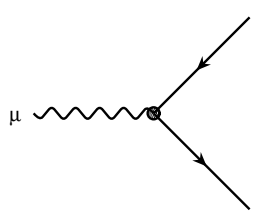
In addition to the pure QCD-processes we need also the Feynman rules for photons:

photon propagator



$$-i \frac{g_{\mu\nu}}{k^2 + i\epsilon}$$

photon-quark vertex



$$-ig_e \gamma_\mu$$

As for gluons, incoming photon legs are represented by polarization vectors $\epsilon_\mu(q, \lambda)$ with momentum q and helicity λ .

For the computation of diagrams in NLO accuracy and beyond, one has to keep in mind some additional rules:

- multiplication with a factor (-1) for each closed fermion or ghost loop
- integration over the loop momentum k for each closed loop with a measure

$$\int \frac{d^n k}{(2\pi)^n}$$

After calculating the amplitude $i\mathcal{M}$ with the rules just presented, the next step is to work out the squared absolute value of the amplitude, i.e., $|\mathcal{M}|^2 = \mathcal{M}\mathcal{M}^*$. To perform this step, one needs projection operators for quarks, antiquarks, and

massless bosons with definite helicities:

$$u(p, \lambda) \bar{u}(p, \lambda) = \frac{1}{2}(\not{p} + m)[1 - \gamma_5 \lambda], \quad (\text{A.1})$$

$$v(p, \lambda) \bar{v}(p, \lambda) = \frac{1}{2}(\not{p} - m)[1 + \gamma_5 \lambda], \quad (\text{A.2})$$

$$\epsilon^\mu(q, \lambda) \epsilon^{\nu*}(q, \lambda) = \frac{1}{2} \left[-g^{\mu\nu} + \frac{q^\mu \eta^\nu + q^\nu \eta^\mu}{q \cdot \eta} + i\lambda \epsilon^{\mu\nu\rho\sigma} \frac{q_\rho \eta_\sigma}{q \cdot \eta} \right], \quad (\text{A.3})$$

where η is an arbitrary, light-like momentum with $q \cdot \eta \neq 0$.

B Phase Space Integrals

In this Appendix we discuss in detail the calculation of all phase space integrals appearing in an analytic NLO calculation of hadron pair production and needed throughout this work. We give explicit results with special emphasis on the correct treatment of plus-distributions and the singularity structure of the integrals. We start with single propagators, namely the $I_1(X_i)$, defined in Eq. (3.97), which exhibit a singular behavior in either w or z . Next, we compute the integrals with double propagators, $I_1(X_i X_j)$, which can, in general, develop singularities in both w and z . For some derivations we closely follow [80, 90, 96].

B.1 Single Propagators $I_1(X_i)$

- $I_1(t_2), I_1(u_2)$

Here the X_{i0} , a_i , and b_i in Eq. (3.93) take the form

$$X_{i0} \equiv t_{20} = -\frac{sv}{2}, \quad a_i = 1 - \cos \psi \cos \theta_1, \quad b_i = \pm \sin \psi \sin \theta_1.$$

Inserting

$$a_i^2 - b_i^2 = (\cos \psi - \cos \theta_1)^2 = 4z^2 \cos^2 \psi,$$

in Eq. (3.98), a potential singularity occurs for $z = 0$. However, this case is avoided as we always ensure that $z > 0$, and we safely can take the limit $\varepsilon \rightarrow 0$ ending up with

$$I_1(t_2) = \frac{\pi}{2t_{20}} \frac{1}{\cos \psi} \frac{1}{z}. \quad (\text{B.1})$$

The result for $I_1(u_2)$ is similar, with a factor $u_{20} = -s(1 - v)/2$ in the denominator instead of t_{20} .

- $I_1(s_{12})$

In this case,

$$X_{i0} \equiv s_{120} = \frac{s(1 - v + vw)}{2}, \quad a_i = 1 - \cos \psi', \quad b_i = -\sin \psi' \sin \theta_1,$$

$$a_i^2 - b_i^2 = 4 \left[z + \frac{v(1 - w)}{1 - v + vw} \right]^2 \cos^2 \psi.$$

As $0 < v, w < 1$, a singularity would occur for negative values of z . Again, as only positive values are allowed for z , we can treat this integral in four dimensions instead of n to obtain the result

$$I_1(s_{12}) = \frac{\pi}{2s_{120}} \frac{1}{\cos \psi} \frac{1}{z + \frac{v(1-w)}{1-v+vw}}. \quad (\text{B.2})$$

- $I_1(t_3), I_1(u_3)$

Here,

$$X_{i0} \equiv t_{30} = -\frac{sv}{2}, \quad a_i = 1 + \cos \psi \cos \theta_1, \quad b_i = \pm \sin \psi \sin \theta_1, \\ a_i^2 - b_i^2 = 4(1-z)^2 \cos^2 \psi.$$

This yields a singularity in Eq. (3.98) at $z = 1$, when the unobserved parton is emitted collinearly to the beam axis defined by the incoming particles. This pole needs to be factorized into the bare parton distributions, as explained in Sec. 2.3. From Eq. (3.98) we obtain

$$I_1(t_3) = \frac{\pi}{2t_{30} \cos \psi} \frac{1}{|1-z|^{1+2\varepsilon}} \left(\frac{\overbrace{1 + \cos^2 \psi (1-2z)}^{\equiv 2h(z)}}{\cos \psi} \right)^{2\varepsilon} \\ \times \frac{\Gamma(1-2\varepsilon)}{\Gamma^2(1-\varepsilon)} {}_2F_1\left(\frac{1}{2} - \varepsilon, -\varepsilon; 1 - \varepsilon; \frac{b_i^2}{a_i^2}\right). \quad (\text{B.3})$$

If $z \rightarrow 1$, also $b_i^2/a_i^2 \rightarrow 1$. In this limit the hyper-geometric function can be expanded as

$${}_2F_1\left(\frac{1}{2} - \varepsilon, -\varepsilon, 1 - \varepsilon; 1\right) = 2^{-2\varepsilon} \left[1 + \mathcal{O}(\varepsilon^2)\right]. \quad (\text{B.4})$$

First, let us consider the range $z \in [1; z_{\max}]$. By using partial fractioning, expanding in powers of ε , and disregarding all terms which vanish in the limit $\varepsilon \rightarrow 0$, we find

$$\int_0^{z_{\max}} dz f(z) \frac{\theta(z-1)}{(z-1)^{1+2\varepsilon}} \left(\frac{h^2(z)}{g(z)} \right)^\varepsilon = \\ \int_0^{z_{\max}} dz f(z) \left[\frac{\theta(z-1)}{(z-1)^{1+2\varepsilon}} \left(\frac{h^2(z)}{g(z)} \right)^\varepsilon \right]_+ \\ + f(1) \left[-\frac{1}{2\varepsilon} + \ln(z_{\max}-1) - \frac{1}{2} \ln \left(\frac{h^2(1)}{g(1)} \right) \right]. \quad (\text{B.5})$$

$h(z)$ is defined in Eq. (B.3), and $g(z)$ is defined in Eq. (3.79). With

$$\theta(z-1) \left[\left(\frac{h^2(z)}{g(z)} \right)^\varepsilon \frac{1}{(z-1)^{1+2\varepsilon}} \right]_+ = \frac{\theta(z-1)}{(z-1)_+} + \mathcal{O}(\varepsilon),$$

and $1 - z_{\max} = z_{\min}$, this can be written as

$$\begin{aligned} \frac{\theta(z-1)}{(z-1)^{1+2\varepsilon}} \left(\frac{h(z)^2}{g(z)} \right)^\varepsilon &= \frac{\theta(z-1)}{(z-1)_+} + \delta(z-1) \\ &\times \left[-\frac{1}{2\varepsilon} + \ln(-z_{\min}) - \frac{1}{2} \ln \left(\frac{h^2(1)}{g(1)} \right) \right]. \end{aligned} \quad (\text{B.6})$$

With a similar calculation in the range $z \in [0; 1]$ we get the combined result

$$\begin{aligned} \frac{1}{|1-z|^{1+2\varepsilon}} \left(\frac{h^2(z)}{g(z)} \right)^\varepsilon &= \frac{\theta(1-z)}{(1-z)_+} + \frac{\theta(z-1)}{(z-1)_+} \\ &+ \delta(1-z) \left(-\frac{1}{\varepsilon} - \ln(z_{\max}) \right). \end{aligned} \quad (\text{B.7})$$

The final result for Eq. (B.3) reads

$$\begin{aligned} g(z)^{-\varepsilon} I_1(t_3) &= \frac{\pi}{2t_{30} \cos \psi} \frac{\Gamma(1-2\varepsilon)}{\Gamma^2(1-\varepsilon)} \\ &\times \left[\delta(1-z) \left(-\frac{1}{\varepsilon} - \ln(z_{\max}) \right) + \frac{\theta(1-z)}{(1-z)_+} + \frac{\theta(z-1)}{(z-1)_+} \right]. \end{aligned} \quad (\text{B.8})$$

The same result is obtained for $I_1(u_3)$ via replacing the prefactor t_{30} by $u_{30} = -s(1-vw)/2$.

- $I_1(s_{13})$

In this case

$$\begin{aligned} X_{i0} &\equiv s_{130} = \frac{1-v+vw}{2}, \\ a_i &= 1 + \cos \psi' \cos \theta_1, \quad b_i = \sin \psi' \sin \theta_1, \\ a_i^2 - b_i^2 &= 4 \left(z - \frac{1}{1-v+vw} \right)^2 \cos^2 \psi. \end{aligned} \quad (\text{B.9})$$

Here we run into a singularity at $z = 1/(1-v+vw) \equiv z_1$. Applying the same procedure as for $I_1(t_3)$ but replacing 1 by z_1 , and defining plus

distributions in the ranges $[0; z_1]$ and $[z_1; z_{\max}]$ the final result is

$$\begin{aligned}
 g(z)^{-\varepsilon} I_1(s_{13}) &= \frac{\pi}{2s_{130} \cos \psi} \frac{\Gamma(1-2\varepsilon)}{\Gamma^2(1-\varepsilon)} \\
 &\times \left[\delta(z_1 - z) \left(-\frac{1}{\varepsilon} - \ln \left(1 - \frac{z_{\min}}{z_1} \right) \right) \right. \\
 &\left. + \frac{\theta(z - z_1)}{(z - z_1)_+} + \frac{\theta(z_1 - z)}{(z_1 - z)_+} \right]. \quad (\text{B.10})
 \end{aligned}$$

- $I_1(s_{23})$

s_{23} has no dependence on the integration angle θ_2 . However, it exhibits a factor $(1-w)$ which is expanded via Eq. (3.102) leading to

$$(1-w)^{-\varepsilon} I_1(s_{23}) = \frac{I_0}{sv} \left[-\frac{1}{\varepsilon} \delta(1-w) + \frac{1}{(1-w)_+} - \varepsilon \left(\frac{\ln(1-w)}{1-w} \right) \right]. \quad (\text{B.11})$$

I_0 is specified in Eq. (3.96).

B.2 Double Propagators $I_1(X_i X_j)$

- $I_1(t_3 u_2), I_1(t_2 u_3)$

Using the expansion for $1/(X_i X_j)$ of Eq. (3.100) we encounter a factor $1/(1-2z)$, which diverges for $z = 1/2$. As this singularity has no physical interpretation we have to remove it by expanding

$$\frac{1}{z} \rightarrow \frac{\theta(1-z)}{z} + \frac{\theta(z-1)}{z}, \quad (\text{B.12})$$

in $I_1(u_2)$. The final result takes the form

$$\begin{aligned}
 g(z)^{-\varepsilon} I_1(t_3 u_2) &= \frac{\pi}{4t_{30} u_{20} \cos^3 \psi} \frac{\Gamma(1-2\varepsilon)}{\Gamma^2(1-\varepsilon)} \\
 &\times \left[\delta(1-z) \left(-\frac{1}{\varepsilon} - \ln z_{\max} \right) + \frac{\theta(1-z)}{z(1-z)_+} \right. \\
 &\left. + \theta(z-1) \left(\frac{1}{(z-1)_+} + \frac{1+2z}{(1-2z)z} \right) \right]. \quad (\text{B.13})
 \end{aligned}$$

The result for $I_1(t_2 u_3)$ is obtained with replacing $t_{30} u_{20}$ by $t_{20} u_{30}$ in Eq. (B.13).

- $I_1(t_3 u_3)$

A detailed discussion of this integral can be found in [90]. Hence, we only give the final result

$$\begin{aligned}
g(z)^{-\varepsilon}(1-w)^{-\varepsilon}I_1(t_3 u_3) &= \frac{\pi}{t_{30}u_{30}} \frac{\Gamma(1-2\varepsilon)}{\Gamma^2(1-\varepsilon)} \frac{1}{2\cos\psi} \left\{ (1-vw) \right. \\
&\times \left(\frac{\theta(1-z)}{[D_1(1-z)]_+} + \frac{\theta(z-1)}{[D_1(z-1)]_+} \right) + \delta(1-z) \left[-\frac{1-vw}{1-w} \right. \\
&\times \ln\left(\frac{\cos\psi + \cos^{-1}\psi}{2}\right) + v\left(-\frac{1}{\varepsilon} + \ln\left(\frac{(1-w)^2}{1-vw}\right)\right) \\
&- (1-v) \left[\left(\frac{1}{\varepsilon} + \ln(1-v)\right) \frac{1}{(1-w)_+} - 2\left(\frac{\ln(1-w)}{1-w}\right)_+ \right. \\
&\left. \left. + \frac{1}{1-w} \ln\left(\frac{1-vw}{1-v}\right) \right] \right] + \delta(1-z)\delta(1-w) \\
&\times \left(\frac{1}{2\varepsilon^2} + \frac{1}{2\varepsilon} \ln(1-v) + \frac{1}{4} \ln^2(1-v) \right) (1-v) \left. \right\}, \tag{B.14}
\end{aligned}$$

where $D_1 \equiv 1 - w + 2(1 - z)w(1 - v)$.

- $I_1(t_3 s_{23}), I_1(u_3 s_{23})$

Integrals with this structure exhibit singularities both in $z = 1$ and $w = 1$ due to an additional factor $1/(1 - w)$ stemming from $1/s_{23}$. A detailed discussion can be found in [80]. The result is

$$\begin{aligned}
g(z)^{-\varepsilon}(1-w)^{-\varepsilon}I_1(t_3 s_{23}) &= \frac{\pi}{2svt_{30}\cos\psi} \frac{\Gamma(1-2\varepsilon)}{\Gamma^2(1-\varepsilon)} \left\{ -\frac{1}{\varepsilon}\delta(1-w) \right. \\
&\times \left[-\frac{1}{\varepsilon}\delta(1-z) + \theta(1-z) \left(\frac{1}{(1-z)_+} - \varepsilon \frac{\ln z}{1-z} \right. \right. \\
&\left. \left. - \varepsilon \left(\frac{\ln(1-z)}{1-z} \right)_+ \right) \right] + \frac{1}{(1-w)_+} \left(-\frac{1}{\varepsilon}\delta(1-z) + \frac{\theta(1-z)}{(1-z)_+} \right) \\
&\left. + \frac{1}{1-w} \left(\frac{\theta(z-1)}{(z-1)_+} - \delta(1-z)\ln(z_{\max}) \right) + \left(\frac{\ln(1-w)}{1-w} \right)_+ \delta(1-z) \right\}. \tag{B.15}
\end{aligned}$$

The same result is obtained for $1/(u_3 s_{23})$ with replacing t_{30} by u_{30} .

- $I_1(u_3 s_{13})$

This type of integral cannot be found in previous calculations. Thus, we have to calculate it from scratch with similar methods used for $I_1(t_3 u_3)$ in Eq. (B.14). The result is

$$\begin{aligned}
g(z)^{-\varepsilon}(1-w)^{-\varepsilon}I_1(u_3 s_{13}) = & -\frac{\pi}{s^2 v^2 w \cos \psi} \frac{\Gamma(1-2\varepsilon)}{\Gamma^2(1-\varepsilon)} \left\{ \delta(1-w)\delta(1-z) \right. \\
& \times \left[\frac{1}{\varepsilon^2} + \frac{1}{\varepsilon} \ln \left(\frac{1-v}{v^2} \right) - \ln^2(v) + \frac{1}{2} \ln^2(1-v) \right] + \delta(1-z) \\
& \times \left[\frac{1}{(1-w)_+} \left(-\frac{1}{\varepsilon} + \ln \left(\frac{v^2 w}{(1-vw)(1-v-vw)} \right) \right) + \left(\frac{\ln(1-w)}{1-w} \right)_+ \right. \\
& - \ln \left(\frac{(1+\cos \psi)(2-v-vw)}{2(v+\cos \psi(vw-1)-1)} \right) \left. \right] + \delta(z_1-z) \left[\frac{1}{(1-w)_+} \left(-\frac{1}{\varepsilon} \right. \right. \\
& + \ln \left(\frac{v^2 w(1-v-vw)}{(1-vw)(1-v+vw)^2} \right) \left. \right) + \left(\frac{\ln(1-w)}{1-w} \right)_+ \\
& - \ln \left(\frac{(2-v-vw)(1-v+vw) \left(\frac{\cos \psi}{1-v+vw} + \frac{1}{2} - \frac{\cos \psi}{2} \right)}{1-v+\cos \psi - vw \cos \psi} \right) \left. \right] \\
& + v \left[\frac{\theta(1-z)}{[D_2(1-z)]_+} + \frac{\theta(z-1)}{[D_2(z-1)]_+} \right. \\
& \left. - \frac{1-v-vw}{1-v+vw} \left(\frac{\theta(z_1-z)}{[D_2(z_1-z)]_+} + \frac{\theta(z-z_1)}{[D_2(z-z_1)]_+} \right) \right] \left. \right\}, \tag{B.16}
\end{aligned}$$

with $D_2 = 2 - 2z - v + 2zv - vw$.

- $I_1(s_{13}s_{23})$

Similar to $I_1(t_3 s_{23})$, we find

$$\begin{aligned}
g(z)^{-\varepsilon}(1-w)^{-\varepsilon}I_1(s_{13}s_{23}) &= \frac{\pi}{2svs_{130}\cos\psi} \frac{\Gamma(1-2\varepsilon)}{\Gamma^2(1-\varepsilon)} \\
&\times \left\{ -\frac{1}{\varepsilon}\delta(1-w) \left[\frac{1}{(1-z)_+} - \varepsilon \frac{\ln z}{1-z} - \varepsilon \left(\frac{\ln(1-z)}{1-z} \right)_+ \right] \right. \\
&+ \frac{1}{(1-w)_+} \left[\frac{\theta(z_1-z)}{(z_1-z)_+} + \frac{\theta(z-z_1)}{(z-z_1)_+} \right] + \frac{1}{\varepsilon^2}\delta(1-w)\delta(1-z) \\
&\left. + \delta(z_1-z) \left[-\frac{1}{\varepsilon} \frac{1}{(1-w)_+} + \left(\frac{\ln(1-w)}{1-w} \right)_+ - \ln \left(1 - \frac{z_{\min}}{z_1} \right) \frac{1}{1-w} \right] \right\} .
\end{aligned} \tag{B.17}$$

C Soft Matrix Elements and Integrals

In this Appendix we give the (un)polarized matrix elements for the processes

$$\begin{aligned}\gamma(p_a) q(p_b) &\rightarrow q(p_c) g(p_d) g(p_e), \\ \gamma(p_a) g(p_b) &\rightarrow q(p_c) \bar{q}(p_d) g(p_e),\end{aligned}\tag{C.1}$$

in the soft limit, i.e., when a gluon in the final state has vanishing energy. We apply the eikonal double pole approximation as outlined in Sec. 5.1. If we associate gluon e with the soft particle, the matrix elements squared in $n = 4 - 2\varepsilon$ dimensions exhibit the following forms

$$\begin{aligned}\overline{\sum} |\mathcal{M}_{\gamma q \rightarrow qgg}|^2 \Big|_{\text{soft}} &= \overline{\sum} |\mathcal{M}_{\gamma q \rightarrow qg}|^2 \mathcal{S}_{\gamma q \rightarrow qg}, \\ \overline{\sum} |\mathcal{M}_{\gamma g \rightarrow q\bar{q}g}|^2 \Big|_{\text{soft}} &= \overline{\sum} |\mathcal{M}_{\gamma g \rightarrow q\bar{q}}|^2 \mathcal{S}_{\gamma g \rightarrow q\bar{q}}, \\ \overline{\sum} \Delta |\mathcal{M}_{\gamma q \rightarrow qgg}|^2 \Big|_{\text{soft}} &= \overline{\sum} \Delta |\mathcal{M}_{\gamma q \rightarrow qg}|^2 \mathcal{S}_{\gamma q \rightarrow qg}, \\ \overline{\sum} \Delta |\mathcal{M}_{\gamma g \rightarrow q\bar{q}g}|^2 \Big|_{\text{soft}} &= \overline{\sum} \Delta |\mathcal{M}_{\gamma g \rightarrow q\bar{q}}|^2 \mathcal{S}_{\gamma g \rightarrow q\bar{q}},\end{aligned}\tag{C.2}$$

with

$$\begin{aligned}\mathcal{S}_{\gamma q \rightarrow qg} &= 2g_s^2 \mu_d^{2\varepsilon} \left[C_A \left(\frac{s}{s_{13}s_{23}} + \frac{t}{u_3 s_{23}} \right) - \frac{1}{C_A} \left(\frac{u}{u_3 s_{13}} \right) \right], \\ \mathcal{S}_{\gamma g \rightarrow q\bar{q}} &= 2g_s^2 \mu_d^{2\varepsilon} \left[C_A \left(\frac{t}{u_3 s_{23}} + \frac{u}{u_3 s_{13}} \right) - \frac{1}{C_A} \left(\frac{s}{s_{13}s_{23}} \right) \right].\end{aligned}\tag{C.3}$$

The unpolarized and polarized n -dimensional LO matrix elements in Eq. (C.2) read

$$\overline{\sum} |\mathcal{M}_{\gamma q \rightarrow qg}|^2 = \mathcal{N} 2C_F \left[-\frac{s}{t} - \frac{t}{s} + \varepsilon \frac{u^2}{st} \right],$$

$$\begin{aligned}
\overline{\sum} |\mathcal{M}_{\gamma g \rightarrow q \bar{q}}|^2 &= \mathcal{N} \frac{1}{1-\varepsilon} \left[(1-\varepsilon) \left(\frac{t}{u} + \frac{u}{t} \right) - 2\varepsilon \right], \\
\overline{\sum} \Delta |\mathcal{M}_{\gamma q \rightarrow qg}|^2 &= \mathcal{N} 2C_F \left[\frac{t}{s} - \frac{s}{t} - \varepsilon \frac{u^2}{st} \right], \\
\overline{\sum} \Delta |\mathcal{M}_{\gamma g \rightarrow q \bar{q}}|^2 &= -\mathcal{N} \left[\frac{t}{u} + \frac{u}{t} \right].
\end{aligned} \tag{C.4}$$

Here, the prefactor is defined as $\mathcal{N} = (g_s g_e e_q)^2 \mu_d^{4\varepsilon}$. Next, the integration over the phase space of the soft gluon, dS in Eq. (5.9), has to be performed. This is done in the c.m.s. frame of the two incoming partons a and b using the following parameterization

$$\begin{aligned}
p_a &= \frac{\sqrt{s}}{2} (1, 0, 0, -1, \dots), \\
p_b &= \frac{\sqrt{s}}{2} (1, 0, 0, 1, \dots), \\
p_c &= \frac{\sqrt{s}}{2} (1, 0, 2\sqrt{v(1-v)}, 1-2v, \dots), \\
p_d &= \frac{\sqrt{s}}{2} (1, 0, -2\sqrt{v(1-v)}, -(1-2v), \dots),
\end{aligned} \tag{C.5}$$

and Eq. (5.6) for the momentum of the soft gluon e . With the help of [87] the integrals then take the form

$$\begin{aligned}
\int dS \frac{1}{s_{13}u_3} &= -\frac{1}{2sv} \frac{1}{\varepsilon^2} v^{-\varepsilon} (\delta_s)^{-2\varepsilon} \left[1 + \varepsilon^2 \text{Li}_2(1-v) \right], \\
\int dS \frac{1}{s_{13}s_{23}} &= \frac{1}{2s} \frac{1}{\varepsilon^2} (\delta_s)^{-2\varepsilon}, \\
\int dS \frac{1}{u_3 s_{23}} &= -\frac{1}{2s(1-v)} \frac{1}{\varepsilon^2} (1-v)^{-\varepsilon} (\delta_s)^{-2\varepsilon} \left[1 + \varepsilon^2 \text{Li}_2(v) \right],
\end{aligned} \tag{C.6}$$

where Li_2 is the di-logarithm function, see, e.g., [95].

Bibliography

- [1] E. Rutherford, *Philosophical Magazine* **21** (1911) 669.
- [2] N. Bohr, *The Nobel Foundation* (1922).
- [3] C. M. G. Lattes, H. Muirhead, G. P. S. Occhialini, and C. F. Powell, *Nature* **159** (1947) 694.
- [4] M. Gell-Mann, *Phys. Lett.* **8** (1964) 214.
- [5] G. Zweig, CERN-TH-412.
- [6] V. E. Barnes *et al.*, *Phys. Rev. Lett.* **12** (1964) 204.
- [7] E. D. Bloom *et al.*, *Phys. Rev. Lett.* **23** (1969) 930; *ibid.*, 935;
For review see, for example: J. I. Friedman and H. W. Kendall,
Ann. Rev. Nucl. Part. Sci. **22** (1972) 203;
see also: H. W. Kendall, Nobel lecture 1990,
<http://nobelprize.org/physics/laureates/1990/kendall-lecture.pdf>.
- [8] D. J. Gross and F. Wilczek, *Phys. Rev.* **D9** (1974) 980;
H. D. Politzer, *Phys. Rev. Lett.* **30** (1973) 1346.
- [9] for more information concerning HERA, see:
<http://www.desy.de/f/hera>.
- [10] M. J. Alguard *et al.*, *Phys. Rev. Lett.* **37** (1976) 1261.
- [11] European Muon Collaboration (EMC), J. Ashman *et al.*, *Phys. Lett.*
B206 (1988) 364; *ibid.*, *Nucl. Phys.* **B328** (1989) 1.
- [12] R. L. Jaffe and A. Manohar, *Nucl. Phys.* **B337** (1990) 509;
X.-D. Ji, *Phys. Rev. Lett.* **78** (1997) 610;
B. L. G. Bakker, E. Leader, and T. L. Trueman, *Phys. Rev.* **D70** (2004)
114001.
- [13] see, e.g., E. W. Hughes, and R. Voss, *Ann. Rev. Nucl. Part. Sci.* **49**
(1999) 303;

- K. Rith, in *Proceedings of the XIIth International Workshop on Deep-Inelastic Scattering*, D. Bruncko *et al.*, eds. Institute of Exp. Physics SAS (2004) p. 183;
S. D. Bass, *Rev. Mod. Phys.* **77** (2005) 1257.
- [14] I. Balitsky and X.-D. Ji, *Phys. Rev. Lett.* **79** (1997) 1225.
- [15] X.-D. Ji, *Phys. Rev.* **D55** (1997) 7114;
HERMES Collaboration, A. Airapetian *et al.*, [arXiv:0802.2499](#) [hep-ex].
- [16] N. Mathur, S. J. Dong, K. F. Liu, L. Mankiewicz, and N. C. Mukhopadhyay, *Phys. Rev.* **D62** (2000) 114504;
QCDSF Collaboration, M. Göckeler *et al.*, *Phys. Rev. Lett.* **92** (2004) 042002;
LHPC Collaboration, P. Hägler *et al.*, *Phys. Rev.* **D68** (2003) 034505;
ibid., [arXiv:0705.4295](#) [hep-lat];
QCDSF-UKQCD Collaboration, Q. M. Ohtani *et al.*, [arXiv:0710.1534](#) [hep-lat].
- [17] M. Glück, E. Reya, M. Stratmann, and W. Vogelsang, *Phys. Rev.* **D63** (2001) 094005.
- [18] COMPASS Collaboration, C. Bernet, [hep-ex/0405073](#).
- [19] COMPASS Collaboration, M. Alekseev *et al.*, [arXiv:0802.3023](#) [hep-ex].
- [20] COMPASS Collaboration, E. S. Ageev *et al.*, *Phys. Lett.* **B633** (2006) 25.
- [21] HERMES Collaboration, A. Airapetian *et al.*, *Phys. Rev. Lett.* **84** (2000) 2584;
P. Liebing, *AIP Conf. Proc.* **915** (2007) 331.
- [22] B. Jäger, M. Stratmann, and W. Vogelsang, *Eur. Phys. J.* **C44** (2005) 533.
- [23] C. Hendlmeier, M. Stratmann, and A. Schäfer, *Eur. Phys. J.* **C48** (2006) 135.
- [24] D. de Florian, R. Sassot, M. Stratmann, and W. Vogelsang, [arXiv:0804.0422](#) [hep-ph].
- [25] for more information concerning the EIC project, see official webpage:
<http://www.bnl.gov/eic>.

- [26] G. Bunce, N. Saito, J. Soffer, and W. Vogelsang, *Ann. Rev. Nucl. Part. Sci.* **50** (2000) 525.
- [27] PHENIX Collaboration, S. S. Adler *et al.*, *Phys. Rev. Lett.* **98** (2007) 012002.
- [28] STAR Collaboration, B. I. Abelev *et al.*, *Phys. Rev. Lett.* **97** (2006) 252001;
ibid., [arXiv:0710.2048 \[hep-ex\]](#).
- [29] PHENIX Collaboration, A. Adare *et al.*, *Phys. Rev.* **D76** (2007) 051106;
PHENIX Collaboration, S. S. Adler *et al.*, *Phys. Rev. Lett.* **93** (2004) 202002;
ibid., *Phys. Rev.* **D73** (2006) 091102;
PHENIX Collaboration, K. Boyle, *AIP Conf. Proc.* **842** (2006) 351.
- [30] S. B. Libby and G. Sterman, *Phys. Rev.* **D18** (1978) 3252;
R. K. Ellis, H. Georgi, M. Machacek, H. D. Politzer, and G. G. Ross, *Phys. Lett.* **B78** (1978) 281; *ibid.*, *Nucl. Phys.* **B152** (1979) 285;
D. Amati, R. Petronzio, and G. Veneziano, *Nucl. Phys.* **B140** (1978) 54;
ibid., *Nucl. Phys.* **B146** (1978) 29;
G. Curci, W. Furmanski, and R. Petronzio, *Nucl. Phys.* **B175** (1980) 27;
J. C. Collins, D. E. Soper, and G. Sterman, *Phys. Lett.* **B134** (1984) 263;
ibid., *Nucl. Phys.* **B261** (1985) 104;
J. C. Collins, *Nucl. Phys.* **B394** (1993) 169.
- [31] B. Jäger, *Studies of Hadronic Spin Structure in Hard Scattering Processes at the Next-to-Leading Order of QCD*. PhD thesis, Universität Regensburg (2004).
- [32] B. W. Harris and J. F. Owens, *Phys. Rev.* **D65** (2002) 094032.
- [33] C. Hendlmeier, M. Stratmann, and A. Schäfer, in *Proceedings of the XVth International Workshop on Deep-Inelastic Scattering*, [arXiv:0706.3766 \[hep-ph\]](#).
- [34] C. Hendlmeier, A. Schäfer, and M. Stratmann, [arXiv:0803.1940 \[hep-ph\]](#), accepted for publication in *Eur. Phys. J. C* (2008).
- [35] C. Hendlmeier, A. Schäfer, and M. Stratmann, work in progress.
- [36] T. Muta, *Foundations of Quantum Chromodynamics*. World Scientific (1987);

- CTEQ Collaboration, R. Brock *et al.*, *Rev. Mod. Phys.* **67** (1995) 157;
R. K. Ellis, W. J. Stirling, and B. R. Webber, *QCD and Collider Physics*.
Cambridge University Press (1996);
R. D. Field, *Applications of Perturbative QCD*. Addison-Wesley (1989);
P. Pascual and T. Tarrach, *Renormalization for the Practitioner*. Springer
(1984);
J. C. Collins, *Renormalization*. Cambridge University Press (1984).
- [37] J. D. Bjorken and S. D. Drell, *Relativistic Quantum Fields*. McGraw Hill
(1964).
- [38] L. D. Faddeev and V. N. Popov, *Phys. Lett.* **B25** (1967) 29.
- [39] Particle Data Group Collaboration, W.-M. Yao *et al.*, *J. Phys.* **G33**
(2006) 1.
- [40] S. Bethke, *Nucl. Phys. Proc. Suppl.* **135** (2004) 345.
- [41] M. Beneke, *Phys. Rept.* **317** (1999) 1;
C. F. Berger, *Soft Gluon Exponentiation and Resummation*.
PhD thesis, State University of New York at Stony Brook (2003).
- [42] C. G. Bollini and J. J. Giambiagi, *Phys. Lett.* **B40** (1972) 566.
- [43] G. 't Hooft and M. J. G. Veltman, *Nucl. Phys.* **B44** (1972) 189.
- [44] T. Kinoshita, *J. Math. Phys.* **3** (1962) 650.
- [45] T. D. Lee and M. Nauenberg, *Phys. Rev.* **133** (1964) B1549.
- [46] F. Bloch and A. Nordsieck, *Phys. Rev.* **52** (1937) 54.
- [47] P. Breitenlohner and D. Maison, *Commun. Math. Phys.* **52** (1977) 11.
- [48] J. C. Taylor, *Nucl. Phys.* **B33** (1971) 436.
- [49] A. A. Slavnov, *Theor. Math. Phys.* **10** (1972) 99.
- [50] W. A. Bardeen, A. J. Buras, D. W. Duke, and T. Muta, *Phys. Rev.* **D18**
(1978) 3998.
- [51] G. 't Hooft, *Nucl. Phys.* **B61** (1973) 455.
- [52] M. Glück, E. Reya, and A. Vogt, *Phys. Rev.* **D45** (1992) 3986.
- [53] J. C. Collins and D. E. Soper, *Nucl. Phys.* **B194** (1982) 445.

- [54] G. Altarelli and G. Parisi, *Nucl. Phys.* **B126** (1977) 298;
L. N. Lipatov, *Sov. J. Nucl. Phys.* **20** (1975) 94;
V. N. Gribov and L. N. Lipatov, *Sov. J. Nucl. Phys.* **15** (1972) 438;
Y. L. Dokshitzer, *Sov. Phys. JETP* **46** (1977) 641.
- [55] C. F. Berger, *Phys. Rev.* **D66** (2002) 116002;
S. Moch, J. A. M. Vermaseren, and A. Vogt, *Nucl. Phys.* **B646** (2002) 181;
ibid., *Nucl. Phys.* **B688** (2004) 101; *ibid.*, *Nucl. Phys.* **B691** (2004) 129.
- [56] J. Pumplin *et al.*, *JHEP* **0207** (2002) 012.
- [57] D. Stump *et al.*, *JHEP* **10** (2003) 046;
W. K. Tung *et al.*, *JHEP* **02** (2007) 053;
P. M. Nadolsky *et al.* [arXiv:0802.0007](#) [hep-ph].
- [58] A. D. Martin, R. G. Roberts, W. J. Stirling, and R. S. Thorne, *Eur. Phys. J.* **C23** (2002) 73; *ibid.*, *Eur. Phys. J.* **C28** (2003) 455; *ibid.*, *Eur. Phys. J.* **C35** (2004) 325; *ibid.*, *Phys. Lett.* **B604** (2004) 61;
A. D. Martin, W. J. Stirling, R. S. Thorne, and G. Watt *Phys. Lett.* **B652** (2007) 292.
- [59] CTEQ Collaboration, H. L. Lai *et al.*, *Eur. Phys. J.* **C12** (2000) 375.
- [60] J. Huston *et al.*, *Phys. Rev.* **D58** (1998) 114034.
- [61] A. D. Martin, R. G. Roberts, W. J. Stirling, and R. S. Thorne, *Eur. Phys. J.* **C14** (2000) 133.
- [62] D. de Florian, G. A. Navarro, and R. Sassot, *Phys. Rev.* **D71** (2005) 094018.
- [63] W. Vogelsang, *Phys. Rev.* **D54** (1996) 2023.
- [64] R. Mertig and W. L. van Neerven, *Z. Phys.* **C70** (1996) 637.
- [65] J. Blümlein and H. Böttcher, *Nucl. Phys.* **B636** (2002) 225.
- [66] Asymmetry Analysis Collaboration, Y. Goto *et al.*, *Phys. Rev.* **D62** (2000) 034017.
- [67] M. Klasen, *Rev. Mod. Phys.* **74** (2002) 1221.
- [68] D. de Florian and S. Frixione, *Phys. Lett.* **B457** (1999) 236.
- [69] M. Glück, E. Reya, and A. Vogt, *Phys. Rev.* **D46** (1992) 1973.

- [70] M. Glück and E. Reya, *Phys. Rev.* **D28** (1983) 2749;
M. Fontannaz and E. Pilon, *Phys. Rev.* **D45** (1992) 382.
- [71] M. Stratmann and W. Vogelsang, *Phys. Lett.* **B386** (1996) 370.
- [72] S. Kretzer, *Phys. Rev.* **D62** (2000) 054001.
- [73] D. de Florian, R. Sassot, and M. Stratmann, *Phys. Rev.* **D76** (2007) 074033.
- [74] A. H. Müller, *Phys. Rev.* **D18** (1978) 3705.
- [75] B. A. Kniehl, G. Kramer, and B. Potter, *Nucl. Phys.* **B582** (2000) 514.
- [76] S. Albino, B. A. Kniehl, and G. Kramer, *Nucl. Phys.* **B725** (2005) 181.
- [77] S. Albino, B. A. Kniehl, and G. Kramer, *Nucl. Phys.* **B734** (2006) 50.
- [78] M. Jamin and M. E. Lautenbacher, *Comput. Phys. Commun.* **74** (1993) 265.
- [79] S. Wolfram, *Mathematica*. see also: www.wri.com.
- [80] P. Aurenche, A. Douiri, R. Baier, M. Fontannaz, and D. Schiff, *Z. Phys.* **C24** (1984) 309.
- [81] M. Fontannaz, B. Pire, and D. Schiff, *Z. Phys.* **C8** (1981) 349.
- [82] J. J. Peralta, A. P. Contogouris, B. Kamal, and F. Lebessis, *Phys. Rev.* **D49** (1994) 3148.
- [83] G. Grispos, A. P. Contogouris, and G. Veropoulos, *Phys. Rev.* **D62** (2000) 014023.
- [84] C. Hendlmeier, *Two Hadron Production in Longitudinally Polarized Lepton-Nucleon Collisions*. Diplomarbeit, Universität Regensburg (2005);
C. Hendlmeier, M. Stratmann, and A. Schäfer, in *Proceedings of the Workshop on Symmetries and Spin (PRAHA SPIN 2005)*,
Czech. J. Phys. **56 C** (2006) 151.
- [85] M. A. Nowak, M. Praszalowicz, and W. Slominski, *Ann. Phys.* **166** (1986) 443.
- [86] G. Passarino and M. J. G. Veltman, *Nucl. Phys.* **B160** (1979) 151.
- [87] W. Beenakker, H. Kuijf, W. L. van Neerven, and J. Smith, *Phys. Rev.* **D40** (1989) 54.

- [88] W. J. P. Beenakker, *Electroweak Corrections: Techniques and Applications*. PhD thesis, University of Leiden (1989).
- [89] I. Bojak, *NLO QCD Corrections to the Polarized Photo- and Hadroproduction of Heavy Quarks*. PhD thesis, Universität Dortmund (2000).
- [90] P. Aurenche, A. Douiri, R. Baier, M. Fontannaz, and D. Schiff, *Z. Phys.* **C29** (1985) 459.
- [91] M. Abramowitz and I. A. Stegun, *Handbook of Mathematical Functions with Formulas, Graphs, and Mathematical Tables*. Dover, New York (1964).
- [92] R. K. Ellis, M. A. Furman, H. E. Haber, and I. Hinchliffe, *Nucl. Phys.* **B173** (1980) 397.
- [93] B. Jäger, A. Schäfer, M. Stratmann, and W. Vogelsang, *Phys. Rev.* **D67** (2003) 054005.
- [94] B. Jäger, M. Stratmann, and W. Vogelsang *Phys. Rev.* **D70** (2004) 034010.
- [95] I. S. Gradstein and I. M. Ryshik, *Tables, Volume 1 and 2*. Verlag Harri Deutsch (1981).
- [96] E. L. Berger and L. E. Gordon, *Phys. Rev.* **D54** (1996) 2279.
- [97] C. Coriano and L. E. Gordon, *Nucl. Phys.* **B469** (1996) 202.
- [98] L. E. Gordon and W. Vogelsang, *Phys. Rev.* **D48** (1993) 3136.
- [99] L. E. Gordon and W. Vogelsang, *Phys. Rev.* **D49** (1994) 170.
- [100] W. Vogelsang, *Nucl. Phys.* **B475** (1996) 47.
- [101] Y. Matiounine, J. Smith, and W. L. van Neerven, *Phys. Rev.* **D58** (1998) 076002.
- [102] COMPASS Collaboration, G. Baum *et al.*, CERN-SPSLC-96-14.
- [103] L. J. Bergmann. PhD thesis, Florida State University (2003).
- [104] H. Baer, J. Ohnemus, and J. F. Owens, *Phys. Rev.* **D40** (1989) 2844.
- [105] H. Baer, J. Ohnemus, and J. F. Owens, *Phys. Lett.* **B234** (1990) 127.
- [106] J. F. Owens, *Phys. Rev.* **D65** (2002) 034011.

Danksagung

An dieser Stelle möchte ich allen Personen danken, die zur Entstehung dieser Arbeit in verschiedenster Weise beigetragen haben:

- Prof. Dr. Andreas Schäfer dafür, dass er mir es ermöglichte, dieses Thema zu bearbeiten. In unseren wöchentlichen Treffen hatte ich immer die Gelegenheit zum regen Gedankenaustausch. Sowohl bei konzeptionellen Fragestellungen als auch bei technischen Details der Rechnungen gab er mir sehr nützliche Ratschläge. Zusätzlich danke ich für die Finanzierung meines Forschungsaufenthaltes in Japan.
- Dr. Marco Stratmann dafür, dass er mir mit großem und unermüdlichem Einsatz das weite Feld der *perturbativen QCD* näher brachte. Trotz der großen Entfernung war er an allen Schritten, die zur Entstehung dieser Arbeit wichtig waren, in besonderem Maße beteiligt. Ich danke ihm weiter für jegliche Hilfe, die er mir während meiner Zeit in Japan zukommen ließ.
- Dr. Horst Fischer, Sonja Hedicke, Dr. Fritz-Herbert Heinsius, Dr. Jean-Marc Le Goff, Dr. Gerhard Mallot, Sebastien Procureur (COMPASS Kollaboration) und Dr. Elke-Caroline Aschenauer (HERMES Kollaboration) für viele fruchtbare Diskussionen im Zusammenhang mit den jeweiligen Experimenten und die Gelegenheit, an diversen Kollaborationstreffen und Workshops teilzunehmen.
- Meiner Frau Daniela, die mir in allen Lebenslagen zur Seite steht und mir auch in schwierigen Zeiten viel Kraft und Liebe gibt, und mit der ich sehnsüchtig auf die Geburt unseres ersten Kindes warte. Meinen Eltern dafür, dass sie mich in allen Belangen unterstützen, wenn es nötig ist.
- Meinem “perturbativen Mitstreiter” Johann Riedl und meinem Bürokollegen Nils Meyer für fachliche Diskussionen, aber auch Gespräche, die weit über Physik hinausgingen. Monika Maschek für ihre große Hilfe in allen organisatorischen Dingen.
- Nicht zuletzt meinen Freunden Klaus Allinger, Fabian Glaab, Markus Helchinger, Tobias Kaiser, Christoph Kamseder, Markus Maier und Christoph Tichy für die “Ablenkung” von Physik, wann immer ich das brauchte.

Während meiner Promotionszeit wurde ich von der “*Universität Bayern e. V.*” mittels eines Stipendiums im Rahmen des “*Bayerischen Eliteförderungsgesetzes*” finanziell unterstützt. Weiter erhielt ich Unterstützung durch das “*Bundesministerium für Bildung und Forschung*” (BMBF) und die “*Deutsche Forschungsgemeinschaft*” (DFG).